

Bimodal Gate Oxide Breakdown

for Sub-100nm CMOS Technology

by

Leila Rezaee

A thesis

presented to the University of Waterloo

in fulfillment of the

thesis requirement for the degree of

Doctor of Philosophy

in

Electrical and Computer Engineering

Waterloo, Ontario, Canada, 2008

©Leila Rezaee 2008

I hereby declare that I am the sole author of this thesis. This is a true copy of the thesis, including any required final revisions, as accepted by my examiners.

I understand that my thesis may be made electronically available to the public.

Abstract

In the last three decades, the electronic industry has registered a tremendous progress. The continuous and aggressive downsizing of the transistor feature sizes (CMOS scaling) has been the main driver of the astonishing growth and advancement of microelectronic industry. Currently, the CMOS scaling is almost reaching its limits. The gate oxide is now only a few atomic layers thick, and this extremely thin oxide causes a huge leakage current through the oxide. Therefore, a further reduction of the gate oxide thickness is extremely difficult and new materials with a higher dielectric constant are being explored. However, the phenomena of oxide breakdown and reliability are still serious issues in these thin oxides. Oxide breakdown exhibits a soft breakdown behavior at low voltages, and this is posing as one of the most crucial reliability issues for scaling of the ultra-thin oxides. In addition, the stress-induced leakage current (SILC) due to oxide has emerged as a scaling problem for the non-volatile memory technologies.

In this dissertation, a percolation modeling approach is introduced to study and understand the dramatic changes in the conductivity of a disordered medium. Two different simulation methods of percolative conduction, the site and bond percolation, are studied here. These are used in simulating the post-breakdown conduction inside the oxide. Adopting a Monte-Carlo method, oxide breakdown is modeled using a 2-D percolation theory. The breakdown statistics and post-breakdown characteristics of the oxide are computed using this model. In this work, the effects of different physical parameters, such as dimension and the applied stress are studied. The simulation results show that a thinning of oxide layer and increasing the oxide area result in softening of breakdown. It is observed that the breakdown statistics appear to follow Weibull characteristics. As revealed

by simulations, the Weibull slope changes linearly with oxide thickness, while not having a significant change when the area is varied and when the amount of the applied stress is varied. It is shown that the simulation results are well correlated with the experimental data reported in the literature.

In this thesis, studying the conduction through the oxide using percolation model, it was discovered that a critical or a quasi-critical phenomenon occurs depending on the oxide dimensions. The criticality of the phase-transition results in a hard breakdown while the soft breakdown occurs due to a quasi-critical nature of percolation for ultra-thin oxides.

In the latter part of the thesis, a quantum percolation model is studied in order to explain and model the stress induced leakage current. It is explained that due to the wave nature of electrons, the SILC can be modeled as a tunneling path through the stressed oxide with the smaller tunneling threshold compared to the virgin oxide.

In addition to the percolation model, a Markov chain theory is introduced to simulate the movement of electron as a random walk inside the oxide, and the breakdown is simulated using this random-walk of electron through the accumulated traps inside the oxide. It is shown that the trapping-detrapping of electrons results in an electrical noise in the post-breakdown current having $1/f$ noise characteristics. Using simulation of a resistor network with Markov theory, the conductance of the oxide is computed.

An analytical study of a 2-D site percolation system is conducted using recursive methods and useful closed-form expressions are derived for specialized networks.

Acknowledgments

It is my great pleasure to thank Prof. C. R. Selvakumar for his guidance and encouragements throughout my Ph.D. studies. I would like to acknowledge the committee members, Prof. Tong Leung, Prof. Manoj Sachdev, and Prof. Andrei Sazanov who accepted to review my thesis. Moreover, I would like to thank Prof. Durga Misra who granted me the honor to have him as the external examiner in my defense exam. I thank all the professors for their valuable comments.

I would like to thank the University of Waterloo for facilitating the research environment and the NSERC for funding this research. This research is facilitated in part by a Marsland Fellowship to Professor Selvakumar.

I am forever indebted to my parents. I have no suitable words that can describe their everlasting love and support to me throughout my life.

I would like to express my utmost gratitude to my dear husband, my love, and my best friend, Javad. This work was not possible without his help, encouragements, and support during the tough stages of my research. This thesis is much of a product of his support and kindness.

I am grateful to my brothers and sister, my friends and all those who helped me throughout the steps of my life.

Last but not least, thanks be to God for every thing he granted me in my life.

Contents

List of Tables	xii
List of Figures	xx
1 Introduction	1
1.1 Motivations for this Thesis	5
1.2 Thesis Organization	7
2 Gate Oxide Breakdown	9
2.1 Physical Models of Oxide Breakdown	10
2.1.1 Anode Hydrogen-Release Model (AHR)	11
2.1.2 Anode Hole Injection Model	13
2.1.3 Thermochemical Model	15
2.2 Oxide Reliability Characterization	17
2.3 Breakdown Statistics and Reliability Projection	18
2.3.1 Choice of Probability Function for Reliability Projection	18
2.3.2 Area Scaling	20
2.3.3 Voltage or Field Extrapolation	20

2.3.4	Temperature Scaling	21
2.4	Soft and Hard Breakdown	22
2.4.1	Different Types of Soft and Hard Breakdown	23
2.4.2	Differences and Similarities of Soft and Hard Breakdown	24
2.4.3	Physical Models for Soft Breakdown	26
2.5	Summary and Conclusion	28
3	Percolation and Phase Transition	30
3.1	Introduction	30
3.2	Percolation	31
3.2.1	History	31
3.2.2	What is Percolation?	32
3.2.3	Mathematical Definition	33
3.2.4	Site and Bond Percolation	34
3.3	Phase Transition and Critical Phenomena	36
3.4	Percolation and Electrical Conduction	38
3.5	Modeling of Percolation Path with a Parallel-Series Network of Resistors	39
3.6	Modeling of Percolation Path conductance with a Network of Resistors	42
3.7	Summary and Conclusion	44
4	Percolation Modeling of Oxide Breakdown	46
4.1	Introduction	46
4.2	Modeling of Oxide as a Network of Molecular Cells	47
4.3	Breakdown Modeling	50
4.4	Oxide Reliability Test	51

4.5	Simulation of the Post-Breakdown Conduction in the Oxide	53
4.6	Summary and Conclusion	54
5	Dimension and Stress Effects on Breakdown	56
5.1	Study of Thickness Effect on Oxide Breakdown	57
5.1.1	Effects of Thickness on Time-to-Breakdown and Weibull Shape Factor	58
5.1.2	Thickness Effect on Post-Breakdown Conduction	60
5.1.3	Explaining the Results as the Quasi-Critical Nature of Soft Break- down	63
5.1.4	Breakdown Statistics	68
5.2	Study of Width (Area) Effect on Breakdown Characteristics	72
5.2.1	Width Effect on Time-to-Breakdown and Weibull Shape Factor . .	72
5.2.2	Width Effect on Post-Breakdown Conduction	75
5.2.3	Width Effect on Percolation Probability Curves	75
5.3	Study of Stress Effect on Breakdown Behavior	77
5.3.1	Stress Effect on Time-to-Breakdown and Weibull Shape factor . . .	79
5.3.2	Stress Effect on Post-Breakdown Conduction	83
5.4	Power-Law or Exponential Voltage-Dependence	83
5.4.1	Accumulation of Defects	84
5.5	Summary and Conclusion	88
6	Markov Chain Modeling of Breakdown	91
6.1	The Markov Chain Fundamentals	92
6.1.1	Hitting Times and Absorption Probabilities	95
6.1.2	Harmonic function	96

6.2	Electron Transport Inside the Oxide	98
6.2.1	Non-Trapped Network	98
6.2.2	Trapped Network	101
6.3	Trap-Detrap	104
6.4	Markov Model of Trapped Configuration as a Resistor Network	109
6.4.1	Resistor Network Equivalent Markov Chain	109
6.4.2	Voltage Interpretation	110
6.4.3	Current Interpretation	111
6.4.4	Simulation Results	113
6.5	Summary and Conclusion	114
7	Tunneling Model of SILC	115
7.1	SILC Physical Models	116
7.2	Quantum Percolation with Tunneling	118
7.3	Modeling of SILC as Parallel Tunneling through Broken Path and the Whole Oxide	122
7.3.1	Fowler-Nordheim Tunneling	122
7.4	Simulation of Tunneling with MATLAB	123
7.5	Summary and Conclusion	134
8	Summary and Conclusion	139
8.1	Summary	139
8.2	Future Works	142
	Appendices	145

A	Analytical Formulae for Percolation Probability in a 2-D System	146
A.1	Percolation Probability for General $M \times N$ Networks	147
A.2	Percolation Probability for $3 \times N$ and $4 \times N$ Networks	153
A.3	Percolation Probability for an $M \times 2$ Network	157
B	Estimation of the Cell Size in the 2-D Percolation Model	166
C	MATLAB Simulation Codes	168
C.1	2-D Network Simulation	168
C.2	Resistor Network Conductance	169
C.3	Parallel-Series Network Model	171
C.4	TDDB Simulation	173
C.5	Markov Simulation	174
C.6	Analytical Formula Extraction	178
	Bibliography	181
	Glossary	210
	Index	213

List of Tables

5.1	The statistical results for samples with width = 200 cells and thickness = 5, 10, 20, and 40 cells	58
7.1	The tunneling energy barriers resulted from the simulation of I-V curves in Figure 7.4a with F-N tunneling current; The energy barriers are calculated for the virgin device current and after applying the ramp gate voltage stress.	126
7.2	The tunneling energy barriers before and after applying positive and negative voltage stress; The results show the independence of the SILC on the polarity of the stress.	128
7.3	The tunneling energy barriers that are calculated using the experimental results in Figure 7.6a, showing the dependence of after-stress current on repeating the stress.	130
7.4	The tunneling energy barriers that are calculated using the experimental results in Figure 7.7a, showing the dependence of after-stress current on the stop voltage of the ramp stress.	132

7.5	The tunneling energy barriers that are calculated using the experimental results in Figure 7.8, showing the dependence of after-stress current on temperature.	135
7.6	The tunneling energy barriers that are calculated using the experimental results in Figure 7.8, showing the dependence of after-stress current on temperature.	135
7.7	The change of tunneling energy barrier of the damaged current path with oxide thickness; The results are based on the experimental data presented on Figure 7.9a. The data is collected based on the current inside virgin and stressed oxide samples with thickness = 5.1 nm, 6.0 nm, 7.5 nm, and 9.7 nm.	137
A.1	The eight possible rightmost column patterns for a $3 \times N$ network and their corresponding terms in calculation of the auxiliary functions	164
A.2	The sixteen possible rightmost column patterns for a $4 \times N$ network and their corresponding terms in calculation of the auxiliary functions	165

List of Figures

1.1	(a) The trend in MOS channel length scaling and the prediction made in the 2007 International Technology Roadmap for Semiconductor (ITRS 2007)	3
2.1	The process of defect generation by the Hydrogen Release Model	11
2.2	Schematic illustration of the anode hole injection model	13
2.3	Life-time extrapolation based on E and $1/E$ models	15
2.4	$\log(T_{BD})$ as a function of electric field (E) and reciprocal of electric field ($1/E$) based on the measurement data collected at low electric field and accelerated temperatures. $\log(T_{BD})$ changes linearly with electric field, a good fit to E -model.	16
2.5	Fitting the experimental data to Log-normal and Weibull distributions	19
2.6	T_{BD} and Q_{BD} versus t_{ox} at 140°C and $6.2 \times 10.4 \text{ cm}^2$	26
3.1	One-dimensional Polya-walk; In diffusion the walk is directed by random scattering and in percolation the walk is controlled by the random medium.	33
3.2	Site and Bond Percolation	35
3.3	The behavior of $\theta(p)$ around the critical point (for bond-percolation)	37
3.4	The vertical and horizontal sites are modeled as series and parallel resistors.	40

3.5	The proposed model to calculate the conductance of the percolation path. In this model the percolation path is considered as a bunch of parallel resistors placed in series to form a current path between the two electrodes.	40
3.6	Conductance versus the defect density calculated using the parallel-series resistor network. Conductance changes as a power-law function of defect density ($\sigma \sim (p - p_{crit})^\alpha$ where $\alpha \simeq 1.5 - 1.6$).	41
3.7	The percolation network is considered as a resistor network, with the two top and bottom rows directly connected to the electrodes.	43
3.8	A randomly trapped network and its equivalent resistor network; R_1 and R_2 are the resistances of open and closed bonds, respectively.	43
4.1	(a) SiO ₂ cubic lattice, (b) Defects are created uniformly inside the oxide; the defect density is less than the critical value. (c) A percolation path is created through the defects inside the oxide.	49
4.2	Histogram of the failure statistics for a set of 50 samples with the size of 40×40 cells	52
4.3	Cumulative failure density diagram for a set of 50 samples with the size of 40 × 40 cells	52
4.4	The obtained Weibit versus $\ln(T_{BD})$ for a set of 50 samples with the size of 40 × 40 cells. The linear curve substantiates the Weibull distribution of the failure.	53
4.5	Post-breakdown current for a sample with the size of 40 × 40 cells	54

5.1	Comparison of the CFD diagrams for the samples with 40, 20, 10 and 5 cells thickness. The simulation is done over a set of samples with width = 200 cells, using the applied stress probability = 0.001.	59
5.2	Weibull function for samples with 40, 20, 10 and 5 cells thickness. The simulation is done over a set of samples with width = 200 cells, using the applied stress probability = 0.001.	59
5.3	The post-breakdown current for a sample with 40 cells thickness	60
5.4	The post-breakdown current for a sample with 20 cells thickness	61
5.5	The post-breakdown current for a sample with 10 cells thickness	61
5.6	The post-breakdown current for a sample with 5 cells thickness	62
5.7	The experimental post-breakdown current for 3nm SiO ₂ gate oxide	63
5.8	Percolation probability versus defect generation probability for samples with thickness changing from 2 cells to 40 cells. The width of all samples is 200 cells.	64
5.9	For thick oxides, the breakdown process can be explained in three stages: (1) a buildup stage, (2) a rapid runaway stage and (3) a post-breakdown stage.	65
5.10	Quasi-critical characteristics of percolation for an oxide with a few layers of cells thickness	66
5.11	(a) Weibull slope versus thickness changing from 2 to 20 cells. The width of all samples is 200 cells. The simulation results show that the Weibull slope is a linear function of the thickness. (b) Measured Weibull slopes versus oxide thickness for p-channel FET (PFET) and n-channel FET (NFET)	69

5.12	Weibull slope versus thickness in a log-log scale; For very thick oxides, the Weibull slope fits a power-law function better than a linear function of the oxide thickness	70
5.13	Time-to-breakdown versus oxide thickness; (a) Simulation results; T_{63} is plotted versus thickness ranging from 2 to 40 cells. The width of all samples is 200 cells. (b) Experimental results	71
5.14	Weibull function versus time-to-breakdown for samples with width ranging from 5 to 200 cells; The results show that the Weibull shape factor (β) does not vary with width. The thickness of all the samples is equal to 5 cells. . .	73
5.15	Area dependence of the normalized T_{BD} for several values of t_{ox} ; (a) Simulation results; (b) Measurement results	74
5.16	Post-breakdown current for a sample with width = 200 cells, and thickness = 10 cells; The $p_s = 0.001$ has been used to compute the post-breakdown conductance.	76
5.17	Post-breakdown current for a sample with width = 20 cells, and thickness = 10 cells; The $p_s = 0.001$ has been used to compute the post-breakdown conductance.	76
5.18	Percolation probability versus defect density for samples with different widths, ranging from 5 to 5000 cells; (a) All samples are 20 cells thick. (b) All samples are 5 cells thick.	78
5.19	Weibull function versus time for different stress conditions for a set of samples with thickness = 5 and width = 200 cells; The Weibull slope does not change with the stress, matching the experiments. (a) Simulation results; (b) Experimental data reported in the literature	80

5.20	(a) The Weibull shape factor versus the applied stress for samples with thickness = 2, 3, 4, 5 and 10 cells, and width = 200 cells; The Weibull slope does not change with the applied stress, matching the experimental results.	
	(b) Experimental data reported in the literature	81
5.21	(a) Lifetime versus applied stress in a log-log scale for samples with thickness = 2, 3, 4, 5, 10, 40 cells; All samples have the same width = 200 cells. It is evident that the lifetime has a power-law relationship with the applied stress. (b) Log-log plot of lifetime versus gate voltage stress for samples with thickness varying from 2.3 to 5 nm; All the samples have the area = 6.2×10^{-4} cm ²	82
5.22	The density of accumulated defects inside the oxide versus time for different applied stress	86
5.23	Time-to-breakdown versus the applied stress in a log-log scale, assuming the critical defect density = 0.3; The curve is plotted based on Equation 5.5.	87
5.24	Time-to-breakdown versus the applied stress in a log-log scale, assuming the normalized critical defect density = 0.1, 0.3, 0.5; The curve is plotted based on Equation 5.5.	87
5.25	Time-to-breakdown versus the applied stress in a semi-log scale, assuming the critical defect density = 0.2, 0.3, 0.4, 0.5; The curve is plotted based on Equation 5.5.	89
6.1	The state diagram corresponding to the transition matrix \mathbf{P}	94
6.2	Simple random walk on \mathbb{Z}	94
6.3	Markov chain model for the oxide	99

6.4	A sample 5×7 trapped network	101
6.5	The Markov chain corresponding to the trapped network of Figure 6.4	102
6.6	Absorption probability versus time for a 5×40 accumulatively trapped network	104
6.7	Absorption probability versus time for a 5×40 accumulatively trapped-detrapped network	105
6.8	The PSD of noise using Periodogram method	106
6.9	The PSD of noise using Burg method	107
6.10	The PSD of experimental current noise	108
6.11	Conductance for a resistor network with thickness = 5 cells, and width = 7 cells	113
7.1	The current density versus the oxide electric field (E_{ox}) before (the solid line) and after (the dashed line) applying the stress; The stress induced leakage current is defined as the difference between the current going through the virgin oxide (J_0) and the after-stress current (J): $J_{SILC} = J - J_0$	117
7.2	The conduction models for SILC; (a) The field enhancement due to trapped positive charges; (b) Trap-assisted elastic tunneling model of SILC; (c) Conduction due to local thinning of the gate oxide; (d) Inelastic trap-assisted tunneling	119
7.3	Typical wave functions of (a) extended state with mean free path l ; (b) localized state with localization length ξ	120

7.4	(a) The curves illustrate the experimental I-V characteristics of two similar 5.1-nm oxide n+ poly gate capacitors (area of 10^{-4} cm ²) after a ramp voltage stress up to an oxide field of = 12 MV/cm. (b) The simulation of the experimental I-V characteristics with two parallel F-N tunneling currents	125
7.5	The after-stress I-V characteristics are measured with positive gate voltage after positive and negative voltage stress. The curves illustrate the independence of the stress induced leakage current on the stress polarities.	127
7.6	Leakage current increase induced by repeated voltage ramps; (a) Sequence of curves (from a, virgin device, to j) with the same maximum voltage (5.5 V)	129
7.7	The leakage current increase depends on the maximum applied voltage. The voltage ramp is repeated on the same capacitor with increasing stop values: 5 V (curve a, virgin sample), 5.2 V (curve b), 5.4 V (curve c), 5.5 V (curve d), 5.6 V (curve e), 5.7 V (curve f), 5.8 V (curve g), and 5.9 V (curve h). The leakage current begins to increase after the ramp with 5.2-V peak voltage and the capacitor broke destructively at 5.9 V during (curve i) ramp.	131
7.8	Before-stress (solid lines) and after-stress (dashed-dotted lines) characteristics at different temperatures (77 K (curve a), 23°C (curve b), 100°C (curve c), and 250°C (curve d)); Curves b, c, and d were obtained from the same device, curve a from a similar device presenting the same virgin I-V characteristic at room temperature.	133
7.9	Dependence of the leakage current on the oxide thickness; The I-V curves are from virgin and stressed samples. The oxide thickness is: 5.1 nm (curve a), 6.0 nm (curve b), 7.5 nm (curve c), and 9.7 nm (curve d).	136

A.1	Percolation probability for $N = 6$ and $1 \leq M \leq 10$ obtained using Theorem A.1	154
A.2	An example for the auxiliary function $Q_{4,12}^{(010)}(p)$	155
A.3	Percolation probability for $M = 3$ and $N = 1, 5, 10, 20, 50, 100, 200, 500$ obtained by Theorem A.3	158
A.4	Percolation probability for $M = 4$ and $N = 1, 5, 10, 20, 50, 100, 200, 500$ obtained by Theorem A.4	159
A.5	Elementary patterns	162
A.6	An example: 12×2 trapped network	163

Chapter 1

Introduction

The concept of Field Effect Transistor (FET) was first patented in 1930 [1]. Thirty years later, in 1960, the FET was put into practice using Si-SiO₂ structure by Kahng and Atala [2]. The new structure was named Metal-Oxide-Semiconductor field effect transistor (MOSFET), and since then, has been incorporated in Integrated Circuits (IC's) [3]. Integrated circuits have been the core technology of micro-electronic industry for the past four decades. During the last three decades, the electronic industry has experienced a tremendous progress. Currently, microprocessors with more than one billion transistors are in production, and high capability of computation and high memory capacities have been achieved [4,5]. Microprocessor clock frequencies have been increasing at an average rate of about 1.25 times per year, from about 2 MHz (Intel 8080), made in 1974, to over 2 GHz today. The number of utilized transistors in IC's have been increasing at about 1.4 times per year, which facilitates more complexity of the circuits today [6,7].

The persistent downsizing of transistors is known to be the main component of the astounding advancement of microelectronic industry [8]. What has enabled such an ex-

ceptional growth is that decreasing the feature size of the unit transistor improves overall circuit performance while reducing the cost of the manufactured component [8–10]. The reduction of the carrier transport distance from the source to drain, and the diminution in capacitances associated with the devices as well as the interconnections will result in higher operation speed of smaller-size devices [5]. Smaller devices can be implemented in a smaller area with fewer materials and will consume less amount of power and decrease the costs of integrated circuits [5]. Moreover, more components per chip are feasible with smaller devices which facilitates more powerful circuit design and further enhancement of the system response.

By about 1965, Gordon Moore reported his important observation that for silicon-based integrated circuits, the number of transistors per square centimeter doubled every 12 months¹, and he made the prediction that this tendency must continue [11,12]. Actually, the doubling took hold in the industry and later was named as the “Moore’s Law”, which has controlled the micro and nano-electronic industry for the last four decades [13]. Having to follow the Moore’s law forced the leading-edge companies to direct the industry and recently manufacture devices with feature sizes below 100 nm [14]. However, for years, there has been a question that for how long the semiconductor industry can keep up its innovation and the Moore’s law can continue.

During the last four decades, many possible limits for the downsizing have been proposed, at different time periods [16]. In the late 1970’s, micrometer was thought to be the possible limit because of the expected difficulty in suppression of the short-channel effects and also because of the expected difficulty in optical lithography [16]. In early

¹In practice, in the past few decades, the density of transistors had been doubled in about every 18 months.

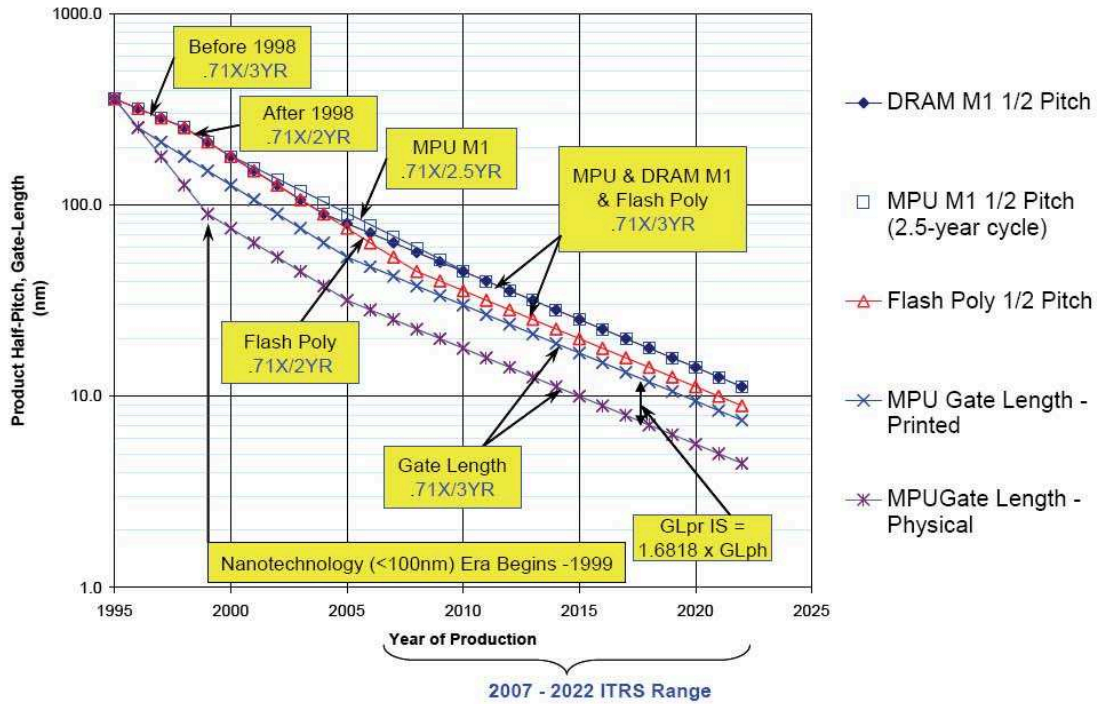


Figure 1.1: (a) The trend in MOS channel length scaling and the prediction made in the 2007 International Technology Roadmap for Semiconductor (ITRS 2007) [15]

1980's, half micron or quarter micron was considered as the limit because of the increased source/drain resistance, direct-tunneling through the thin gate oxide and dopant fluctuations in the short channel [5, 16]. Those limits were mainly related to the technological issues and were overcome very soon [14]. In the early 1990's, 100-nm was thought to be the limit because of many expected difficulties in reducing the physical parameters of the transistors [5, 16]. Therefore, in early 1990's, the definition of a clear roadmap to anticipate the evolution of the market seemed to be necessary. In 1993, the Semiconductor Industry Association (SIA) introduced the National Technology Roadmap for Semiconductors (NTRS) as the future IC roadmap. Later, in 1998, the SIA with its European, Japanese,

Korean and Taiwanese created the first global roadmap, being called as the International Technology Roadmap for Semiconductors (ITRS) [17].

The ITRS is an industrial consensus of future semiconductor technology that is updated every two years [17]. Figure 1.1 shows the ITRS 2007 edition. The ITRS-2007 predicts that the silicon technology will continue its historical advancing rate with the Moore's law for at least a couple of decades [15] (Figure 1.1). With this trend, the silicon gate oxide will be scaled down to its physical limit. It is predicted that feature sizes will continue to shrink down to at least the 18 nm node at 2018 [15]. At that node, the half of the center-to-center (pitch) of first level of interconnect is 18 nm and the width of the resist feature for the gate electrode is 12 nm; the etched gate electrode is even smaller, about 7 nm [18]. Figure 1.1 illustrates these limits on the roadmap.

The mission of the ITRS is the definition of the near and long-term technology requirements for the semiconductor industry as well as the description of potential technical solutions to meet these needs [19].

There are different challenges for the further downscaling of the devices, which are described according to the "near term" (2007 through 2015) and the "long term" (2016 through 2022) time-frames of the Roadmap [15]. For the "near-term" scaling, performance enhancements can be achieved with the introduction of new technologies and materials at least for another 10 years and furthermore with that of three dimensional structures [15,16]. Several achievements in finding new materials and developing new process for sub-100 nm device manufacturing have been made recently. Some of these processes or materials can be listed as [16]: the elevated source/drain [20–22], plasma doping with flash or laser annealing [23–25], NiSi silicide [26,27], strained-Si channel for mobility enhancement [28–30], Silicon on Insulator (SOI) [31–33], three-dimensional structure [34–37], high dielectric constant

(high-k) gate insulator [38–42], metal gate [43, 44], and low dielectric constant (low-k) inter-layer insulator for interconnects [45, 46].

Based on the ITRS-2007 statement [15],

“reduction of the gate oxide thickness has emerged as the most difficult challenge associated with the future device scaling, which is required for performance improvement.”

More than the technology requirements, the ITRS introduces modeling of chemical, thermochemical and electrical properties of new materials as the other most important challenge [15]. Among the difficult modeling and simulation challenges, ITRS includes the necessity for predictive modeling of dielectric reliability, breakdown (BD), and leakage currents through the gate dielectric stacks [15]. This Ph.D. thesis mainly focuses on proposing such a modeling of dielectric breakdown and simulation.

1.1 Motivations for this Thesis

Thinning of the MOSFET’s gate dielectric to sub-10 nm in nanoelectronic industry has resulted in several technological issues [3]. The oxide thinning leads to a large increase of the gate leakage current which ends up with faster gate oxide breakdown, and has caused serious reliability problems. The oxide reliability is currently considered as one of the most restrictive factors in CMOS scaling. Especially for ultra-thin oxides, the appearance of a new breakdown phenomenon, called soft-breakdown², has raised questions about the

²Soft breakdown is a low conduction state following a long-term stress that is always followed by a catastrophic breakdown with high conduction state, see chapter 2.

long-term reliability projections. Stress-induced leakage current (SILC)³ is also a major reliability concern for the non-volatile memory technology, which exploits tunnel oxides to program the device.

The present thesis investigates potential models of soft breakdown and SILC, in order to gain an understanding and improve the reliability evaluation and projection methods. It is attempted to use the percolation theory as a unified model to explain the soft and hard breakdown, and also the stress induced leakage current (SILC). Such a unified model has not been proposed yet, and will help to better understand the breakdown phenomenon.

The next objective is to analyze the effects of oxide size and applied stress on the breakdown characteristics. Understanding these effects and their contributing factors are useful for explaining the experimental results and proposed methods to project reliability from accelerated test conditions.

In addition to the percolation model, in my research, I use Markov chain⁴ to model the electron transport inside the oxide. The goal here is to model the trap-detrap of electron as the origin of the current noise after the oxide breakdown. Markov process will also be used as a model to describe the conductance due to defected breakdown paths inside the oxide.

Finally, I introduce a quantum percolation model to describe the origin of the high-field stress induced leakage current that goes through the oxide before breakdown happens.

³SILC is defined as a low field gate leakage current following high-field stressing of thin oxide MOS capacitors, see chapter 7.

⁴Markov chain is a memoryless discrete-time stochastic process, which can model the movement of a particle in a liquid, a gas and any disordered medium. See chapter 6.

1.2 Thesis Organization

This dissertation is organized as follows:

In chapter 2 a short review of gate oxide breakdown will be presented. The soft breakdown will be introduced as the main reliability issue for ultrathin oxides. The models reported in the literature to explain this phenomenon will be reviewed. Different available reliability evaluation methods will be introduced and the methods of reliability projection will be discussed.

Chapter 3 will elaborate on the percolation phenomenon. The conductance modeling of a disordered material is discussed. Two different simulation methods, for site and bond percolation, will be introduced.

In chapter 4, oxide breakdown will be modeled using the percolation theory. The breakdown statistics will be simulated using a Monte Carlo method. Using the conductance simulation methods, proposed in chapter 3, the post-breakdown conductance will be simulated.

The effects of different parameters, such as dimension and applied stress, will be discussed in chapter 5. It will be discussed how the thinning of oxide layer and increasing the oxide area result in softening of breakdown. The behavior of different reliability factors, such as Weibull slope and time-to-breakdown under different conditions will be analyzed using the Monte-carlo method, proposed in chapter 4. We report how the simulation results are very consistent with the experiment.

Chapter 6 will introduce Markov chain theory, and the breakdown will be simulated using Markov chains. The conductance of the oxide will be calculated using simulation of a resistor network with Markov theory. The post-breakdown current noise will be simulated

considering trap-detrap of electrons inside the oxide.

In chapter 7 a quantum percolation modeling of the stress induced leakage current will be proposed. It will be shown how the SILC can be modeled as a tunneling path through the oxide.

Chapter 8 is a very short chapter summarizing the conclusions of the thesis.

In addition to these chapters, there are three appendices. In appendix A, an analytical method will be introduced to find the percolation probability for a 2-D site percolation system in a recursive manner. Closed form formulas are also derived for some special network sizes.

Appendix B will introduce an estimation of cell size in our percolation model using the experimental data.

In Appendix C, we will provide some of the MATLAB codes that have been used in simulations.

The references and index are appended at the end.

Chapter 2

Gate Oxide Breakdown

In the current Si microelectronics, gate oxide reliability and gate breakdown are some of the critical problems for transistor scaling. During the last three decades, the extrinsic oxide breakdown has been controlled by improving the fabrication processes and lowering the contamination levels. Intrinsic breakdown, on the other hand, has never been a threat at typical operating voltages. But, for the sub-100 nm technology, the oxide thickness reaches less than 5 nm and the intrinsic reliability is a bottleneck.

In this chapter, a short review of the oxide breakdown in general, focusing on the breakdown in ultra-thin gate oxides, is provided. A short history, physical models of oxide breakdown, hard and soft breakdown, and the challenges for reliability evaluation and understanding of the physics of oxide breakdown will be reviewed. This chapter is organized as follows:

- (i) Section 2.1 will review the mostly accepted physical models of oxide breakdown. Advantages and disadvantages of each model will be discussed.

- (ii) The three common methods of reliability characterization will be introduced in section 2.2.
- (iii) Oxide reliability and oxide failure statistics will be reviewed in section 2.3.
- (iv) In section 2.4, a comprehensive classification of different types of gate oxide breakdown will be provided. I will report the differences between soft and hard breakdown and the proposed models to explain soft breakdown in this section.

2.1 Physical Models of Oxide Breakdown

In MOS system, oxide breakdown was known as a loss of dielectric behavior. For ultra-thin oxides ($t_{ox} < 5$ nm), however, this definition cannot be valid, because of the appearance of a new phenomenon being called “soft breakdown”. In “soft breakdown”, the insulating property of the oxide is not damaged completely.

Currently, oxide breakdown is defined as a local increase of conductance, leading a large leakage current through the gate oxide dielectric. This increase of conductance can be abrupt or gradual, depending on different parameters such as oxide thickness, area or stress conditions.

Understanding the physics of oxide breakdown is very critical for the development of a model to describe the dependence of breakdown on different controlling parameters such as temperature and electric field. Such a model is necessary to extrapolate lifetime from accelerated test conditions. Currently, it is generally accepted that oxide breakdown is due to oxide degradation and accumulation of defects inside the oxide [47]. There are different physical models proposed to explain the process of defect generation inside the

oxide which lead to oxide degradation and final breakdown. The most accepted models are “Thermochemical model” [48], “Anode Hole Injection (AHI) model” [49–51] and “Anode Hydrogen Release (AHR)” [52–56] model.

2.1.1 Anode Hydrogen-Release Model (AHR)

Since 1989, it has been recognized that exposure of bare SiO_2 to hydrogen atoms, even in the absence of any electric field, produces electrically active defects such as paramagnetic interface defects, diamagnetic interface defects (slow and fast defects), and bulk electron traps [52–56]. These defects are similar to those being generated by applying voltage stress to oxide layer. Since then, “Hydrogen-Release Model” has been accepted as a model to explain the process of defect generation inside the oxide which follows degradation and breakdown of the oxide [47, 57].

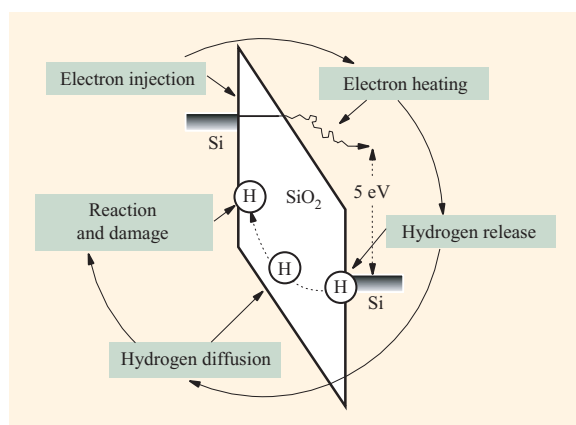


Figure 2.1: The process of defect generation by the Hydrogen Release Model [58]

In this model, it is assumed that energetic tunneling electrons release hydrogen from the anode interface. Hydrogens atoms, then, diffuse into SiO_2 and generate defects. Figure

2.1 schematically illustrates this process [58].

The desorption rate of hydrogen atoms from Si surface has been measured as a function of incident energy of the electron [59]. It has been shown that the voltage dependence of defect generation rate is very similar to electron energy dependence of the hydrogen desorption rate [59]. This fact is considered as a strong support for the model.

The major disadvantage of AHR model is its inability to explain hydrogen isotope effects. It is reported that deuterium-annealed devices show some isotope effects on the release of hydrogen from the Si interface [60,61]. However, experiment results indicate that Q_{BD}/T_{BD} does not improve if deuterium is used to passivate Si/SiO₂ interface [62]. Q_{BD} (charge-to-breakdown) is a measure of gate oxide reliability which is defined as the total charge needed to be accumulated in the oxide to initiate the breakdown. T_{BD} (time-to-breakdown) is the time taken for the oxide to fail while applying a constant stress. The charge-to-breakdown is generally determined through injecting the constant current into the oxide and measuring the time-to-breakdown. Such a fact has caused some arguments against the Hydrogen Release model. Although the breakdown has not been improved, a suppression of Stress Induced Leakage Current (SILC) was reported for the deuterated oxide films [63], and the issue of isotope effect is still not fully understood or explained.

The most important advantage of AHR model is that it explains the process of defect generation even at low voltages where MOSFETs operate. The defect generation process through AHR model has a threshold voltage of 5 volts, and can continue in the subthreshold region even at operating voltages (down to 1.2 V and lower) [64,65]. AHR model is currently the lowest energy process for defect generation that is identified [66].

2.1.2 Anode Hole Injection Model

The next physical model is “Anode Hole Injection (AHI)” model which is also referred to as “ $1/E$ model”. This model predicts that the lifetime is proportional to the inverse of electric field (Figure 2.3) and follows the extrapolation formula: $T_{BD} \propto \exp(-\beta/E)$, in which T_{BD} is the lifetime and the parameter β is the electric field acceleration factor. AHI model claims that Fowler-Nordheim (F-N) tunneling electrons transfer energy to the holes at anode, and breakdown is the result of injection of holes from the anode contact into the oxide [49–51]. Figure 2.2 shows such a process schematically [67]. The $1/E$ dependence of lifetime is the consequence of assuming that the Fowler-Nordheim tunneling current is the driving force for the defect generation. Anode hole injection and anode hydrogen release

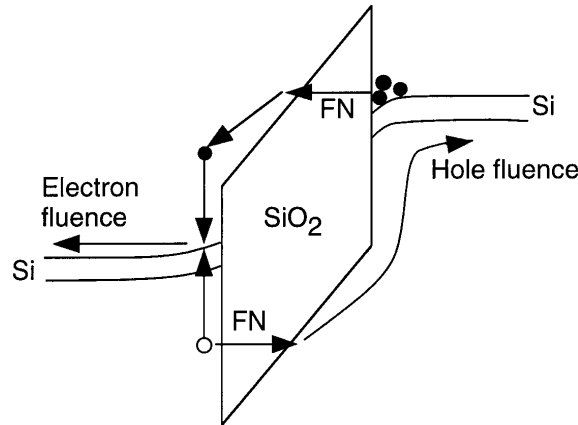


Figure 2.2: Schematic illustration of the anode hole injection model [67]

models are similar in regards that both models presume that hot electrons generate some entities (atomic hydrogen or hot holes) which diffuse back through the oxide and generate defects [66]. However, the gate voltage threshold for AHI model is 7-8 V for FETs with n+ poly-Si gates [68,69]. Therefore, it is believed that this mechanism cannot account for

defect generation at lower voltages close to operating voltages.

A recent modification of the AHI model has been proposed recently which presumes other mechanisms to be responsible for hot-hole injection and defect generation [58]. It is proposed that hole formation is possible at different voltages under different processes. For electron energy > 9 eV and thick oxides, impact ionization of hot electrons traveling through the oxide from the cathode generates holes inside the oxide [70]. For intermediate voltages, between 7 V and 9 V, it is proposed that a minority-carrier ionization, known as surface-plasmon-assisted ionization, is responsible for hole injection. The surface-plasmon-assisted process mechanism has a threshold of 7-8 V [68,71]. At low voltages, the electrons coming from the cathode create holes in p-type anode material or lightly doped inverted n-type material through a weaker minority ionization process [72–74]. Time/charge-to-breakdown in this process is expected to have an exponential voltage dependence [75], and its exponent very well fits the measured slope of $\log(T_{BD}/Q_{BD})$ versus voltage at high electric fields. The major argument against this model is that hole current at low voltages is at least 12 orders of magnitude smaller than the electron current. In AHI model, it is assumed that the defect generation is mainly due to holes and not electrons. Therefore, the defect generation rate per hole is required to be very much greater than the rate per injected electron. However, Dimaria measured the defect generation due to holes directly by injecting hot holes into the oxide [76]. He demonstrated that the measured defect generation rate value due to holes is comparable to the rate due to electrons, and is several orders of magnitude less than what is required by a minority-carrier mechanism [58,77,78].

2.1.3 Thermochemical Model

Thermochemical model [48] considers the defect generation as a field-driven process. This model is also known as “ E -model” because it explains the well-known experimental result $T_{BD} \propto \exp(-\gamma E)$, in which E is the electric field and γ is the electric field acceleration factor. This model explains that the logarithmic dependence of time-to-breakdown on linear changes of electric field (Figure 2.3).

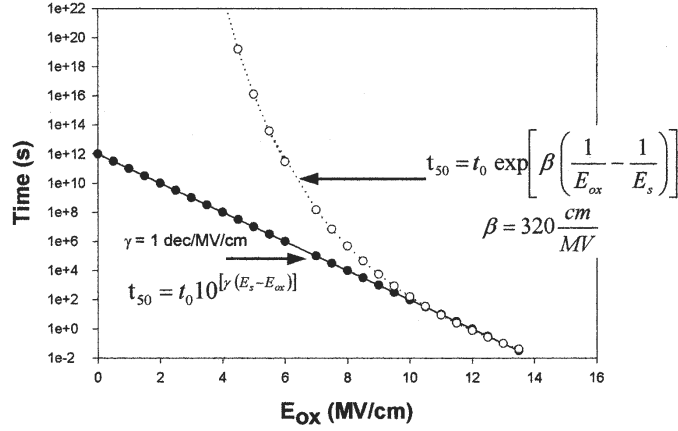


Figure 2.3: Life-time extrapolation based on E and $1/E$ models [57]

In thermochemical model (E -model), which was proposed by McPherson [48] in late 1990’s, local electric fields are said to interact with weak Si-Si bonds in the oxide, break the bonds and eventually create permanent defects. These bonds are associated with oxygen vacancies, and the defect which is created is referred to as E' center. E' center is a structure in SiO_2 having an unpaired electron localized on a silicon atom which is bonded to three oxygen atoms, instead of four, due to oxygen vacancy [57, 79]. E' centers can be easily detected with electron spin resonance (ESR) techniques [79].

Figure 2.3 shows that E and $1/E$ models lead to very different extrapolations at low

electric fields based on accelerated test data. Although both models fit the data for high electric fields, the projected lifetime for low electric field (close to realistic situations) is more optimistic in $1/E$ model (Figure 2.3).

The validation of models has been a subject of much debate for many years. To validate models, reliability tests are conducted at low electric fields over a long period of time [80,81], and at accelerated temperatures [82–85]. The data reported (Figure 2.4) shows that the linear change of $\log(T_{BD})$ with electric field (as E -model extrapolation predicts) is closer to reality. The value of the acceleration factor (γ), however, is greater than what the E -model predicts, and the researchers believe that the exponential dependence of lifetime on electric field cannot be a proof of validity of the thermochemical model [47]. The Substrate Hot Electron Injection (SHEI) experiment [76,86], thickness dependence [87] and polarity dependence [72] of oxide breakdown are the evidences against the validity of E -model.

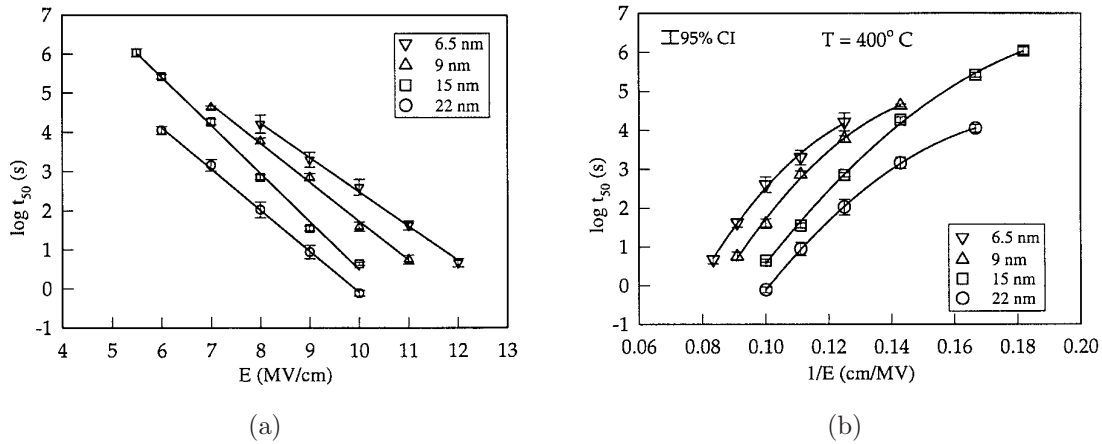


Figure 2.4: $\log(T_{BD})$ as a function of electric field (E) and reciprocal of electric field ($1/E$) based on the measurement data collected at low electric field and accelerated temperatures [83]. $\log(T_{BD})$ changes linearly with electric field (E), a good fit to E -model.

2.2 Oxide Reliability Characterization

Reliability is defined as the probability of a device performing its designated function adequately (within tolerance) for the intended period of time under the operating condition encountered [28]. The operating condition mainly means the electric field and the temperature that correspond to the normal operation of a transistor. The intended lifetime, on the other hand, could be 10 to 20 years, depending on the application [67].

The main characters that describe the reliability of a dielectric film are the “electric field-to-breakdown” (E_{BD}), the “time to breakdown” (T_{BD}) and the “charge-to-breakdown” (Q_{BD}) [88]. E_{BD} is regarded as a gross parameter that represents an estimation of the maximum electric field the dielectric film can sustain, but the film is not subjected to the wear-out kinetics that govern the degradation to breakdown. T_{BD} and Q_{BD} , as defined before, are the quantities that describe the reliability performance in “Time-Dependent Dielectric Breakdown” (TDDB).

Commonly used methods include the “Ramped Voltage Stress” (RVS), “Constant Voltage Stress” (CVS) and “Constant Current Stress” (CCS) tests. A RVS test applies a voltage which linearly increases in time on the gate electrode. Very often a staircase voltage is used instead. The occurrence of a breakdown is detected according to a leakage current. This type of stress test is used to measure E_{BD} , the maximal electric field the oxide can sustain before breakdown.

In CVS test, a constant voltage is applied to the test structure for a long time and the leakage current going through the oxide is measured by time. Breakdown is detected if the leakage current is larger than a threshold or according to a criterion of change in the leakage current. In CCS tests, a constant amount of current density is injected into

the gate electrode while the voltage evolution over time is monitored through a voltage versus time curve. Breakdown is detected if a sudden drop of voltage occurs between two consecutive stress steps.

CCS and CVS test methods are more representative of the operating conditions in a real circuit environment than a ramped stress. These test methods are used to measure T_{BD} and Q_{BD} to predict the lifetime under the operating conditions.

2.3 Breakdown Statistics and Reliability Projection

2.3.1 Choice of Probability Function for Reliability Projection

To project the reliability of oxide due to breakdown, the choice of the probability function describing the breakdown statistics is very critical. Log-normal and Weibull distributions are the two functions that have been widely used to characterize oxide breakdown statistics [67, 75, 89]. The fact that both distributions can fit the data with limited sample numbers has caused some confusion about which function is the better choice. To establish which function is the proper choice to project the reliability, Wu and Vollertsen [90] collected a large number of statistical data for oxide breakdown. In this experiment, 900 identical capacitors, being selected from a large group of more than 4000 capacitors, were stressed in substrate injection with a gate voltage of 4 V at 140°C [90]. Figure 2.5 shows log-normal and Weibull fit to the experimental data [91]. It is evident from the experiment data that the assumption of using log-normal function for reliability projection is not valid, although both Weibull and log-normal functions can fit the data with very limited samples.

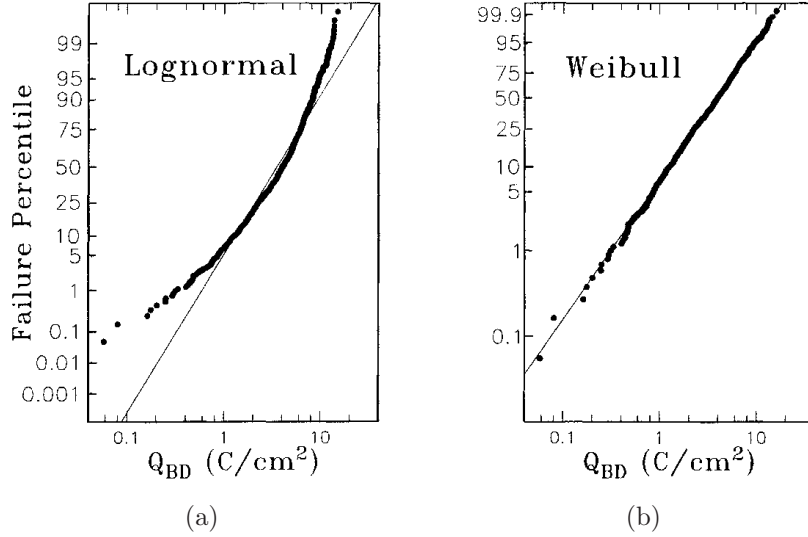


Figure 2.5: Fitting the experimental data to Log-normal and Weibull distributions [91]

Weibull Statistics

The oxide breakdown statistics can be described by the Weibull distribution:

$$F = 1 - \exp\left(-\frac{T_{BD}}{\alpha}\right)^\beta \quad (2.1)$$

in which F is the cumulative failure probability, T_{BD} is the time-to-breakdown, α is the characteristic time-to-breakdown at 63.2 failure percentile which is often expressed as “ T_{63} ”, and β is the Weibull statistics shape factor which is also known as “Weibull Slope” [90]. Weibull distribution is an “extreme-value” distribution and is appropriate for “weakest-link” type of problem. Plotting the Weibull function in the form of:

$$W = \ln(-\ln(1 - F)) \quad (2.2)$$

versus $\ln(T_{BD})$ yields a straight line with slope β (see Figure 2.5). W is called the “Weibit” function. It has been shown that oxide breakdown is a weakest-link type of problem because

device fails if any small portion of the gate area breaks down [47].

2.3.2 Area Scaling

It is found that the oxide breakdown failure probability function fits very well the Poisson model:

$$F = 1 - \exp(-DA) \quad (2.3)$$

where A is the area of the sample and D is the defect density (number of defects per unit area). Considering failure probability distribution for two sets of samples with area A_1 and A_2 to be named as F_1 and F_2 , (2.3) results in (2.4):

$$\ln(-\ln(1 - F_1)) - \ln(-\ln(1 - F_2)) = \ln\left(\frac{A_1}{A_2}\right) \quad (2.4)$$

Therefore, from (2.2), the Weibit function shifts vertically when the area changes.

2.3.3 Voltage or Field Extrapolation

It is believed that a scale factor can be used to scale a lifetime at higher voltage to a lower voltage at one oxide thickness. Using this method, the voltage acceleration rate parameter is measured at several higher voltages, then lifetime at lower voltages (i.e. operating voltages) is extrapolated from higher voltage measured data [92].

There is considerable controversy about the appropriate scaling parameter to be used. Some researchers claim that, based on the anode-hole-injection model, the logarithm of time-to-breakdown scales with $1/E_{ox}$, whereas others prefer using the E_{ox} -dependence.

According to anode hole-injection ($1/E$) model, the charge-to-breakdown can be de-

scribed as:

$$Q_{BD} = Q_0 \exp\left(\frac{H}{E_{ox}}\right) \quad (2.5)$$

where H is a constant for a fixed oxide thickness.

The E -model on the other hand predicts a linear relationship between the logarithm of the time-to-breakdown and the oxide-field:

$$T_{BD} = t_0 \exp(-\gamma E_{ox}) \quad (2.6)$$

where t_0 and γ are constants.

In the past 15 years, researchers tried to prove the correctness of either E or $1/E$ models [80, 85]. A mixed model with approximate $1/E$ dependence at high voltage and E -dependence at low voltages has been proposed being called unified $E - 1/E$ model [92].

For ultra-thin oxides, however, a power-law voltage relationship has been discovered recently. Researchers interpret this fact as a result of the ballistic electron transport through ultra-thin oxides.

2.3.4 Temperature Scaling

The T_{BD} data are often obtained at temperatures that are different from and higher than the real device operating temperature. The T_{BD} at operating conditions can only be determined when the temperature dependence is known a priori. Especially in ultra-thin oxides the temperature dependence of time-to-breakdown is very strong [92, 93]. The T_{BD} has been assumed to have an Arrhenius relationship to temperature. The activation energy of T_{BD} can be determined by the Arrhenius law which shows a linear relationship between the logarithm of T_{BD} and inverse temperature, i.e. $T_{BD} \propto \exp(E_a/k_B T)$, where E_a is

the activation energy for defect generation, k_B is Boltzmann constant in electron-volts per Kelvin and T is the absolute temperature in kelvin. However, it is found that the measured activation energy depends on oxide layer thickness [94], the voltage or field range [95] and temperature range [96] of the measurements. Therefore, the Arrhenius dependence of T_{BD} on temperature has been questioned. DiMaria [97] explained this non-Arrhenius temperature dependence as a combined result of the temperature dependence of the defect buildup in the oxide films and the critical defect density (N_{BD}).

Suehle et al. on the other hand performed a thorough investigation of the temperature dependence of the progressive BD rate [98]. They showed that their data fit much better with a non-Arrhenius exponential form compared to Arrhenius law. The temperature acceleration appears independent of voltage [98].

The undefined dependence of T_{BD} on temperature complicates the temperature extrapolation of time-to-breakdown, and it is appreciated to measure the T_{BD} at the device operating temperature [92].

2.4 Soft and Hard Breakdown

In 1992, Fukuda et al. [99] showed that oxide breakdown (BD) in ultra-thin (sub-5 nm) oxides exhibits different characteristics compared to oxides thicker than 5 nm. Usually, this new BD mode is distinguished by post-breakdown current of orders of magnitude less than the previously recognized oxide BD. For the lower conductivity and for being less destructive, this new BD mode is called “Soft Breakdown (SBD)” [100]. Other titles such as “quasi” [101,102]. “partial” [103] or “non-destructive” breakdown [104] have been also used to describe this phenomenon. The soft breakdown with low conduction state,

is always followed by a catastrophic breakdown with high conduction state, being called “Hard Breakdown (HBD)”. A physics-based definition for the soft and hard breakdown is still lacking, and there is no consistent choice of how to classify the breakdown to SBD and HBD.

It is revealed, by combined electrical and optical measurements, that the differences between SBD and HBD post-breakdown current is due to the size of the BD spot. Based on such a fact, Degraeve [92] defined the soft breakdown as an oxide breakdown without lateral propagation of the breakdown spot due to thermal damage.

2.4.1 Different Types of Soft and Hard Breakdown

Although a physics based classification of HBD and SBD is still lacking, based on experiments, six different types of breakdown has been realized by now [105]. Based on the data reported in different articles, SBD can be classified into three different categories of analogue SBD (A-SBD), digital SBD (D-SBD) and micro-breakdown (MB) [106,107]. A-SBD is recognized by random noise, while D-SBD is identified by a telegraph switching pattern. Micro-breakdown , on the other way, is recognized by a much smaller current than typical SBD current, and is not detectable in large area samples. HBD is also classified into two main groups of high-HBD and low-HBD, which are associated to HBD with and without thermal propagation, respectively. Recently, another HBD mode has also been recognized which is called non-linear HBD (NL-HBD). NL-HBD is a high-HBD with a non-linear post-breakdown I-V characteristics.

2.4.2 Differences and Similarities of Soft and Hard Breakdown

Post-Breakdown I-V Characteristics

One of the main differences of soft and hard breakdown is the difference in their post-breakdown I-V characteristics. Till recent years, an in-depth research investigation has not been done about the post-BD current behavior. Recently, it has been found that the post-breakdown I-V characteristic after the occurrence of hard breakdown does mostly have a resistance-like behavior for small values of applied voltage, while for large voltages the background F-N tunneling characteristics reappears. For soft breakdown, on the other hand, a more in-depth research has been done. Based on the observations, post-SBD current is reported to fit power-law [108, 109] or exponential [102, 110] function of the applied voltage, and yet it is still not quite clear which model is correct. Some researchers believe that the I-V follows both characteristics depending on the range of voltage [105]. Measuring the normalized post-BD conductance for a wide range of voltages, it has been found that for small ranges of voltage ($V \leq 3$), I-V fits power-law characteristic, whereas for the larger voltages it follows the exponential characteristics [111].

Noise Characteristics

Both SBD and HBD post-BD currents have a noisy component. It is believed that the cause of such a noisy current is the trapping-detrapping of electrons within the oxide. It is reported that the noise spectrum after SBD has a $1/f^\alpha$ characteristics, where f is the signal frequency, and α is a constant between 1 and 2 [112]. For HBD, however, the low frequency noise is supposed to be the result of contribution of several fluctuators, and it is characterized by a few Lorentzian components [113].

Substrate Current after Breakdown

Monitoring the substrate current after breakdown is a well-known technique, being called carrier-separation method, to determine the dominant carrier type of the gate leakage current [105]. Crupi et al. [114, 115] reported a large increase of substrate current after both HBD and SBD. They observed a plateau in the substrate current that was ascribed to a generation-recombination mechanism of electron-hole pairs in the space charge region close to the Si-SiO₂ interface. Similar plateaus in the substrate current after SBD have been identified by other researchers [116, 117]. DiMaria et al. [69] claimed that the increase of measured substrate current at low voltage was the result of tunneling of holes through oxide back to cathodes which are generated from anode hole injection mechanism. Photo-excitation of electrons, due to photon generation by hot electrons in the gate, is the other mechanism that is proposed as a cause of substrate hole current [118].

Thickness Dependence of SBD and HBD

Two statistical parameters of Weibull statistics, the shape factor (β) and the time/charge to breakdown (T_{BD}/Q_{BD}), change as a function of oxide thickness (t_{ox}). Figure 2.6 shows that for every 0.1 nm reduction in t_{ox} , T_{BD} decreases roughly four-folds [91]. The thickness dependence of T_{BD}/Q_{BD} is believed to be the result of reduction in critical defect density by decreasing t_{ox} .

Figure 2.6 shows that scaling down the oxide thickness from 4.2 nm to 2.3 nm results in decrease of T_{BD} by seven orders of magnitude, and reduction of Q_{BD} by four orders of magnitude.

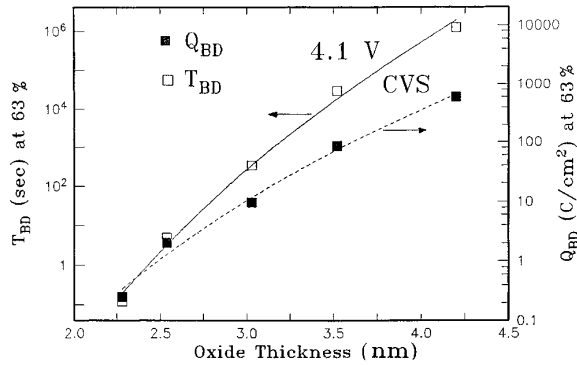


Figure 2.6: T_{BD} and Q_{BD} versus t_{ox} at 140°C and $6.2 \times 10.4 \text{ cm}^2$ [91]

2.4.3 Physical Models for Soft Breakdown

Tunneling

Different authors have used quantum tunneling as a model to explain SBD post-breakdown I-V characteristics. Direct tunneling [101], trap-assisted tunneling [100], and resonant tunneling [119] are among the most accepted tunneling models. Lee [101] proposed to model SBD current as a parallel Fowler-Nordheim and direct tunneling currents. In this model, it is proposed that SBD can be the result of a progressive degradation of a localized region close to the anode interface, and the reduction of the effective thickness at a localized region. The thinning of the oxide at the physically damaged region, and direct tunneling through the thin localized damaged region has been considered as the origin of SBD [101].

Variable Range Hopping

In 1997, Okada et al. [120] proposed that a Variable Range Hopping (VRH) model can be used to explain the temperature dependence and noisy fluctuations of soft breakdown. Mott variable range hopping is a model describing low temperature conduction in strongly

disordered systems with localized states [121]. Mott's theory of VRH conduction model predicts that current can be explained as a function of $T^{-1/4}$, expressed as below:

$$I(T) = A \exp(-BT^{-1/4}) \quad (2.7)$$

$$B = 2.06(\alpha^3 k_B N^{-1/4}) \quad (2.8)$$

where I is the current, T is the temperature, k_B is the Boltzmann's constant, A is a constant, α is the decay length of the localized states and N is the density of the localized states available for carrier conduction.

Considering the conduction to be due to localized states and traps inside the insulator and the interface states, Okada explains that the temperature dependence of post-SBD very well fits the VRH expression.

Percolation

Houssa et al. [109] modeled SBD based on percolation theory. In the percolation theory, traps randomly occupy the oxide and finally form a conducting path which spans between the two electrodes, and causes the oxide breakdown. In Houssa's model, the insulating oxide is modeled as a network of non-linear conductors with different percolation thresholds. The individual conductors are assumed to have a power-law I-V characteristic of the form $V = rI^\alpha$ where r and α are constant. It is shown that with such an assumption, the random network I-V curves follow a power law with the same exponent ($\alpha \approx 0.32$). The exponent α was extracted from the measurements data that were obtained in the range $0.5 < V_g < 3V$. Later, Houssa extended the model to explain the temperature dependence and the noisy behavior of SBD [122, 123]. The scattering of electrons in the percolation

path is considered as the origin of the temperature dependence, while the noise is modeled because of fluctuations caused by random switching in the percolative network.

Quantum-Point Contact Model

Suñé and co-workers [124–126] modeled SBD by Quantum Point Contact (QPC) mechanism. In QPC model of breakdown, the breakdown path across the oxide is treated like an atom-sized constriction [105]. Because of the lateral confinement of the wave function, the electron transverse momentum becomes quantized, the tighter the confinement the higher the energy levels within the structure. The increase of the energy levels gives rise to conduction sub-bands which act as potential barriers. According to QPC, these barriers determine whether SBD, HBD or NL-HBD happens [105].

2.5 Summary and Conclusion

In this chapter, a short review of oxide breakdown, as a reliability concern for sub-100 nm CMOS scaling, was presented. The physical models of oxide breakdown such as thermochemical model, hydrogen release model, and anode hole injection model were reviewed.

The basics of reliability evaluation and the oxide breakdown statistics were reviewed. Time-dependent dielectric breakdown tests (CCS and CVS) were discussed as the common techniques of reliability evaluation. The area-scaling, temperature-scaling and the voltage-extrapolation, as the methods of reliability projection from accelerated test conditions, were explained.

The soft breakdown was introduced as the serious reliability issue for ultra-thin oxides. There are differences and similarities between the soft and hard breakdown, which were

discussed. The precise and distinguishing origin of soft breakdown is not known yet. However, different phenomenological models have been proposed to explain this phenomenon. In this chapter, we reviewed the proposed models.

Chapter 3

Percolation and Phase Transition

3.1 Introduction

Percolation theory refers to a class of stochastic models generally describing the flow of material through a porous medium. In this chapter, a short critical review of percolation theory will also be presented. The phase transition and critical phenomena will be reviewed. Then, introducing the mostly accepted models of electrical conduction of a disordered material, I will present the two models that I have developed to calculate the conduction of percolation path. One model calculates the conductance by simulating the material as a network of parallel and series resistors, being a good model for site percolation. This model will be used in chapters 4 and 5 to calculate the post-breakdown conduction in oxides. The other model to be discussed is based on a bond-percolation, which is basically modeling the material as a network of bonds being conductive and non-conducting with some probabilities. The results of the two simulation methods will be compared.

This chapter is organized as follows:

- (i) A short history of percolation theory, the concept of percolation and different applications of percolation theory will be reviewed in section 3.2. The site and bond percolation models will be discussed.
- (ii) In section 3.3, the concept of phase transition and its modeling with percolation will be studied.
- (iii) The section 3.4 will present a short review of the concept of conductivity in disordered systems. The models that I have developed for calculation of percolation path conductance will be introduced in sections 3.4 and 3.5.

3.2 Percolation

3.2.1 History

The history of percolation theory goes back to the 1940's, when Flory [127] and later, Stockmayer [128] used percolation to describe how polymerization phenomena may finally lead to “gelation”. In their model, during polymerization, small branching molecules begin to form larger and larger macromolecules if more and more chemical bonds are formed between the original molecules. “Gelation” is said to occur as soon as a network of the formed chemical bonds spans the whole system [129].

The term “percolation”, however, was first introduced by Broadbent and Hammersley [130] in 1957, using the example of a porous stone immersed in a bucket of water. They were the first researchers who treated percolation mathematically [129]. Thereafter, the advent and development of computer technology led to a huge progress in percolation theory.

The relationship of percolation to critical phenomena was only emphasized since the 1970's (Essam and Gwilym [131].) Percolation theory, currently, covers a wide range of applications, from modeling of fluids in porous media [132] to the study of the effect of dopants in semiconductors [133], modeling of thermodynamic phase transitions [134, 135], and even a way to understand different events such as propagation of forest fires [136–138].

3.2.2 What is Percolation?

One of the best ways to understand “percolation” is to know its difference with the well-known transport mechanism of “diffusion”. An example of diffusion is the motion of one molecule in a gas as scattered by other molecules. Soaking of a fluid into a porous medium can be considered as a good example of percolation process. Diffusion, such as moving of a molecule through gas, is a “memory-less” random process [139]. It means that, when the gas is sufficiently dilute, the last collisions do not have effect on the current scattering. Percolation, however, has memory effects. It means that the random scattering of the particles in the fluid must be treated as a property of the medium.

Figure 3.1 shows a one-dimensional Polya-walk which is a good illustration of the difference between percolation and diffusion [140]. When the random mechanism is assigned to the fluid particles, a particle steps to the left or right with equal probability but randomly. The result is that, as shown in Figure 3.1a, the particle will visit every lattice point if the process is allowed to continue indefinitely. This is a diffusion process. On the other hand, Figure 3.1b shows the case that the random mechanism is assigned to the medium of the lattice points. Suppose that the lattice points are initially assigned with arrows randomly but with equal probability on the directions of the arrows. The direction of the steps of

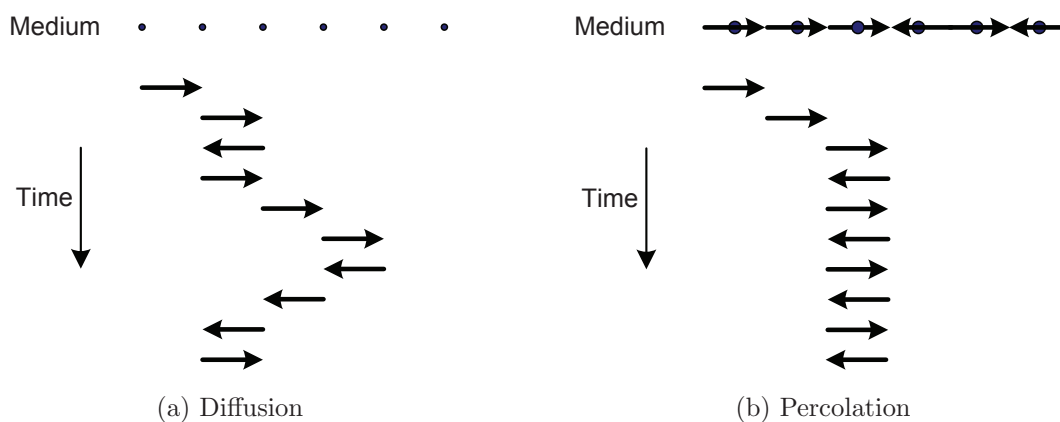


Figure 3.1: One-dimensional Poly-walk; In diffusion the walk is directed by random scattering and in percolation the walk is controlled by the random medium [140].

the particle at a certain lattice site is agreed to be the direction of the arrow associated to the lattice point. It will be drastically different from that of the previous process. The particle will be trapped somewhere and could not visit every lattice point. This should be the case of percolation [139, 141].

3.2.3 Mathematical Definition

Broadbent and Hammersley [130] introduced the 2-D percolation problem as below:

Definition 3.1 (2-D Percolation Problem). *Considering \mathcal{L} to be the graph in the plane whose vertices are the integral vectors (i.e. elements of \mathbb{Z}^2) and whose edges or bonds are the segments connecting two adjacent vertices (the two vertices v' and v'' of \mathcal{L} are called adjacent if the distance between them equals 1). Let each bond of \mathcal{L} be open or passable with probability p , and closed or blocked with probability $q = 1 - p$, and assume that open or closedness for all different bonds is chosen independently. The percolation probability is*

defined as

$$\theta(p) = P\{\text{the origin is part of an infinite connected open set in } \mathcal{L}\}$$

This definition can be easily expanded to a \mathbb{Z}^d lattice (\mathbb{Z}^d is a set of all vectors $x = (x_1, x_2, \dots, x_d)$ with integer coordinates). For this purpose \mathbb{Z}^d is turned into a graph, called the *d-dimensional cubic lattice* [142]. The distance between any two points of the graph is defined by:

Definition 3.2. *The distance $\delta(x, y)$ from $x \in \mathbb{Z}^d$ to $y \in \mathbb{Z}^d$ is:*

$$\delta(x, y) = \sum_{i=1}^d |x_i - y_i|$$

Any pairs x, y of points of \mathbb{Z}^d are said to be adjacent if $\delta(x, y) = 1$. In the graph, an edge is added between any two adjacent points. Each edge is open or passable with probability p and closed or blocked with probability $q = 1 - p$. The term “cluster” for each vertex, and the percolation probability are defined as follows:

Definition 3.3 (Cluster). *The (open) cluster $C(v)$ of the vertex v is defined as the collection of points connected to v by an open path.*

Definition 3.4 (*d – D Percolation Probability*). *If we denote the origin of \mathbb{Z}^d as O , the percolation probability ($\theta(p)$) is defined by*

$$\theta(p) = P\{C(O) \simeq \infty \mid \text{Each edge is open or passable with probability } p\}$$

3.2.4 Site and Bond Percolation

There are two basic types of percolation models, called “site” and “bond” percolation. In bond percolation, bonds are defined between two neighboring sites on a lattice, and each

bond has a probability p to be conductive or being connected and $1 - p$ to be insulating and open (Figure 3.2a). In site percolation, however, a lattice of sites (cells) is defined in which every lattice site has a probability p to be “filled” and a probability $1 - p$ to be “empty” (Figure 3.2b). Although Definition 3.4 seems to define a bond percolation, it can also be realized for site-percolation analysis by considering edges between any two adjacent sites. Then, each edge is open if both the cells are filled and it is closed (blocked) otherwise (i.e. if any of the neighboring sites is empty.)

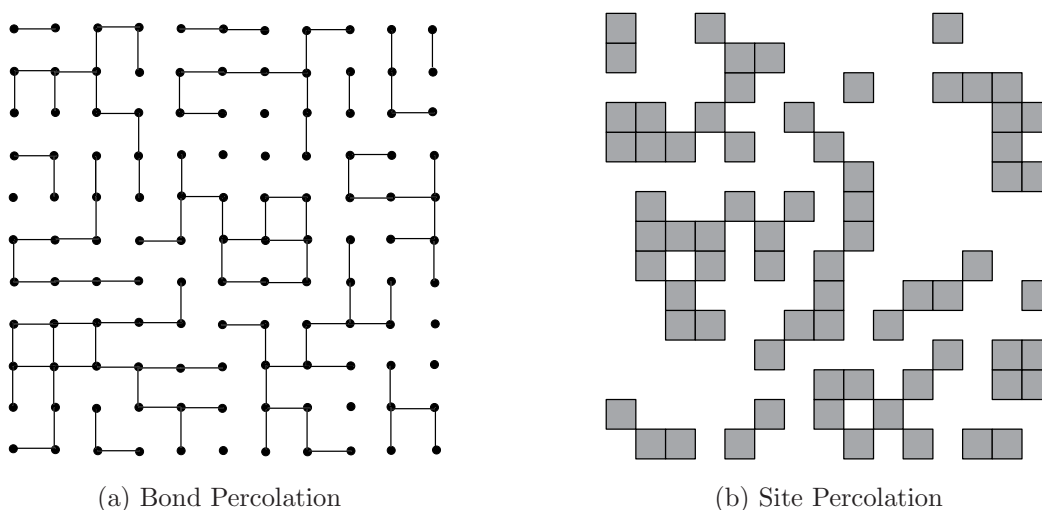


Figure 3.2: Site and Bond Percolation

In both site and bond percolation cases, clusters are defined as structures of connected points in a way that it is possible to create a path between any two points of the cluster (Definition 3.3). As the probability p is increased, larger clusters will be formed. Eventually, a cluster which has a path that spans the whole system will be formed. If the lattice is infinite in extension, the size of this particular cluster would be infinite. It is fundamental

to the percolation theory that there exists a critical value p_{crit} of p such that

$$\theta(p) \begin{cases} = 0 & \text{if } p < p_{crit} \\ > 0 & \text{if } p > p_{crit} \end{cases}$$

p_{crit} is called the critical probability and is defined by

$$p_{crit} \triangleq \sup\{p : \theta(p) = 0\} \quad (3.1)$$

In the case of periodic or infinite lattices, the existence of a diverging quantity, namely the (average) cluster size, at a specific, finite value of a parameter, and the qualitative change in the behavior of the system after crossing this value tell us that one should look for critical behavior [143]. In fact, near p_{crit} , several quantities exhibit power-law behavior, and there are scaling laws relating the different critical exponents.

3.3 Phase Transition and Critical Phenomena

In physics, a phase transition is defined as the transformation of a thermodynamic system from one phase to another [144]. The distinguishing characteristic of a phase transition is an abrupt change in one or more physical properties, in particular the heat capacity, with a small change in a thermodynamic variable such as the temperature. The transitions between the solid, liquid, and gaseous phases (boiling, melting, sublimation, etc.), the transition between the ferromagnetic and paramagnetic phases of magnetic materials at the Curie point, and the emergence of superconductivity in certain metals when cooled below a critical temperature are some of the examples of phase transitions [129].

Percolation is one of the simplest models which explain a phase transition, and the occurrence of a critical phenomenon is quite central to the appeal of percolation [142].

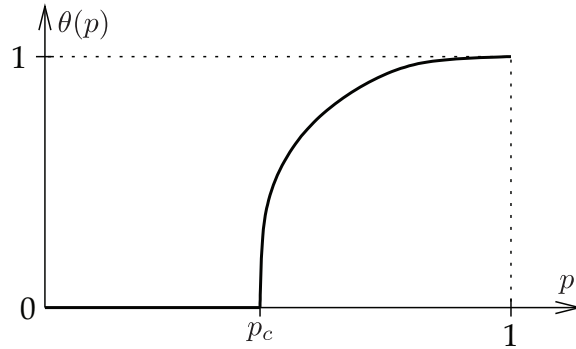


Figure 3.3: The behavior of $\theta(p)$ around the critical point (for bond-percolation)

One of the most interesting topics in the area of phase-transition is metal-insulator transition. In this phenomenon, the material, near the metal-insulator transition, consists of the localized charges surrounded with metallic phase medium. When the density of localized charges is lowered, the material transitions to the insulating state, and the proportion of the localized charges increases while the metallic phase disappears. It strongly suggests that the metal-insulator transition is connected with the microscopic restructuring inside the system, and is a percolation transition between the two phases [145, 146].

In this thesis, I have studied the oxide breakdown and interpreted it as a metal-insulator transition (see chapter 5). I demonstrate that for ultra-thin oxides, the nature of transition changes to a quasi-critical rather than critical, and a gradual breakdown occurs as observed in experiments.

3.4 Percolation and Electrical Conduction

In 1968, Ziman [147] proposed a theory, that in disordered systems, the electron mobility must be dependent on the percolation probability. Later, this theory was used to calculate the hopping electrical conductivity of semiconductors [148]. Ziman's theory was based on the concept that the localized areas in a disordered system act as traps and affect the electron mobility. If Ziman's theory was correct, however, after the critical defect density, a sharp transition in the conductance of the material must occur. In 1971, Last and Thouless [149] conducted a simple experiment and measured the conductance of a sheet of graphite paper which was randomly hole punched, with different density of the holes, and showed that the conductance varies much less sharply than the percolation probability after the transition. The reason for the smooth transition of the conductance is that near the p_{crit} , lots of the paths, available for the conductance, are dead ends or contribute less in conduction. Therefore, it became clear that the idea of linear dependence of mobility on the percolation probability may not be a valid model. In 1973, Kirckpatrick [150] developed a model for the percolation path conductance, by modeling the disordered material as a network of resistors, and calculating the distribution of potentials in the network due to both external and local electric field. According to this model, the conductance of the percolation path conductance fits very well with the relationship $(p - p_{crit})^n$ outside the critical region, where n is about 1.5 to 1.6.

3.5 Modeling of Percolation Path with a Parallel-Series Network of Resistors

The model proposed by Kirckpatrick [150] is mainly based on the bond percolation. Here, I have developed a simple model to calculate the percolation path conductance based on the site percolation, which will be used in chapter 4 for simulation of the breakdown. The percolation path is established when a defect cluster develops and spans the distance between the two electrodes. Therefore, by applying electric field across the two electrodes this cluster can conduct electron from one electrode to the other electrode. I assume that, when the electrical stress is applied, the defects in the percolation path become oriented with the external electric field. In this way, all the defects can be modeled as the resistors conducting current. In this model, a constant conductance is assigned to each defect that is part of the percolation path. The defects that are part of a dead end path and the non-trapped sites are assumed as perfect insulators, because they do not have much contribution in material's conductance after the transition.

With modeling of the defects as resistors, a network of resistors is made. When an electrical stress is applied, the same stress is applied to the horizontally-connected cells, and the current is branched through them. Therefore, one can model the horizontally-connected cells as parallel resistors (Figure 3.4b). In the same way, the vertically connected cells are modeled as series resistors (Figure 3.4a). I assume that all the percolation paths in the square lattice network can be modeled as rows of parallel resistor cells that are located in series.

Depending on the number of the cells that are in parallel, more current can go through the path and the conductance between electrodes increases. If any of these horizontally

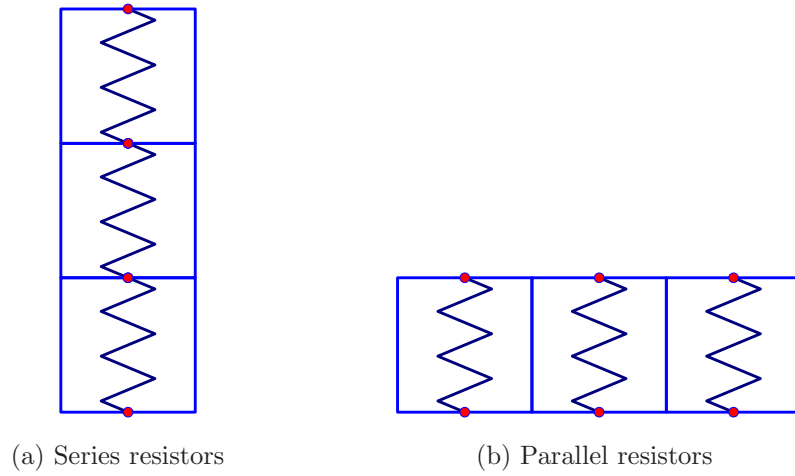


Figure 3.4: The vertical and horizontal sites are modeled as series and parallel resistors.

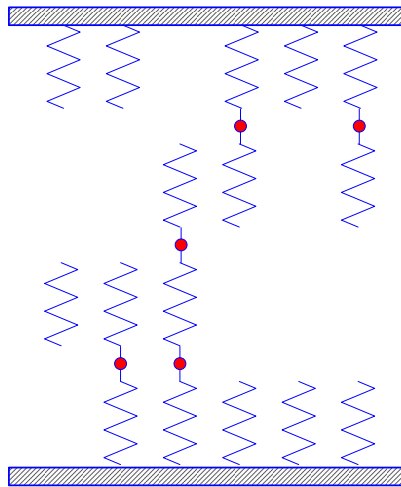


Figure 3.5: The proposed model to calculate the conductance of the percolation path. In this model the percolation path is considered as a bunch of parallel resistors placed in series to form a current path between the two electrodes.

connected cells are blocked vertically, it is assumed that a very small current passes across it and it has a small contribution in conductance. Therefore, these defects are not considered in the group of the parallel resistors.

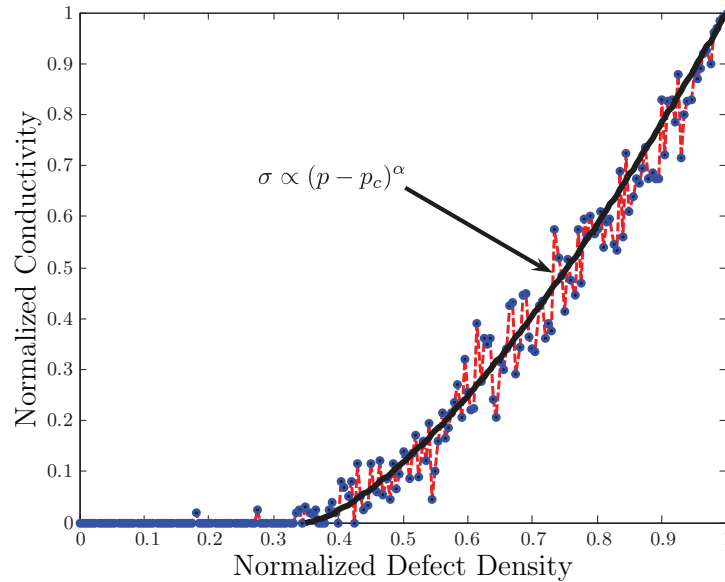


Figure 3.6: Conductance versus the defect density calculated using the parallel-series resistor network. Conductance changes as a power-law function of defect density ($\sigma \sim (p - p_{crit})^\alpha$ where $\alpha \simeq 1.5 - 1.6$).

Figure 3.5 shows a view of the schematic modeling of the percolation path. This parallel-series modeling of the network turns about to be a good way of approximation for the current going through. In Figure 3.6, the simulated conductance as a function of defect probability is plotted. The results match well the Kirckpatrick [150] power law result.

3.6 Modeling of Percolation Path conductance with a Network of Resistors

In this section, the disordered medium (defected oxide) is modeled as a network of resistors. In this modeling, each site in the percolation network is considered as a node in an equivalent resistor network (Figure 3.7). Here, the filled cells in the lattice (Figure 3.8a) are named traps, and the empty sites are called the nontrap cells. The resistance R_1 is then used to model both nontrap-nontrap and trap-nontrap junctions while trap-trap junctions are replaced with resistance R_2 . The top row nodes are all assumed to be connected together and to the same input voltage V_{in} . The bottom row nodes are connected to ground by a resistance R_1 or R_2 depending respectively on whether it is a nontrap or trap. Figure 3.8b depicts the network of resistors corresponding to the trapped network of Figure 3.8a.

Modeling the trapped network with a resistor network makes it easy to analyze its equivalent resistance (or conductance). Specifically, the input unit current $I_{in} = 1$ is applied through the node V_{in} and the resulting voltage V_{in} is computed. Alternatively, the input voltage can be set and then the input current is computed. Either approach can be used since they will give same result for $R_{eq} = V_{in}/I_{in}$.

Here, the first approach is followed which leads to 'node equations'. Each node i is assigned a voltage v_i . A node equation is simply a KCL for a specific node. Since the nodes are connected to each other by resistors, the current of each branch can be expressed as linear combination of the voltages at its two ends, $I_{i \rightarrow j} = G_{ij}(v_i - v_j)$, where $G_{ij} = 1/R_{ij}$ is the conductance between nodes i and j . Therefore, a typical node equation is as follows:

$$\sum_{j \in S_i} G_{ij}(v_i - v_j) = \sum_{k \in C_i} I_{k \rightarrow i} \quad (3.2)$$

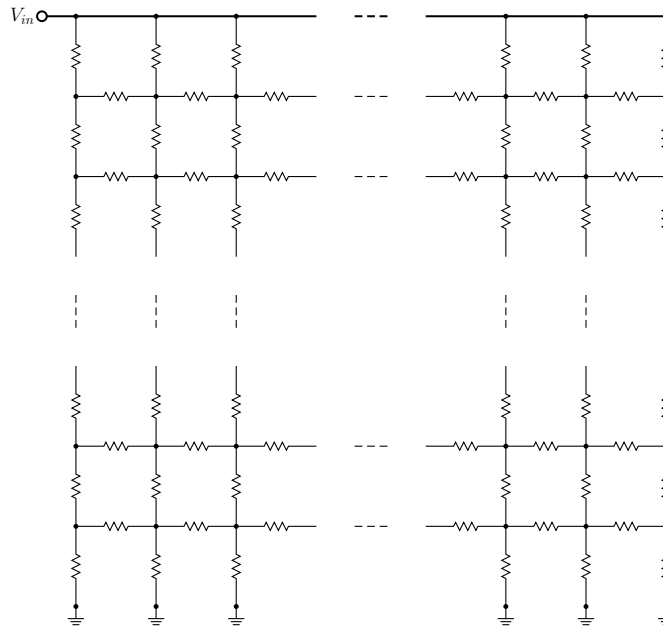


Figure 3.7: The percolation network is considered as a resistor network, with the two top and bottom rows directly connected to the electrodes.

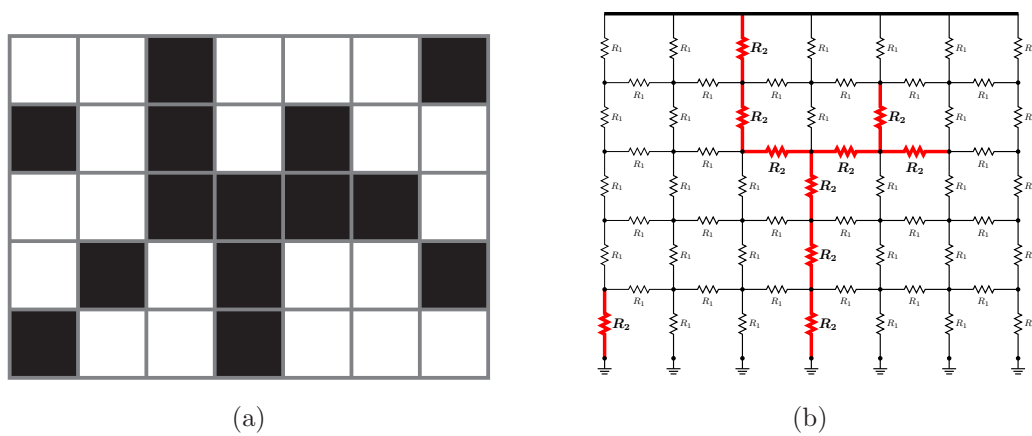


Figure 3.8: A randomly trapped network and its equivalent resistor network; R_1 and R_2 are the resistances of open and closed bonds, respectively.

where S_i is the set of all nodes which are connected to node i with resistors (neighbors of i in the original trapped network) and C_i is the set of all nodes connected to i with current sources. $I_{k \rightarrow i}$ is the value of current flowing *into* i through the k 'th current source.

Writing the node equation for *every* node and putting them altogether, we obtain a system of N linear equations with N unknowns v_i :

$$\mathbf{Y}\underline{v} = \underline{I} \quad (3.3)$$

where $\underline{v}_{N \times 1}$ is the vector of node voltages and $\mathbf{Y} = (y_{ij})_{N \times N}$ (*node conductance matrix*) and $\underline{I}_{N \times 1}$ are defined as follows:

$$y_{ij} \triangleq \begin{cases} -G_{ij} & i \neq j \\ \sum_{k \in S_i} G_{ik} & i = j \end{cases}$$

$$I_i \triangleq \sum_{k \in C_i} I_{k \rightarrow i}$$

Here there is only one current source connected to the uppermost node (node 1). Therefore, $\underline{I} = (1, 0, \dots, 0)^T$.

Compared to the parallel-series network model which was proposed in section 3.5, this model has the advantage of being easily used for higher dimension networks. I have used this model to simulate the conduction inside the 3-D trap networks, while the simple model of parallel-series network was used for 2-D networks.

3.7 Summary and Conclusion

In this chapter, the percolation introduced as a simple model to explain phase-transition phenomena. The two models of site and bond percolation were reviewed. It was discussed

how the percolation theory can be exploited to find conductivity in disordered materials. Introducing two resistor network models, we calculated the conductance.

Chapter 4

Percolation Modeling of Oxide Breakdown

4.1 Introduction

In this chapter, oxide is modeled with a 2-D network of square cells. It is assumed that breakdown is the result of continuous degradation of oxide and generation of defects inside the oxide. Then, oxide breakdown is modeled as the creation of a percolating path of defects inside the oxide which conducts a huge current between electrodes, and causes the breakdown.

This chapter is organized as follows:

- (i) Section 4.2 describes the 2-D percolation model that is developed to simulate the creation of a breakdown path inside the oxide.
- (ii) CCS and CVS test methods are simulated in section 4.3.

- (iii) In section 4.4, the breakdown statistics is investigated through failure analysis of 50 different samples. The breakdown is considered to be the result of accumulation of defects inside the oxide undergoing a constant stress. The oxide reliability and lifetime are then estimated based upon the statistical simulation. Finally, the post-breakdown current will be calculated using the percolation conduction model introduced in section 3.5.

4.2 Modeling of Oxide as a Network of Molecular Cells

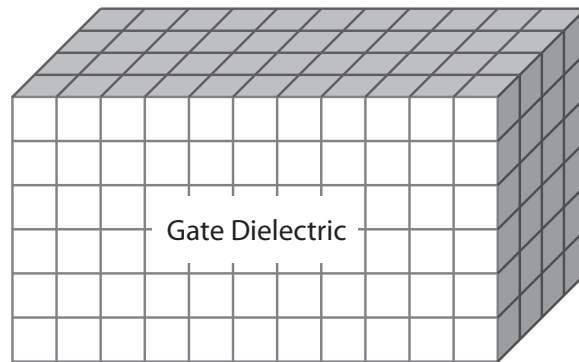
In order to model the oxide breakdown, one can start by assuming that a layer of SiO_2 dielectric is placed between two electrodes, as in a metal-insulator-metal capacitor or a MOS-capacitor, and is stressed electrically for a long time. Continuing to apply the stress results in the creation of defects inside the oxide. Currently, it is assumed that these defects can be the result of different physical-chemical damages, such as bond breakage, hot-hole injection or other models that have already been reviewed in section 2.1.

Although there are several physical models which have been proposed to explain the origin of these defects, there is still no agreement on the real cause of defects. However, regardless of the physics of these defects (see chapter 2), it is agreed that trapping of electrons inside the generated defects eventually leads to breakdown [47]. In simple terms, the electrons trapped inside the dielectric are localized electrons, and either cannot participate in conduction, or have a very small contribution in the conduction. But, as soon as the number and the energy of trapped electrons reach a certain critical level, they can generate

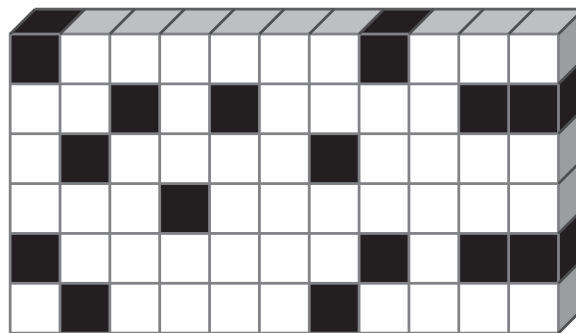
a path for the current conduction, and thus cause a significant increase of electrical current through the oxide. This phenomenon is called oxide breakdown, and the conduction mechanism can be explained by the percolation theory.

In this research, I have used a “square lattice percolation model” [129] to simulate oxide breakdown. Figure 4.1b illustrates a schematic of a 2-D structure being used to simulate the percolation. This structure represents the cross-section of the dielectric, in which the dielectric is divided into cubic cells. Based on the percolation theory (see section 3.2), in this square lattice, the cells are either “occupied” with the probability p , or “unoccupied” with the probability $1 - p$. Here, the “occupied” cells are considered to denote “defects” in the oxide, and the “unoccupied” cells denote the “cells that are not damaged”. The probability p is referred to as the “site occupancy”, which represents the defect generation probability.

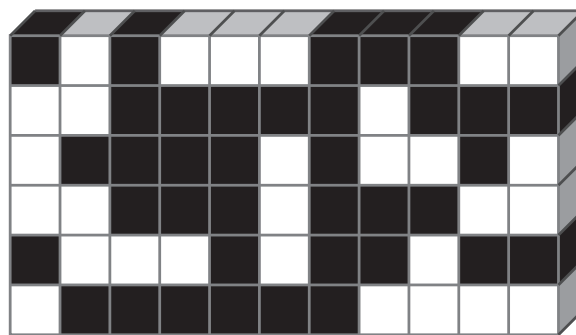
The conduction in the oxide takes place when the percolation occurs and a continuous conduction path of defects is formed between the two electrodes. Figure 4.1c shows a view of such a conduction path. In the proposed model, it is assumed, for simplicity, that the current can flow only in the vertical or horizontal direction between the cells. The current paths in inclined directions are excluded. With this assumption, the neighbor sites are defined as the two nearest sites that are placed horizontally or vertically side-by-side (mathematically called 4-connected). Any group of neighbor defective sites is defined as a “defect cluster”, and the percolation path is defined as a defect cluster which spans the distance between the two electrodes. Implementing the Hoshen-Kopelman (H-K) algorithm for cluster-counting [151], and looking for the time that at least one of these defect clusters is wide enough to span the distance between the two electrodes (Figure 4.1c), a procedure of searching for the percolation path can be formulated.



(a)



(b)



(c)

Figure 4.1: (a) SiO_2 cubic lattice, (b) Defects are created uniformly inside the oxide; the defect density is less than the critical value. (c) A percolation path is created through the defects inside the oxide.

It will be discussed in the following section how to employ the mentioned percolation model to simulate the oxide breakdown. In this simulation, the time-to-first percolation is taken as being the time-to-breakdown. The simulation procedure is based on a continuously application of stress and searching for a percolation path, which will be introduced in the next section.

4.3 Breakdown Modeling

The time dependent dielectric breakdown (TDDB) is the common technique to evaluate reliability of gate oxides in MOS devices. In practice, two standard TDDB test methods of the constant voltage stress and constant current stress are usually applied. In the CVS test, a constant voltage stress is applied to the gate and the time needed to break the oxide is measured by detecting the abrupt change (rise) of resulting oxide current. Dually, in the CCS test, an electric current is injected through the oxide, which is maintained constant, and the time for the oxide to fail is measured.

Simulation of the TDDB is performed by modeling two main parameters: (1) the applied “stress” and (2) the “aging (time)” effect. Here, the stress is simulated by its effect on defect generation in the oxide. The formation of a conduction path in the oxide as a result of defect generation and accumulation by time is assumed to be the cause of breakdown. In so doing, the constant stress (either current or voltage stress) is modeled with a constant probability of defect generation (p_{dg}) in the oxide. The aging of the oxide, on the other hand, is modeled by generation and accumulation of defects in the oxide by time. This model can be called Constant Probability of Defect Generation (CPDG) which is a good simulation of CVS or CCS breakdown tests. The time-to-first-percolation is

considered as the time-to-breakdown.

4.4 Oxide Reliability Test

For a reliability test, 50 samples of the same size are subjected to a constant p_{dg} . In order not to damage the device at once, p_{dg} must be much smaller than critical probability (p_{crit})¹. The stress is periodically applied on each sample, and after each step of applying the stress, the availability of percolation path is tested. The time-to-breakdown is estimated by the time-to-first percolation. The defects are generated randomly, with a uniform distribution, in the oxide. The density of defects depends on the stress (p_{dg}) that is applied to the oxide. Because of the random generation of the defects, the same p_{dg} stress on the samples results in different distribution of defects. Therefore, although these defects have the same density, they cause different time-to-breakdown. This method of sample generation turns out to be able to closely simulate the degradation of dielectrics in a realistic manner.

To evaluate the reliability, a statistical failure analysis of 50 samples is accomplished. As an example, Figure 4.2 shows a histogram of the failure for a set of samples with the size of 40×40 cells. The choice of the statistical distribution function is one of the key issues for reliability projection of the oxide breakdown.

The obtained statistical data show that Weibull function is the best fit to the failure distribution of breakdown. Figure 4.3 represents the calculated cumulative failure density (CFD) for a set of 50 samples with dimensions of 40×40 . The Weibit function on the other

¹Note that the definition of p_{crit} (Equation 3.1) should be modified to model the percolation behavior in a finite lattice. Equation 3.1 is then revised to $p_{crit} = \sup\{p : \theta(p) < \epsilon\}$, where, $\epsilon > 0$ is a predetermined small parameter. p_{crit} is known as the normalized critical defect density in our research.

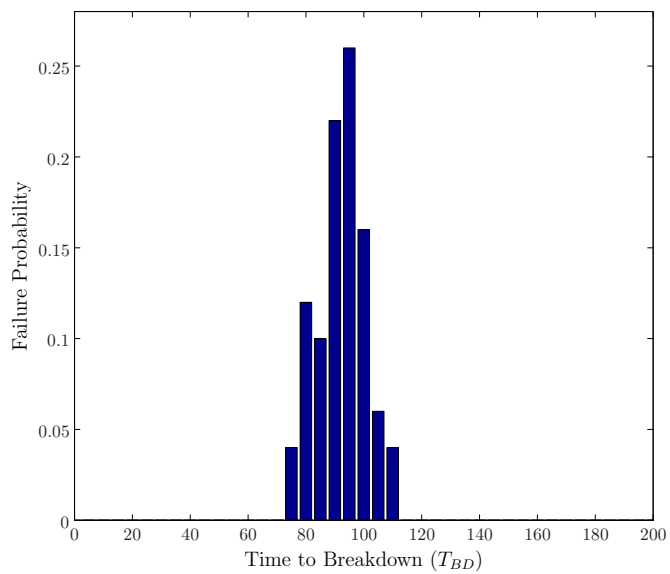


Figure 4.2: Histogram of the failure statistics for a set of 50 samples with the size of 40×40 cells

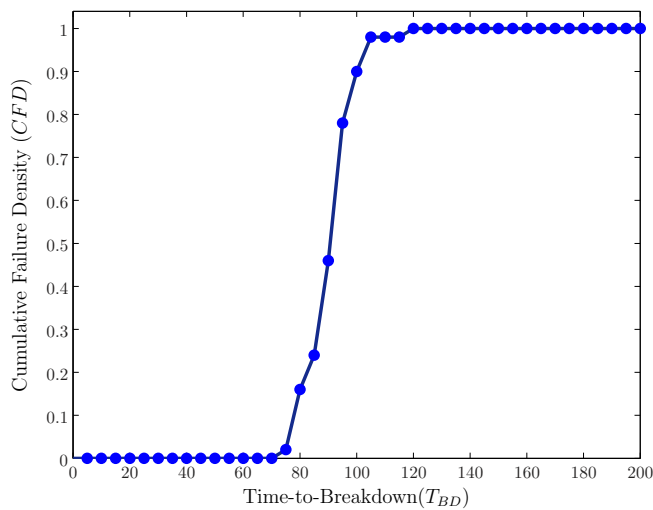


Figure 4.3: Cumulative failure density diagram for a set of 50 samples with the size of 40×40 cells

hand is shown on Figure 4.4. It is observed in Figure 4.4 that Weibit is a linear function of $\ln(T_{BD})$, which demonstrates that the breakdown has a Weibull characteristic.

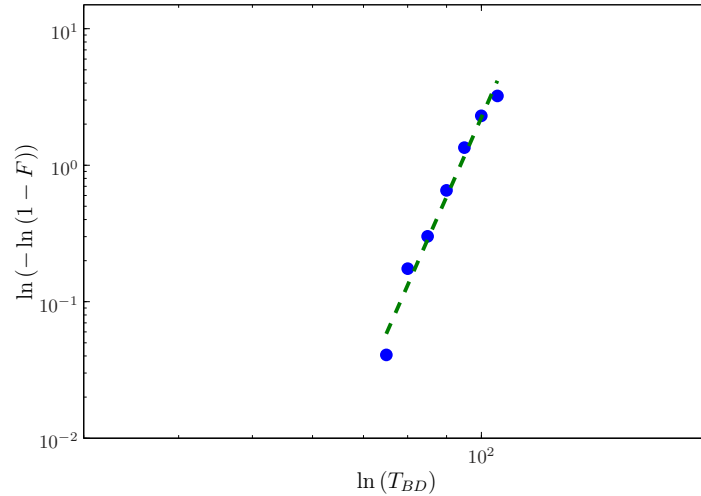


Figure 4.4: The obtained Weibit versus $\ln(T_{BD})$ for a set of 50 samples with the size of 40×40 cells. The linear curve substantiates the Weibull distribution of the failure.

4.5 Simulation of the Post-Breakdown Conduction in the Oxide

In addition to the reliability and the lifetime, the post-breakdown characteristic is also of interest and is measured to evaluate the oxide insulation after the breakdown. For thin film oxides, measurement of the post-breakdown current provides valuable information on how destructive the breakdown had been. Using the parallel-series conduction model that was discussed in section 3.5, percolation path conductance after the breakdown is calculated. Figure 4.5 draws the post-breakdown current for a 40×40 sample. As it is seen in the

figure, after the breakdown a sharp transition of the current occurs in the oxide. The sharp rise is mainly observed for thick oxides.

In the next chapter, the effects of applied stress and oxide dimensions on the shape of post-breakdown current curve will be inspected. It will be shown that since a very small critical defect density (almost zero) is needed to trigger the breakdown, soft breakdown is dominant for the ultra-thin oxides, and some plateaus occur in post-BD current in ultra-thin oxides.

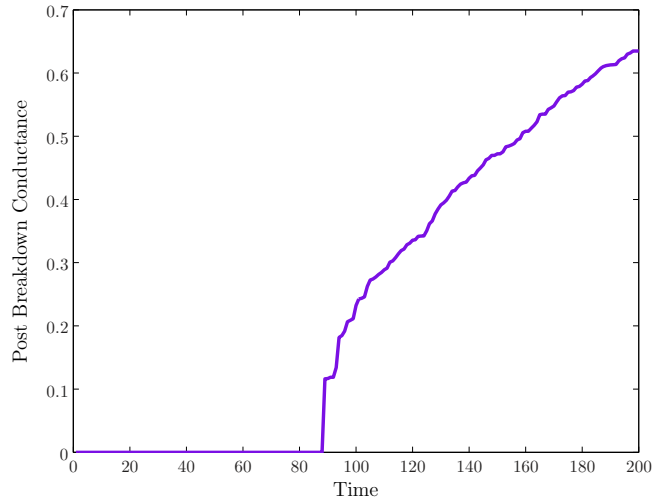


Figure 4.5: Post-breakdown current for a sample with the size of 40×40 cells

4.6 Summary and Conclusion

In this chapter, oxide breakdown was modeled using a 2-D percolation model. The time-to-breakdown was taken as being the time taken that the first-percolation path appears inside the oxide. Simulating the breakdown statistics for 50 samples, it was shown that oxide

reliability displays the Weibull characteristics. Furthermore, post-breakdown current was found using the parallel-series conduction model. A sharp transition of post-BD current was observed at the breakdown.

Chapter 5

Dimension and Stress Effects on Breakdown

Changes of oxide thickness and oxide area have significant effects on breakdown statistics, and also the post-breakdown current inside the oxide. As pointed out in chapter 2, one of the unanswered questions is, why does reducing the oxide thickness cause soft breakdown in shorter stress time and lower voltages? Moreover, due to the appearance of soft breakdown for ultra-thin oxides, finding an acceptable method for projection of oxide reliability based on accelerated voltage stressing in larger oxide areas is still currently a concern. It has been recognized that reducing the oxide area would result in lower percentage of soft-breakdown occurrences [152]. The causes of these phenomena are still unclear.

In this chapter, we study the effects of oxide dimensions and the applied stress on breakdown statistics and post-breakdown current using the CPDG model which was proposed in chapter 4. These issues will be elaborated on and justified via the introduction of a new concept of quasi-critical phase-transition in the following sections. The chapter

is organized as follows:

- (i) In section 5.1, the effects of oxide thickness on breakdown characteristics will be studied. It will be expounded how reduction of the oxide thickness to several atomic layers causes soft breakdown while hard breakdown occurs for thick oxides.
- (ii) The effects of changing the area on breakdown will be set forth in section 5.2.
- (iii) Section 5.3 will clarify stress effects on reliability test results. Knowing the effects of the applied stress on oxide reliability evaluation (TDDB test) is a new issue in CMOS technology. Especially, finding an extrapolation law to anticipate reliability for operating voltages from accelerated test conditions is of critical value.
- (iv) The chapter will be summarized and concluded in section 5.5.

5.1 Study of Thickness Effect on Oxide Breakdown

In this section, using the “CPDG method”, proposed in chapter 4, for the simulation of the TDDB, the oxide breakdown characteristic is studied for different oxide thicknesses. Using the “parallel-series-network model” (section 3.5) of the conduction path helps us to simulate the change of post-breakdown conduction with oxide thickness. Here, the breakdown simulation results for samples with 40, 20, 10, and 5 cells thickness, and the width of 200 are compared. A constant stress probability equal to 0.001 is applied to a set of 50 samples. The behavior of breakdown characteristics and post-BD conduction will be explained using the percolation theory.

Later, examining the effects of breakdown statistics for a wide range of oxide thicknesses, the variation of the Weibull slope and T_{BD} with oxide thickness will be elucidated, and the results will be compared with the experimental results reported in the literature.

5.1.1 Effects of Thickness on Time-to-Breakdown and Weibull Shape Factor

Figure 5.1 shows the cumulative failure density (CFD) for all four thicknesses. To find the CFD, 50 samples with the specified thickness are made and stressed under the same conditions, and the time-to-failure¹ is measured. As it is observed, decreasing the thickness shifts the CFD diagram to the left, which highlights the fact that for thinner oxides the oxide begins to fail earlier. Furthermore, it is observed that the CFD curves spread over a long time interval. This time-interval is longer for thinner oxides, resulting in smaller Weibull slope, and lower reliability as it will be seen later.

Table 5.1: The statistical results for samples with width = 200 cells and thickness = 5, 10, 20, and 40 cells

Thickness (cells)	Lifetime	Weibull Slope
5	347.69	4.75
10	554.52	7.37
20	702.95	15.21
40	823.30	18.03

¹The time-unit is arbitrary, and depends on the circumstances.

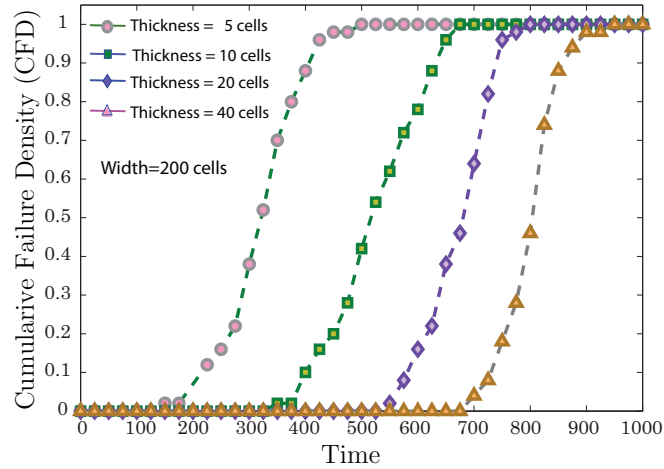


Figure 5.1: Comparison of the CFD diagrams for the samples with 40, 20, 10 and 5 cells thickness. The simulation is done over a set of samples with width = 200 cells, using the applied stress probability = 0.001.

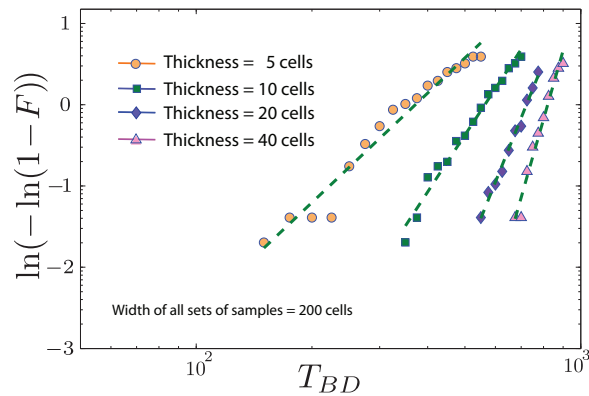


Figure 5.2: Weibull function for samples with 40, 20, 10 and 5 cells thickness. The simulation is done over a set of samples with width = 200 cells, using the applied stress probability = 0.001.

The CFD simulation shows that they fit the Weibull statistics very well. In Figure 5.2, fitting the CFD to the Weibull distribution, the Weibull function is plotted for all the samples. Scrutinizing the failure characteristics, it is found that the Weibull slope decreases from 11.3 for the thicker oxide ($t_{ox} = 40$) to 4.7 for $t_{ox} = 5$. The simulation results (lifetime² and Weibull slope) are summarized in Table 5.1.

5.1.2 Thickness Effect on Post-Breakdown Conduction

The post-breakdown current for the samples with 40, 20, 10, and 5 cells thickness are depicted in Figures 5.3, 5.4, 5.5 and 5.6, respectively.

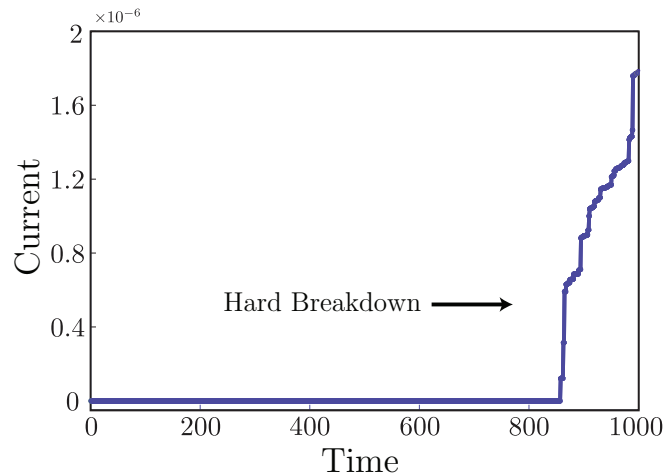


Figure 5.3: The post-breakdown current for a sample with 40 cells thickness

It is observed in Figure 5.3 that the current has a sudden rise from zero to higher values for the sample with 40 cells thickness, which represents the oxide breakdown. This sudden

²In the whole thesis, the terms “lifetime”, “ T_{BD} ” and “ T_{63} ” are used interchangeably and refer to the characteristic time-to-breakdown at 63.2 failure percentile.

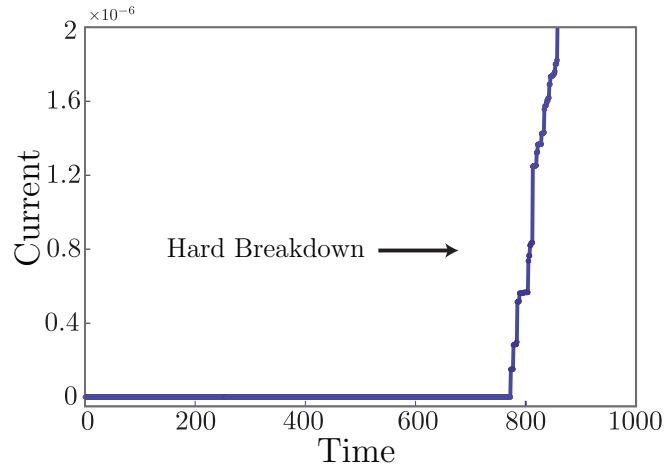


Figure 5.4: The post-breakdown current for a sample with 20 cells thickness

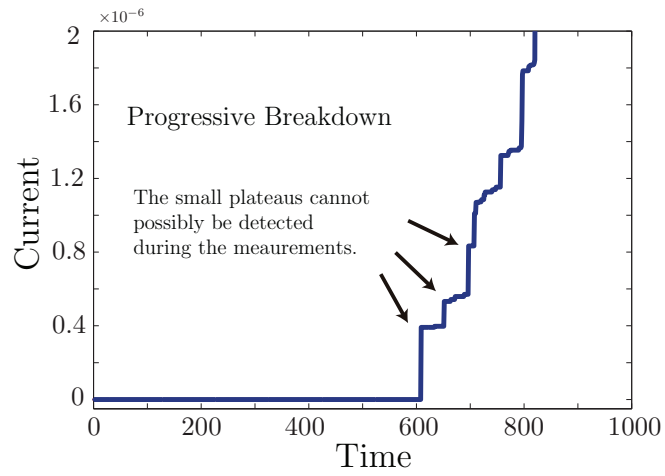


Figure 5.5: The post-breakdown current for a sample with 10 cells thickness

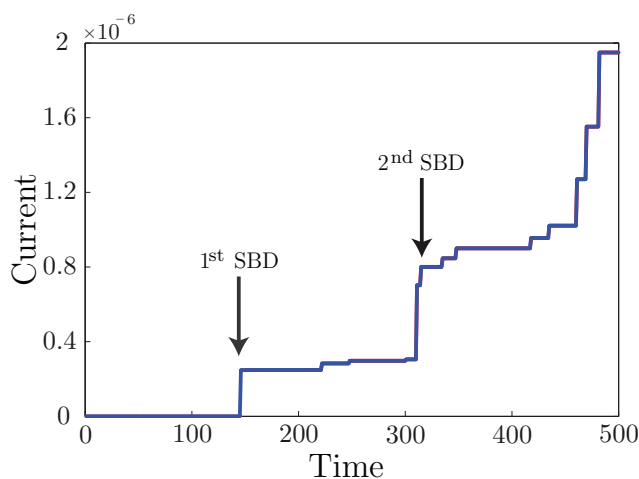


Figure 5.6: The post-breakdown current for a sample with 5 cells thickness

rise happens when the defect density in the oxide exceeds a critical density. When the oxide thickness decreases to 20 cells, there is still a sudden rise in the current (Figure 5.4). The lifetime of the oxide increases with thickness. For thicknesses less than about 10 cells, as seen in Figures 5.5 and 5.6, the jump in the current is not as sharp as the thicker oxides, and by time, some plateaus occur in the post breakdown current for very thin oxides.

Change of the post breakdown current from a sharp rise for thick oxides to a staircase shape for ultra-thin oxides has been observed experimentally [153]. These plateaus are recognized as soft breakdown in the literature. Figure 5.7 depicts the post breakdown current that Suñé et al. [153] published for the oxide breakdown with the thicknesses of 3-5 nm. Based on the Suñé's statement, none of the soft breakdown models, such as tunneling [154], hopping [120] and percolation, has explained the origin of these plateaus in post breakdown current.

In the next sub-section, it will be discussed how the origin of the difference between soft

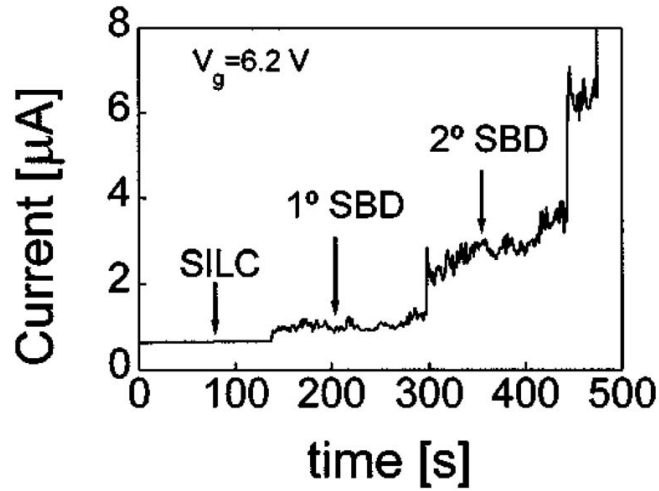


Figure 5.7: The experimental post-breakdown current for 3nm SiO₂ gate oxide [153]

and hard breakdown can be explained by the percolation theory. We will discuss about the critical nature of the dielectric breakdown, and how this phenomenon can be introduced as a phase transition. Then, it will be shown that for ultra-thin oxides the transition is not a critical phenomenon, and processes of defect buildup and oxide runaway are mixed. In this work, this type of transition will be termed as a “quasi-critical” phase transition.

5.1.3 Explaining the Results as the Quasi-Critical Nature of Soft Breakdown

It is observed from the simulation results (Figures 5.1-5.6) that reducing the oxide thickness results in three main phenomena: a) a decrease of the Weibull slope by decreasing the thickness, b) a decrease of the lifetime, and c) change of the post-breakdown current from a sudden rise for thick oxides to a multi-level function for oxides with very small thickness.

To clarify the origin of these differences, we study the nature of the percolation for thick

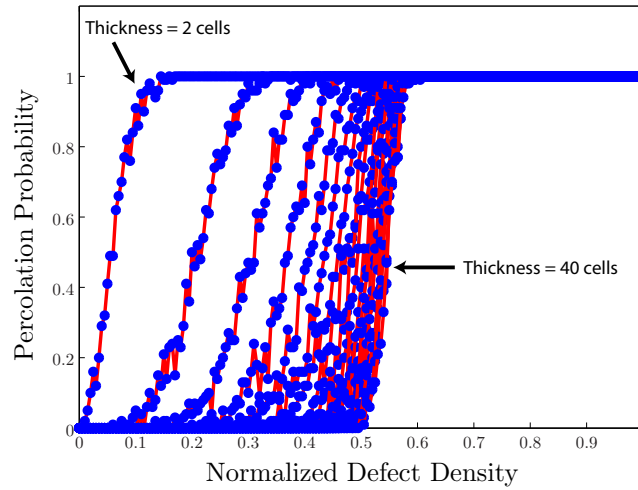


Figure 5.8: Percolation probability versus defect generation probability for samples with thickness changing from 2 cells to 40 cells. The width of all samples is 200 cells.

and thin oxides in this section. Using a Monte-Carlo technique, the percolation probability (P_{perc}) is calculated as a function of defect generation probability (p_{dg}) for different oxide thicknesses. Figure 5.8 shows the probability of percolation versus probability of defect generation for 20 samples with the width of 200 cells, and the thicknesses varying from 2 cell to 40 cells.³

Figure 5.8 suggests that, by decreasing the oxide thickness, the percolation curves shift toward the left. Generally speaking, for thick oxides (the curves at the right), the percolation curve has a shape (qualitative behavior) similar to Figure 5.9, while for ultra-thin oxides the curves follow Figure 5.10. The percolation probability curve in Figure 5.9 can be divided into three parts: (1) zero percolation probability for low density of defects

³Finding the exact analytical solution for the P_{perc} is a complicated and still open problem. Appendix A deals with this problem using recursive techniques resulting in some theorems.

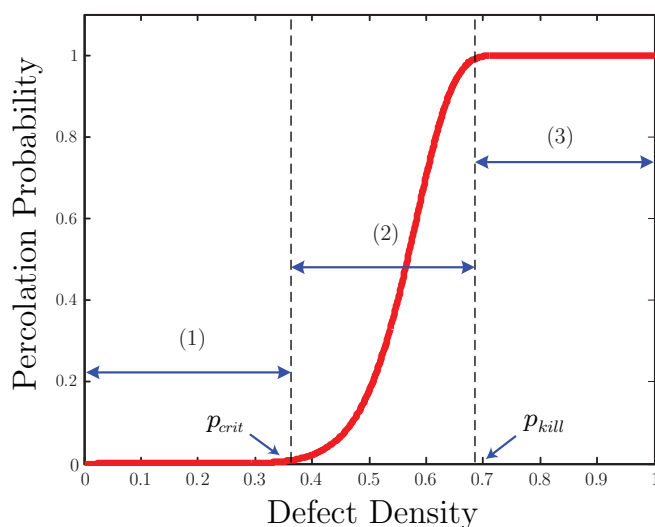


Figure 5.9: For thick oxides, the breakdown process can be explained in three stages: (1) a buildup stage, (2) a rapid runaway stage and (3) a post-breakdown stage.

in the oxide, before the defect density reaches a critical value (p_{crit}) (2) start of percolation, and a sudden rise to full percolation (percolation probability=1) after reaching the critical defect density, and (3) the full degradation.

As it is observed in Figure 5.8, decreasing the oxide thickness will reduce p_{crit} . For very thin oxides, i.e. for oxide thicknesses about a few layers of cells, p_{crit} is almost zero. The percolation characteristics for the very thin oxides (curves at the left) is similar to Figure 5.10. For these ultra-thin oxides, there is a chance of percolation even for low probability of defect generation, and the probability of percolation gradually increases to a full percolation.

Based on the above observations, the breakdown process for thick oxides can be explained in two stages: (1) a buildup stage where the oxide is slowly damaged under electrical stress, but no significant current passes through the oxide. This process continues until

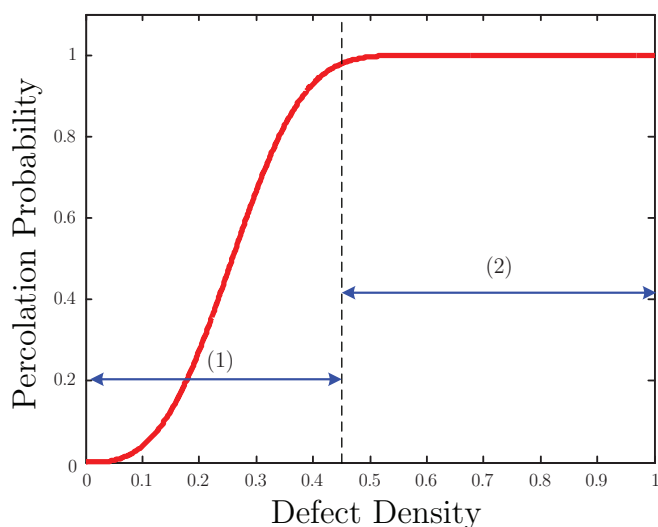


Figure 5.10: Quasi-critical characteristics of percolation for an oxide with a few layers of cells thickness

the defect density reaches a critical value. (2) the second stage is a rapid runaway, and full damaging of the oxide, in which the defect density in the oxide has exceeded the critical defect density and the oxide degrades very fast. Since at the critical defect density, a relatively large percentile of the thick oxide medium is damaged, the post breakdown current is very large, and we can observe a sharp rise in the current after the breakdown.

For ultra-thin oxides, however, the two stages of build-up and run-away are mixed. The percolation can happen at very small probability of defect generation, which causes a local current path in the oxide, and a small increase in the current is observed. The runaway here is not sharp and rapid but very gradual. The reason is that since the oxide is not extensively defected, after the critical defect density, a gradual increase in the defect density can create other new paths and bring about full destruction. In TDDB test, therefore, the current remains constant for a period of time until the next new path is created and,

thereby, the current is increased.

One of the main parameters that defines the breakdown process in thick oxides, is the critical defect generation probability (p_{crit}). As it can be seen in Figure 5.8, by decreasing the oxide thickness the critical defect generation probability decreases. Therefore, in the TDDB test, the time needed to accumulate defects in the oxide decreases as a result of decreasing the thickness. This fact can explain the reason of the lifetime reduction caused by decrease of the thickness.

The other important parameter is the killing defect generation probability (p_{kill}) which determines the defect density where the full percolation occurs. In contrast to p_{crit} , p_{kill} is defined as the probability after which p_{perc} becomes very close to 1:

$$p_{kill} \triangleq \inf\{p : 1 - \epsilon < \theta(p)\}, \quad (5.1)$$

where, $\epsilon > 0$ is a predetermined small parameter. The difference between p_{kill} and p_{crit} affects the speed of runaway, and also the slope of Weibull characteristics. As it is observed in Figure 5.8, by decreasing the thickness, $p_{kill} - p_{crit}$ increases. It follows that for smaller thicknesses the failure of the oxide happens in a large time interval, resulting in a smaller Weibull slope.

As can be expected, for ultra-thin oxides the critical defect generation probability does not have the same meaning as for the thick oxides. In the literature, the defect density needed to start the breakdown has been introduced as the critical defect density [47, 58, 92]. As Figure 5.8 represents, for the ultra-thin oxides this critical defect density is varying, and is not a constant value to be used for evaluating the reliability.

The above discussion suggests that the origins of soft and hard breakdown are different “Critical” and “Quasi-critical” characteristics of the breakdown phenomenon in the oxide.

By the “critical phenomenon” we mean that in thick oxides, a critical defect density is needed to trigger the breakdown after which a sharp runaway is registered. For ultra-thin oxides, however, we name the process of percolation as a “Quasi-critical phenomenon”, where the critical probability is almost zero. The breakdown can happen at different probabilities of defect generation depending on the distribution of defects in the oxide and the runaway is very gradual.

5.1.4 Breakdown Statistics

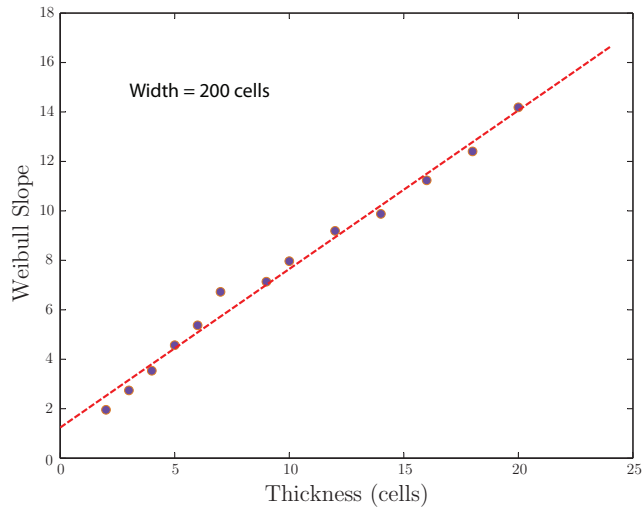
Studying the breakdown statistics is crucial for the real projection of the oxide reliability. Figure 5.11a shows the Weibull shape factor versus thickness for t_{ox} varying from 2 to 20 cells. The simulation results demonstrate that the Weibull slope linearly changes with oxide thickness ($\beta \propto t_{ox}$) matching the experimental data (Figure 5.11b) extracted from the literature [155].

Fitting a line to the resulted curve, we have:

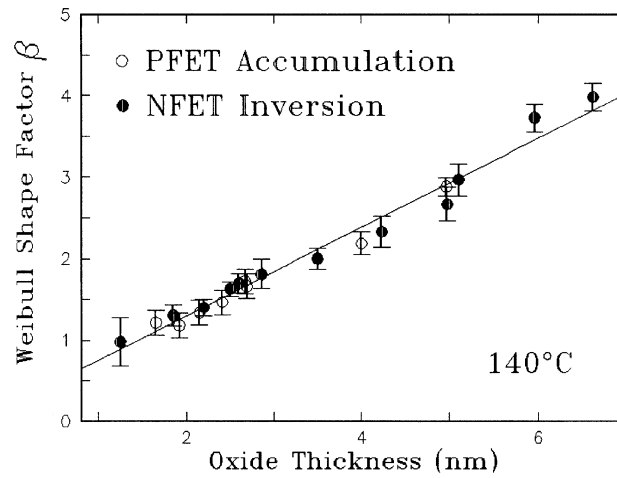
$$\beta \simeq 0.6413 \times t_{ox} + 1.2373$$

This result has been obtained for a width of 200 cells, and the stress $p_s = 0.001$ defects/unit time. As it will be discussed, however, the Weibull shape factor does not have a significant change with stress and width, which can be deployed to estimate the cell size in our simulations. In Appendix B, this issue will be elaborated on.

At the same time, it is found that the linear relation between β and thickness no longer holds for very thick oxides. Figure 5.12 shows the Weibull slope for the thickness changing from 2 to 100 cells.



(a)



(b)

Figure 5.11: (a) Weibull Slope versus thickness changing from 2 to 20 cells. The width of all samples is 200 cells. The simulation results show that the Weibull slope is a linear function of the thickness. (b) Measured Weibull slopes versus oxide thickness for p-channel FET (PFET) and n-channel FET (NFET). [155]

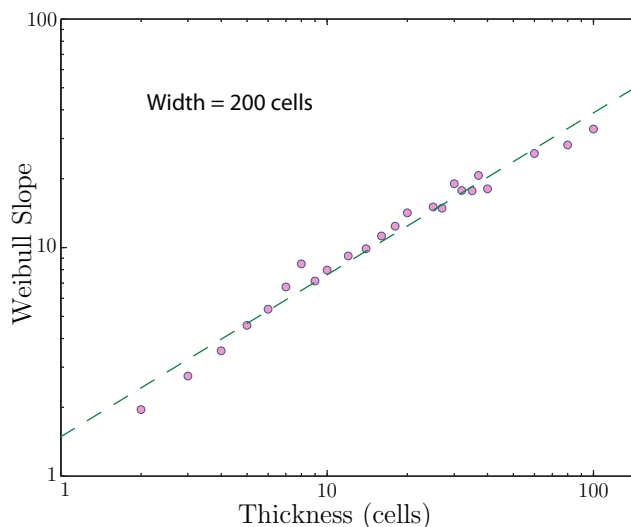
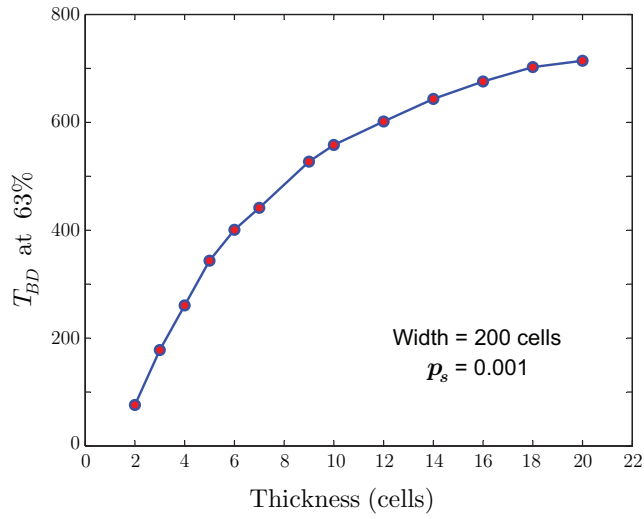


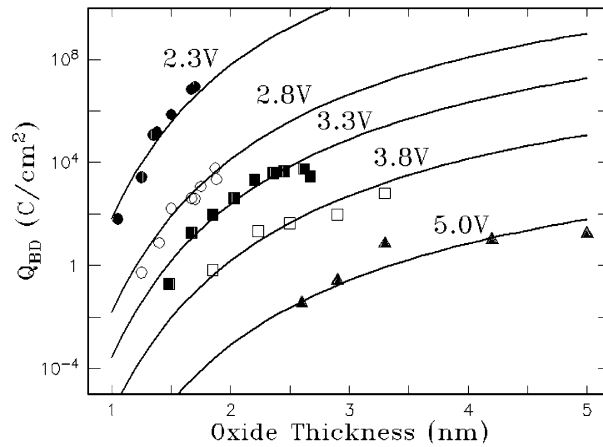
Figure 5.12: Weibull slope versus thickness in a log-log scale; For very thick oxides, the Weibull slope fits a power-law function better than a linear function of the oxide thickness

Plotting β versus thickness in a log-log scale results in a line which certifies that for very thick oxides, a power-law function, rather than a linear function, better describes the change of Weibull slope with thickness. Fitting the simulation results to a power-law function leads to $\beta \propto t_{ox}^a$, where $a \simeq 0.708$. The case of a very thick oxide, however, is not of much concern here, since the ultra-thin oxide reliability is the focus of research issue in this thesis.

Figure 5.13 plots time-to-breakdown versus t_{ox} . It is seen that T_{BD} increases by increasing the oxide thickness and the rate of increase is slower for thicker oxides. This behavior has been also reported by other researchers, and it can be seen in Figure 5.13b that the simulation result matches very well with the experiment [155]. For very thick oxides T_{BD} saturates, because the p_{crit} does not vary too much for thick oxides (see Figure 5.8).



(a)



(b)

Figure 5.13: Time-to-breakdown versus oxide thickness; (a) Simulation results; T_{63} is plotted versus thickness ranging from 2 to 40 cells. The width of all samples is 200 cells. (b) Experimental results [155]

5.2 Study of Width (Area) Effect on Breakdown Characteristics

In this section, the effects of oxide area on the breakdown statistics and post-breakdown conduction are addressed. The width of the network in the 2-D percolation model is a good representative of the oxide area in the 3-D real world. Using CPDG method introduced in chapter 4, the breakdown characteristics are studied for sets of samples with different widths. The simulation results show that reducing the width of the oxide increases the lifetime and hardens the breakdown, while not affecting the Weibull slope significantly. The simulation results very well match the experimental data presented in the literature. Using the percolation theory and the concepts of critical and quasi-critical phase-transitions, the results are explained and justified.

5.2.1 Width Effect on Time-to-Breakdown and Weibull Shape Factor

To study the breakdown statistics, 50 samples of the same width are stressed each time and T_{BD} and β are measured. Changing width of the samples, the effects of width on breakdown statistics are analyzed. Figure 5.14 shows the Weibit function for oxides with thickness = 5 cells, and the oxide-width varying from 5 to 200 cells. It is observed that the Weibit functions are parallel and therefore the Weibull slope does not change by width. The Weibit shifts to the left and it suggests that the T_{BD} decreases by increasing the width.

It is found that for widths less than 10 cells, the failure statistics does not very well match the Weibull function. This fact can be observed in Weibit plot for width = 5 cells in

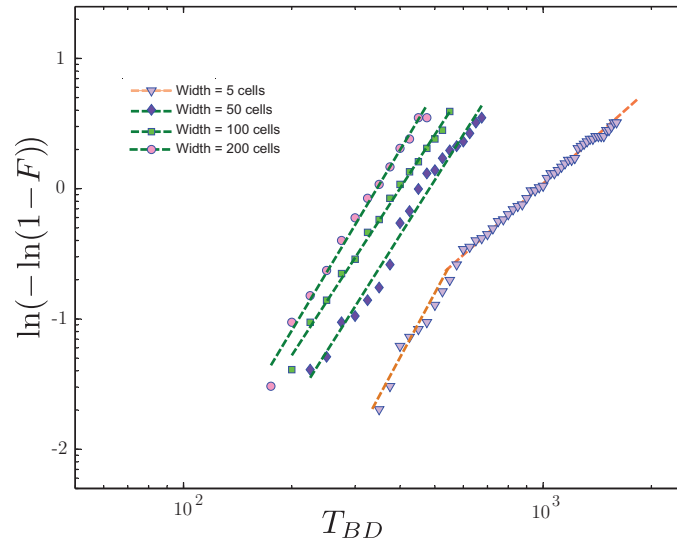
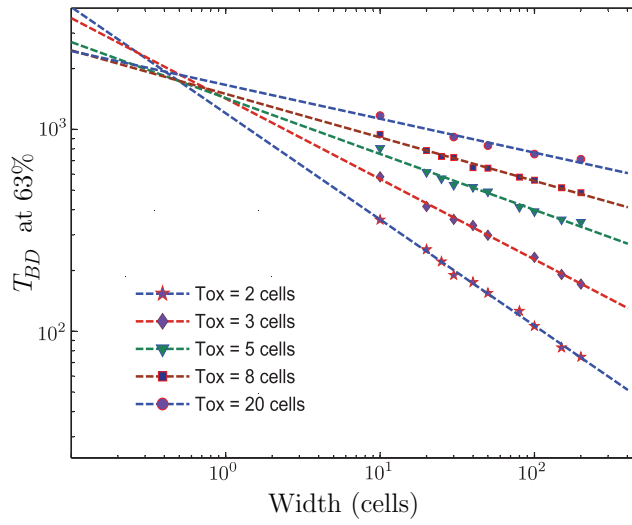


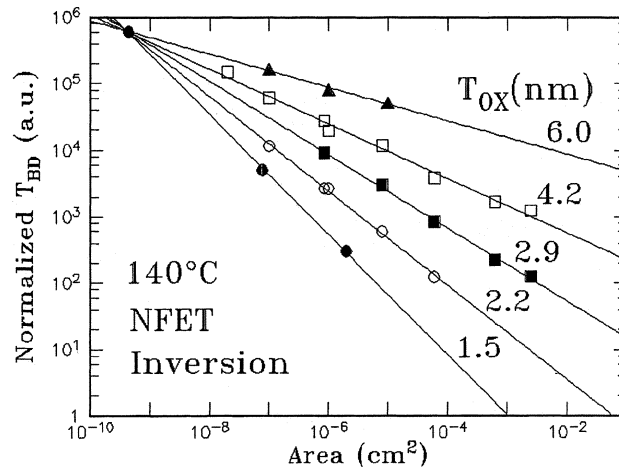
Figure 5.14: Weibit function versus time-to-breakdown for samples with width ranging from 5 to 200 cells; The results show that the Weibull shape factor (β) does not vary with width. The thickness of all the samples is equal to 5 cells.

Figure 5.14. As it will be explained in section 5.2.3, the spread of percolation probability over a wide range of defect density is the cause of such a fact. Figure 5.15a plots time-to-breakdown versus width of the oxide for different oxide thicknesses. The width varies from 5 to 5000 cells.

From the simulation results, T_{BD} turned out to be a power-law function of oxide width. $T_{BD} \propto (W_{ox})^a$ where W_{ox} is the oxide width and a is a function of oxide thickness. A similar power-law relationship has been reported by Wu et al. [155] from the experimental results (Figure 5.15b).



(a)



(b)

Figure 5.15: Area dependence of the normalized T_{BD} for several values of t_{ox} ; (a) Simulation results; (b) Measurement results extracted from [155]

5.2.2 Width Effect on Post-Breakdown Conduction

In the literature, the effect of oxide area on post-BD current has not been fully investigated. Indeed, the measurement limitations necessitate using larger-area devices and elevated-stress conditions [91]. With small-area samples, the measurements possibly take several years making the test impossible. Therefore, a procedure of using large-area devices to extract breakdown statistics and extrapolating the data to smaller-area conditions has been a common routine for evaluation of the oxide reliability [156].

In this research, the effect of the oxide width on the post-breakdown conductance has also been evaluated. As two examples, Figures 5.16 and 5.17 illustrate the post-BD conductance for samples with width = 200 and 20 cells, respectively. Figure 5.16 shows that a stair-case current curve is obtained for the sample with width equal to 200 cells, and these small plateaus are signs of soft-breakdown. The post-breakdown current in the sample with width = 20 cells (Figure 5.17), however, has a sharp rise, which represents the occurrence of hard-breakdown. The simulation has been conducted for a large number of samples and the same results have been obtained. These results confirm that reducing the oxide width results in the appearance of hard-breakdown even for the ultra-thin oxides. Similar experimental results have also been reported in the literature [152], showing that decreasing the oxide area results in hardening of the breakdown.

5.2.3 Width Effect on Percolation Probability Curves

As it was explained in section 5.1.3, the changes in breakdown characteristics are mainly due to the nature of percolation phenomenon. To study the effect of oxide width on the breakdown statistics, percolation probability versus defect generation probability is plotted

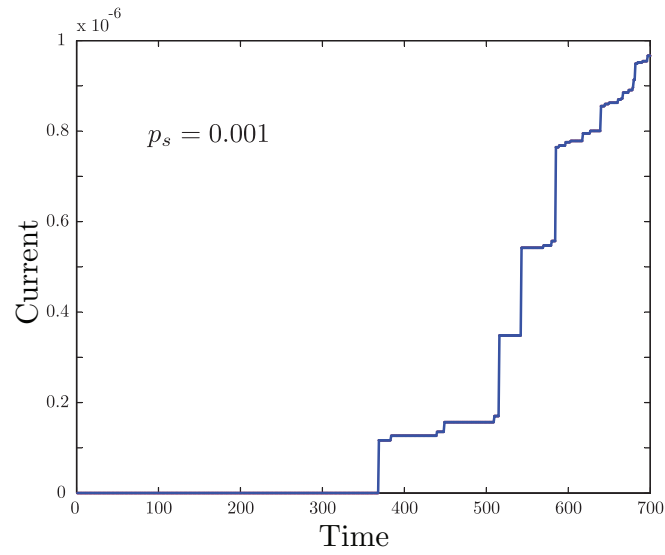


Figure 5.16: Post-breakdown current for a sample with width = 200 cells, and thickness = 10 cells; The $p_s = 0.001$ has been used to compute the post-breakdown conductance.

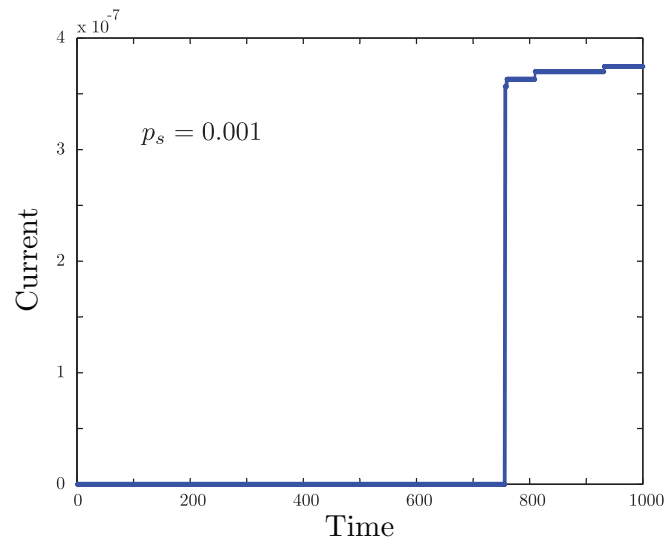


Figure 5.17: Post-breakdown current for a sample with width = 20 cells, and thickness = 10 cells; The $p_s = 0.001$ has been used to compute the post-breakdown conductance.

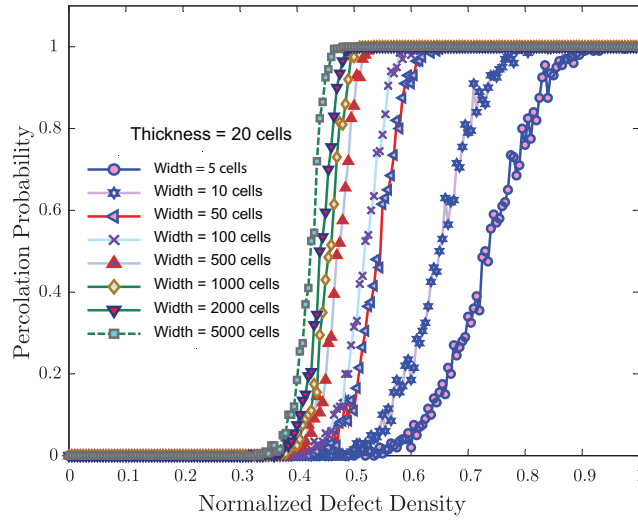
in Figure 5.18 for thick and ultra-thin oxides.

Figure 5.18a shows the percolation probability for thickness = 20 cells, and the width varying from 5 to 5000 cells. As it is observed in Figure 5.18, the percolation curves shift to the right by reducing the width. This verifies that the critical defect density increases by decreasing the width. This causes the increase of time-to-breakdown by reducing the oxide area as suggested by Figure 5.15. Figure 5.18a also represents that for a wide range of widths (from 50 to 5000), the slope of the percolation probability rise from zero (non-percolating) to one (full percolation) is almost the same, i.e. Weibull slope remains constant by changing the width.

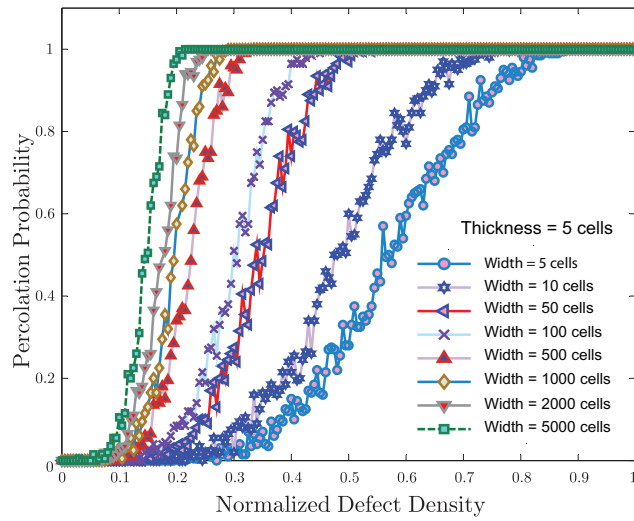
Figure 5.18b shows the percolation probability for oxide thickness = 5 cells, and the oxide width ranging from 5 to 5000 cells. It is observed that for ultra-thin oxides, the percolation probability has a very gradual rise to full-percolation when the width reduces to the order of 100 cells. The appearance of non-Weibull characteristics (see Figure 5.14) for some of the measurements is mainly the result of such a gradual rise.

5.3 Study of Stress Effect on Breakdown Behavior

In addition to the width and thickness, during the evaluation of the breakdown characteristics, the applied stress is another important factor which affects the breakdown characteristics, such as the probability of soft breakdown, the breakdown statistics, and the post-BD current. Since the reliability evaluation is usually done in accelerated stress conditions, studying the effects of stress is indispensable to project reliability. In this section, the effect of stress on breakdown is studied.



(a)



(b)

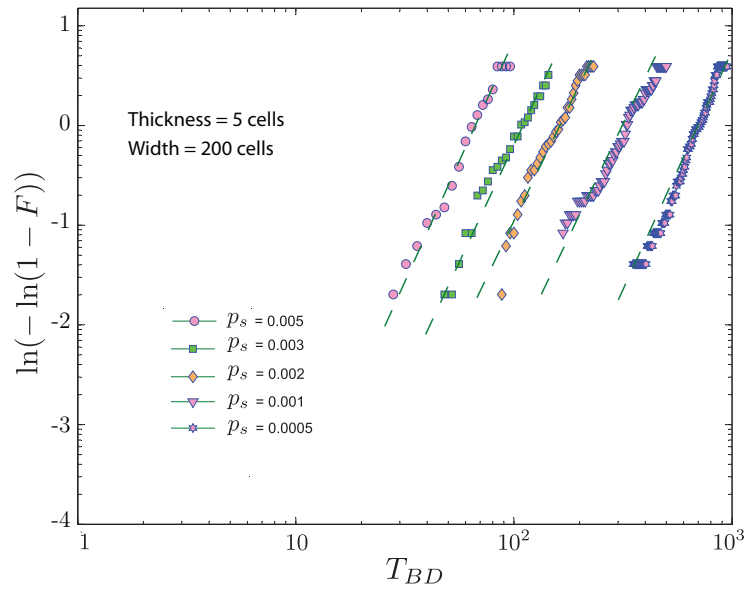
Figure 5.18: Percolation probability versus defect density for samples with different widths, ranging from 5 to 5000 cells; (a) All samples are 20 cells thick. (b) All samples are 5 cells thick.

5.3.1 Stress Effect on Time-to-Breakdown and Weibull Shape factor

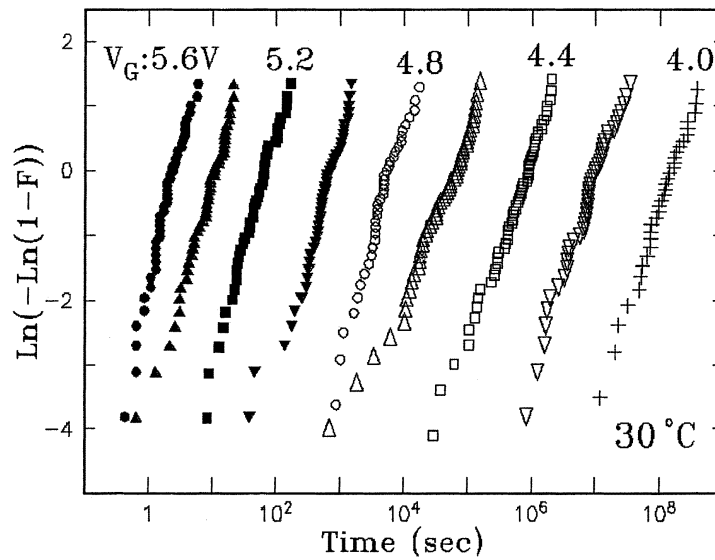
Figure 5.19a shows the Weibit function versus time-to-breakdown for a set of samples with thickness = 5 cells and width = 200 cells. The breakdown statistics is calculated using different applied stresses, $p_s = 0.0005, 0.001, 0.002, 0.003, 0.005$. The parallel Weibit lines suggest that the Weibull shape factor does not change with the applied stress (Figure 5.19a), which is also confirmed by the experimental data reported in the literature [155].

The Weibull slope is extracted for oxide thickness = 2, 3, 4, 5, and 10 cells. Figure 5.20a plots the Weibull slope versus the applied stress, for different oxide thicknesses. The simulation results show that the Weibull shape factor does not have a significant change with the applied stress, match very well the experimental results (Figure 5.20b) presented in the literature [155].

Time-to-breakdown versus applied stress is plotted in a log-log scale in Figure 5.21a. T_{BD} is plotted for different oxide thicknesses and the same width (width = 200 cells). As it is observed, $\ln(T_{BD})$ is a linear function of $\ln(p_s)$. These lines are parallel whose slope does not vary with oxide thickness. This means that T_{BD} is a power-law function of the stress and can be expressed as $T_{BD} \propto p_s^\alpha$ that α is the same for different oxide thicknesses. Similar experimental results are reported in the literature, measuring T_{BD} for different voltage stresses [157]. Figure 5.21b depicts the experimental results published by Wu et al. [158]. The simulation results and matching experimental data confirm that power-law voltage acceleration is acceptable to extrapolate reliability at operating conditions using accelerated test conditions.

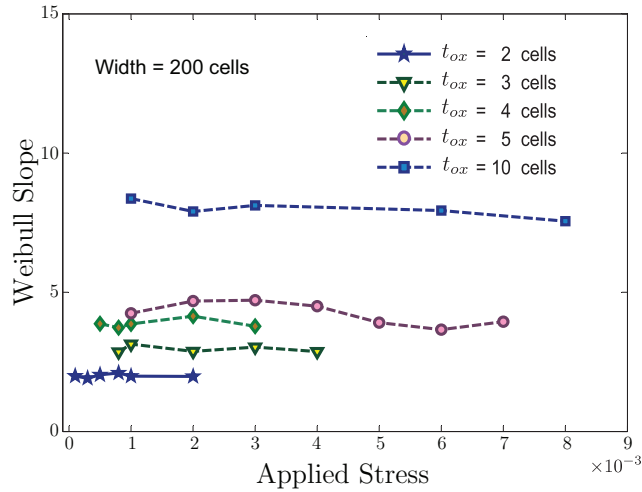


(a)

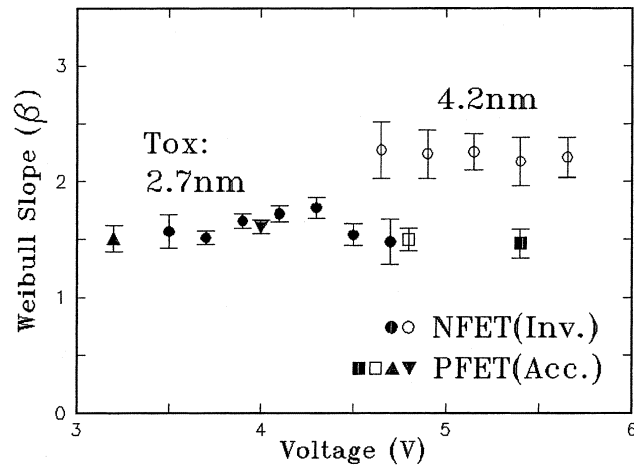


(b)

Figure 5.19: Weibit function versus time for different stress conditions; The Weibull slope does not change with the stress, matching the experiments. (a) Simulation results; (b) Experimental data reported in the literature [155]



(a)



(b)

Figure 5.20: (a) The Weibull shape factor versus the applied stress for samples with thickness = 2, 3, 4, 5 and 10 cells, and width = 200 cells; The Weibull slope does not change with the applied stress, matching the experimental results. (b) Experimental data reported in the literature [155]

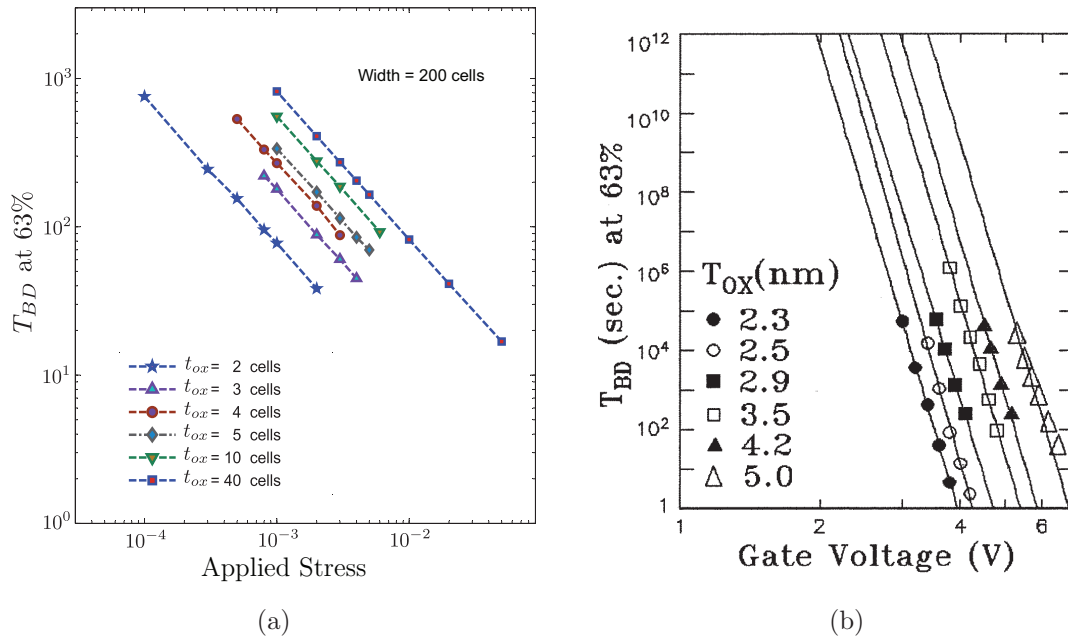


Figure 5.21: (a) Lifetime versus applied stress in a log-log scale for samples with thickness = 2, 3, 4, 5, 10, 40 cells; All samples have the same width = 200 cells. It is evident that the lifetime has a power-law relationship with the applied stress. (b) Log-log plot of lifetime versus gate voltage stress for samples with thickness varying from 2.3 to 5 nm; All the samples have the area = $6.2 \times 10^{-4} \text{ cm}^2$ [158].

5.3.2 Stress Effect on Post-Breakdown Conduction

I have found that decreasing the stress, and therefore decreasing the rate of defect generation, increases the chance of soft breakdown even for thick oxides. It means that by decreasing the stress, a large percentage of breakdown is soft, and the breakdown phenomenon is more gradual. This fact is due to the less abrupt transition of the percolation probability from zero to one, or the gradual change of the system status from non-percolating to percolating. Even for thick oxides, the transition from non-percolating to percolating phase is not perfectly sharp. In this way, thinner paths are created and plateaus are observed in post-BD current.

However, observing this behavior for thick oxides in the real world seems extremely difficult. The reason is that since the critical defect density is large for thick oxides, the time-to-breakdown is significant. It is, in fact, on the order of ten years using small applied voltage test stresses [91]. Consequently, a large stress is often needed to test the breakdown in a reasonable time interval. In this way, the gradual degradation is not often detectable in the test conditions and breakdown for thick oxides is reported to be purely hard.

5.4 Power-Law or Exponential Voltage-Dependence

A key element to accurately assess oxide reliability is the voltage-acceleration factor⁴ [159]. The exponential law for voltage dependence of T_{BD} has been historically used for reliability extrapolation. Recently, Wu and Suñé [157] reported that if the exponential extrapolation law is correct, then the voltage acceleration factor measured for thin oxides is larger than

⁴The voltage acceleration factor is defined as $\gamma = -\partial \ln(T_{BD})/\partial V_G$, which is extracted from the exponential extrapolation law $T_{BD} \sim \exp(-\gamma V_G)$.

that of thick oxides. Therefore, they have suggested that a power-law relationship (rather than exponential) holds between T_{BD} and V_G . In this section, it will be shown as to how the accumulation of defects by time causes the mentioned power-law behavior for ultra-thin oxides, while maintaining the exponential behavior of thick oxides.

5.4.1 Accumulation of Defects

The degradation of the oxide is the consequence of gradual accumulation of defects inside the oxide. The accumulation is done by time via stressing the sample with a stress $0 < p_s < 1$ at time steps $t = nt_0$. At each time step, every non-defected cell becomes defected with probability p_s . The following lemma expresses the defect density at n 'th step as a function of p_s :

Lemma 5.1 (Normalized Defect Density). *Let a sample be stressed with the stress p_s for time duration t . Then, for $n \geq 1$, the normalized defect density (i.e., the probability that a cell is trapped) at time $t = nt_0$ (where t_0 is the time unit) is*

$$P_n = 1 - (1 - p_s)^n. \quad (5.2)$$

Proof. The formula can be proved by induction on n . For $n = 1$, it is obvious that $P_1 = p_s$, and thus, the formula holds. Assume that for $n = k$ we have $P_k = 1 - (1 - p_s)^k$. One should then prove that $P_{k+1} = 1 - (1 - p_s)^{k+1}$.

To this end, note that the following recursive equation holds for every $n \geq 1$:

$$P_n = P_{n-1} + p_s(1 - P_{n-1}). \quad (5.3)$$

To see why this is true, denote by A_n , $n \geq 1$, the event that a cell is defected *at or before* $t = nt_0$. Recall that P_n is the probability of such an event. Also, notice that there are two

possibilities for a cell at n 'th time step, corresponding to whether or not it is defected at or before $n - 1$ 'th time step. These two event are, indeed, A_{n-1} and \bar{A}_{n-1} with probabilities P_{n-1} and $1 - P_{n-1}$, respectively. Expressing A_n conditional on A_{n-1} and \bar{A}_{n-1} , we can write:

$$P_n = \mathbb{P}\{A_n|A_{n-1}\}P_{n-1} + \mathbb{P}\{A_n|\bar{A}_{n-1}\}(1 - P_{n-1}). \quad (5.4)$$

Now, since $A_{n-1} \subset A_n$, we have $\mathbb{P}\{A_n|A_{n-1}\} = 1$. The event $A_n|\bar{A}_{n-1}$ indicates the event that the cell is defected exactly at the n 'th time step (not before). Thus, $\mathbb{P}\{A_n|\bar{A}_{n-1}\} = p_s$. (5.3) follows from (5.4) by substituting the probabilities with their mentioned values. Putting $n = k + 1$ in (5.3) and using the induction's assumption $P_{n-1} = P_k = 1 - (1 - p_s)^k$, the desired result will be established immediately.

The result of the lemma can be proved using a different and simpler approach: Consider \bar{A}_n as defined above. Now, observe that \bar{A}_n is the event that the cell has not been defected yet (until $t = nt_0$). This happens if and only if the cell is defected at *none* of the time steps $t = kt_0$, $k = 1, 2, \dots, n$. Since each of these events has probability $1 - p_s$ and they are independent, it follows that $\mathbb{P}\{\bar{A}_n\} = (1 - p_s)^n$, which completes the proof. \square

For the sake of simplicity, unless otherwise mentioned, the time unit $t_0 = 1$ is assumed throughout the rest of this chapter. Figure 5.22 plots P_t versus t .

At the breakdown, $P_{t=T_{BD}}$ is equal to p_{crit} . Therefore, considering p_{crit} to be constant for a specific thickness, we will have

$$1 - (1 - p_s)^{T_{BD}} = p_{crit} = const.$$

and T_{BD} can be found as a function of the applied stress p_s as follows:

$$T_{BD} = \frac{\ln(1 - p_{crit})}{\ln(1 - p_s)}. \quad (5.5)$$

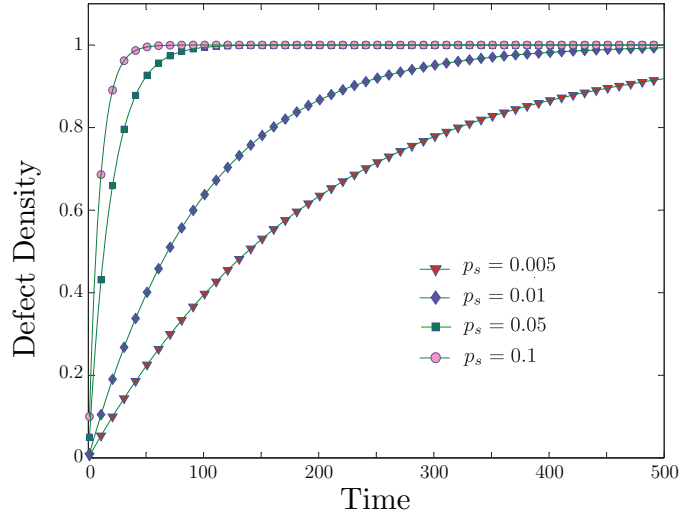


Figure 5.22: The density of accumulated defects inside the oxide versus time for different applied stress

If $\ln(-\ln(1 - p_{crit})) = K$, then $\ln(T_{BD}) = K - \ln(-\ln(1 - p_s))$. For small p_s , $\ln(1 - p_s) \simeq -p_s$, and therefore,

$$\ln(T_{BD}) = K - \ln(p_s). \quad (5.6)$$

Figure 5.23 shows T_{BD} versus p_s in a log-log scale based on Equation 5.5. As suggested by (5.6) and depicted in Figure 5.23, in small p_s regime, T_{BD} has a power-law relationship with p_s . The effect of critical defect density can be seen in Figure 5.24, where T_{BD} is plotted versus p_s , for different values of p_{crit} . We see from (5.5) that any change in the critical density corresponds to a constant shift in the lifetime (T_{BD}) and the slope does not change, resulting in parallel curves for the whole range of p_s in Figure 5.24.

To compare the behavior of T_{BD} in small and medium p_s regimes, we define two measurement windows corresponding to these two regimes. These measurement windows are

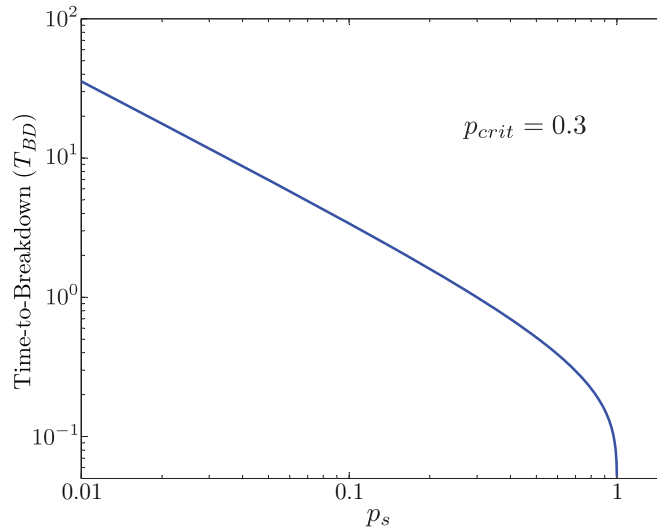


Figure 5.23: Time-to-breakdown versus the applied stress in a log-log scale, assuming the critical defect density = 0.3; The curve is plotted based on Equation 5.5.

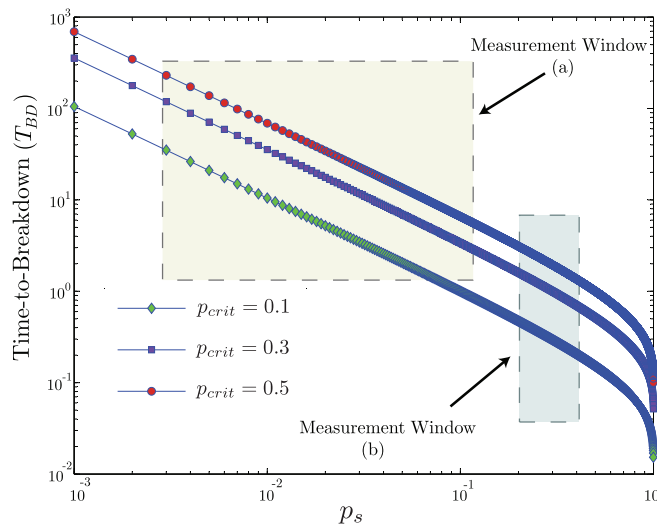


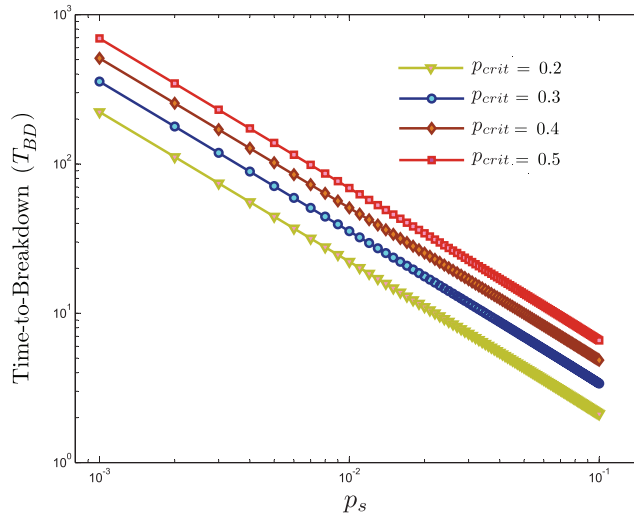
Figure 5.24: Time-to-breakdown versus the applied stress in a log-log scale, assuming the normalized critical defect density = 0.1, 0.3, 0.5; The curve is plotted based on Equation 5.5.

shown in Figure 5.24, labeled as windows (a) and (b). Large p_s is not of interest, since if p_s is larger than or comparable to p_{crit} , it will break down the oxide at once.

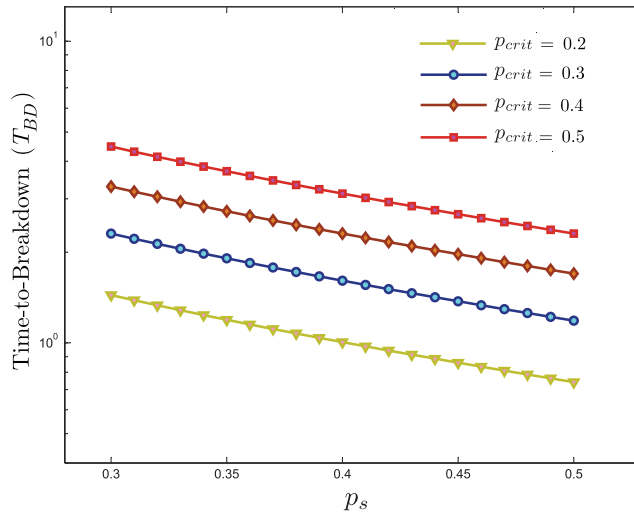
These two windows are magnified in Figure 5.25. In Figure 5.25a, which shows the measurement window (a), it is clear that the T_{BD} follows a power-law relationship with p_s . For medium p_s regime (i.e. window (b)), T_{BD} versus p_s is plotted in a *semi-log* scale. The semi-log lines in Figure 5.25b corroborate the fact that in the medium stress regime, T_{BD} varies exponentially with p_s .

5.5 Summary and Conclusion

In this chapter, the oxide breakdown characteristics under different measurement conditions were studied. It was shown that reducing the thickness results in appearance of soft breakdown, while hard breakdown occurs for thick oxides. The origin of soft and hard breakdown in gate oxides was studied using a percolation modeling approach. In this work, I have considered the breakdown as a phase-transition phenomenon. Examining the effects of thickness on the percolation threshold in samples, it was shown that breakdown behaves as a critical phenomenon, but by decreasing the oxide thickness, it turns to a quasi-critical phenomenon. It was shown that the quasi-critical nature of percolation in ultra-thin oxides causes the softening of the breakdown. Based on the results and the discussion, the breakdown in thick oxides is shown to be due to the buildup of defects to a critical density. This critical density in the thick oxides is significant which results in the damaging of a large part of the oxide, a large-area conduction path, and a significant increase in the current after the breakdown. For ultra-thin oxides, however, this critical density is negligible followed by the formation of small-area breakdown paths, and localization of the



(a) small stress regime, log-log plot



(b) medium stress regime, semilog plot

Figure 5.25: Time-to-breakdown versus the applied stress in a semi-log scale, assuming the critical defect density = 0.2, 0.3, 0.4, 0.5; The curve is plotted based on Equation 5.5.

breakdown spots. These small-area breakdown paths result in smaller increase of current which is called the softening of the breakdown. However, by time, the number of defects in the oxide increases which eventually leads to hard breakdown.

Chapter 6

Markov Chain Modeling of Breakdown

A Markov chain is mathematically identified as a discrete-time stochastic process with the Markov property [160]. Having the Markov property essentially means that the process has no memory and its value at any time depends only on its value at one time-step before. This memoryless property can model a variety of phenomena and systems and is employed to a wide range of applications such as statistical physics [161], biology [162], economics [163, 164] and music [165, 166]. The well studied Random Walk and Brownian Motion are important special cases of Markov processes that can model the movement of a particle in a liquid and a gas.

In this chapter, I model the electron transport inside a dielectric as a Markov process (Random Walk). Considering the effects of defect generation inside the dielectric by time, and based on a trapping-detrapping phenomenon, I will propose a model to describe the occurrence of electrical noise in both pre-BD and post-BD currents. Moreover, resistor-

network model used in section 3.6 is revisited and analyzed using Markov chains and, the post-BD current will be calculated. This chapter is organized as follows:

- (i) In section 6.1, a brief review of the Markov chain will be presented. Markov chain is defined and clarified through some examples. Two useful concepts, namely, “hitting time” and “absorption probability”, are defined and the latter is calculated using standard theorems.
- (ii) In section 6.2, oxide will be modeled as a network of cells. The electron transport in this network is modeled as a random walk through the oxide with non-trapped cells and trapped regions being the Markov states. The concept of hitting probability is deployed to analyze the behavior of current through the oxide with time. The “detrap” phenomenon is then incorporated into the model to introduce the current noise in the results. The proposed model proves to be fully consistent with the experimental results reported in the literature. The “ $1/f$ ” noise which is observed in the current can be justified by the proposed model as a result of trap accumulation process.
- (iii) A different approach to model the network as a Markov chain is considered in 6.4, which is a Markov analysis for the resistor-network model of section 3.6. Here, post-BD conductance will be calculated using the Markov transition matrix.

6.1 The Markov Chain Fundamentals

Consider a walker on the integer axis. If the walker is on the point i at the time instance n , it will step to either point $i - 1$ or point $i + 1$ with probabilities p and $1 - p$, respectively.

This process is the well known “Random Walk” on \mathbb{Z} . Figure 6.2 depicts such a process. Random walks on two or three-dimensional grids are defined similarly. It is observed that given the position of the walker at a time instance n , its position at time instance $n + 1$ is independent of its traversed positions before time n . In other words, the walker makes memoryless movements. A random walk is an example of a large class of stochastic processes, called *Markov Chains*. A standard definition of a Markov chain is as follows:

Definition 6.1 (Markov Chain [167]). $(X_n)_{n \geq 0}$ is a Markov chain with initial distribution λ and transition matrix \mathbf{P} (Markov(λ, \mathbf{P})) if

(i) X_0 has distribution λ

(ii) for $n \geq 0$, conditional on $X_n = i$, X_{n+1} has distribution $(p_{ij} : j \in S)$ and is independent of X_0, \dots, X_{n-1} . More explicitly, $\mathbb{P}(X_{n+1} = i_{n+1} | X_0 = i_0, \dots, X_n = i_n) = \mathbb{P}(X_{n+1} = i_{n+1} | X_n = i_n) = p_{i_n i_{n+1}}$.

S is called the *state-space* and each $i \in S$ is called a *state*. The above definition essentially points out that, given the state of the chain at a time, the future and past states are independent. Given the current state, the next state is determined by a distribution (which depends only on the current state). These conditional distributions are interpreted as transition probabilities between the states and construct rows of the transition matrix \mathbf{P} . This key feature enables us to describe a Markov chain with a state diagram whose nodes are the states and the state transitions are shown by arrows labelled with their corresponding transition probabilities. For example, Figure 6.1 shows the state diagram

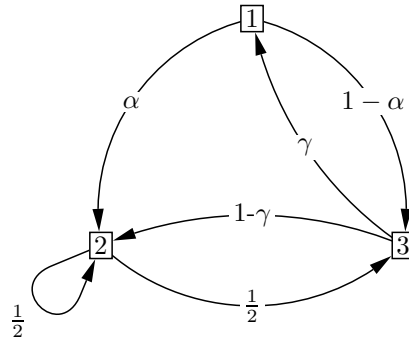


Figure 6.1: The state diagram corresponding to the transition matrix \mathbf{P}

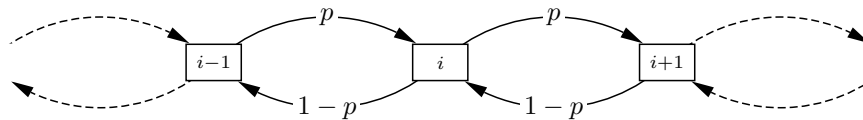


Figure 6.2: Simple random walk on \mathbb{Z}

for a three-state Markov chain with transition matrix

$$\mathbf{P} = \begin{pmatrix} 0 & \alpha & 1 - \alpha \\ 0 & 1/2 & 1/2 \\ \gamma & 1 - \gamma & 0 \end{pmatrix}.$$

Note that since rows of a transition matrix are distributions, their elements add to 1.

The state-space can be either finite or infinite. Figures 6.1 and 6.2 exemplify finite-state and infinite-state Markov chains, respectively.

The most important characteristic of Markov chains known as *Markov property* is that they have no memory. This fact is mathematically expressed through the following theorem:

Theorem 6.1 (Markov property [167]). *Let $(X_n)_{n \geq 0}$ be Markov(λ, \mathbf{P}). Then, conditional on $X_m = i$, $(X_{m+n})_{n \geq 0}$ is Markov($\delta^{(i)}, \mathbf{P}$) and is independent of the random variables X_0, \dots, X_{m-1} where $\delta^{(i)}$ is defined on S as follows:*

$$\delta_j^{(i)} = \begin{cases} 1 & \text{for } j = i \\ 0 & \text{for } j \neq i \end{cases}$$

In the rest of this section, I invoke some characteristics of Markov chains needed in our electron analysis in the following sections.

6.1.1 Hitting Times and Absorption Probabilities

Let $(X_n)_{n \geq 0}$ be a Markov chain with transition matrix \mathbf{P} . The *hitting time* of a subset A of S is the random variable $H^A \in \{0, 1, 2, \dots\}$ given by

$$H^A = \min\{n \geq 0 : X_n \in A\} \quad (6.1)$$

where the minimum of the empty set is defined to be ∞ . In other words, H^A is a random variable with the following distribution:

$$\mathbb{P}(H^A = m) = \mathbb{P}\left(\bigcap_{n=0}^{m-1} \{X_n \notin A\} \cap \{X_m \in A\}\right). \quad (6.2)$$

The *hitting probability* is the probability that $(X_n)_{n \geq 0}$ starting from state i ever hits A and is defined by:

$$h_i^A = \mathbb{P}(H^A < \infty | X_0 = i). \quad (6.3)$$

When there is no escape from A , h_i^A is called the *absorption probability*, and A is called an absorbing state. The following theorem from [167] is fundamental for calculation of hitting probabilities in a Markov chain:

Theorem 6.2 (Hitting probabilities [167]). *The vector of hitting probabilities $\underline{h}^A = (h_i^A : i \in S)$ is the minimal non-negative solution to the system of linear equations*

$$\begin{cases} h_i^A = 1 & \text{for } i \in A \\ h_i^A = \sum_{j \in S} p_{ij} h_j^A & \text{for } i \notin A. \end{cases} \quad (6.4)$$

Minimality means that if $x = (x_i : i \in S)$ is another solution with $x_i \geq 0$ for all i , then $x_i \geq h_i$ for all i .

For an elaborate discussion on Markov chains the reader is referred to [167]. In the following section, the concept of *harmonic functions* is defined and their application in Markov chains is highlighted which will be used in the subsequent sections.

6.1.2 Harmonic function

A harmonic function is basically defined for lattice points in a two dimensional plane [168, 169]. Lattice points are points with integer coordinates on the plane. In the lattice context, a harmonic function is defined as follows:

Definition 6.2 (harmonic function [168, 169]). *Let $S = D \cup B$ be a set of lattice points where (a) $D \cap B = \emptyset$, (b) every point in D has its four **neighboring** points in S and (c) every point in B has at least one of its four neighboring points in D . Points in D are called **interior** points while points in B are called **boundary** points.*

Then a function f defined on S is harmonic if, for points $(a, b) \in D$, it has the averaging property

$$f(a, b) = \frac{f(a+1, b) + f(a-1, b) + f(a, b+1) + f(a, b-1)}{4} \quad (6.5)$$

The values of f is explicitly given on the boundary points. The problem of finding a harmonic function over a set of points given specific boundary values is called *Dirichlet* problem.

There are two main principles regarding harmonic functions [168, 169]:

Maximum Principle : A harmonic function takes its maximum (and also minimum) values on the boundary points.

Uniqueness Principle : If f and g are two harmonic functions such that $f(x) = g(x)$ on the boundary points, then they are equal over all points in S .

The definition of a harmonic function can be generalized to Markov chains. In the Markov chain context, the points are states. Similarly, $S = D \cup B$ is the state-space where B and D are two subset of states satisfying only the condition (a). A state $j \in S$ is said to be a neighboring state of state $i \in S$ if there is a transition $i \rightarrow j$ with nonzero probability in the Markov chain. Therefore, the equation 6.5 turns to the following equation:

$$\forall i \in D : f(i) = \sum_{j \in S} p_{ij} f(j) = \sum_{j \in S_i} p_{ij} f(j) \quad (6.6)$$

where S_i is set of all neighboring states of i . Note that since $\sum_{j \in S_i} p_{ij} = 1$ for all $i \in S$ and $p_{ij} \geq 0$ for all $i, j \in S$, equation 6.6 is a weighted averaging over the neighboring states of state i . The Maximum and Uniqueness principles also hold in the Markov context since they are based on the averaging property of the harmonic function. As an important example, Theorem 6.2 shows that the hitting probability of the states in a Markov chain is a harmonic function. Later, in section 6.4, we will use this fact to find the equivalent conductance of a degraded oxide by considering different conduction through defected and non-defected cells of the oxide equivalent lattice.

6.2 Electron Transport Inside the Oxide

To model electron transport as a Markov process, we can consider the oxide as a network of molecular cells through which electron passes. Figure 6.3 illustrates the schematic of this modeling. In the probabilistic modeling of electron transport inside the oxide I use here, the electron in a non-trapped cell travels to the neighboring cells with probabilities p (vertically) and q (horizontally). I also incorporate a probability r into the model, such that $p + 2q + r = 1$, which represents the transition to a dummy state. This dummy transition accounts for the fact that a non-trapped cell is actually an isolating one which must have a tendency to hinder the electron transport. Transition to the dummy state is, therefore, interpreted as a termination to the electron transport. Here, I call p and q , respectively, *inter-layer* and *intra-layer* transition probabilities.

Since position of the electron after a transition given its current position is independent of its previously visited positions (cells), this probabilistic model complies with the definition of Markov chain (Definition 6.1). All non-trapped cells and also trapped *regions* correspond to a Markov state.

6.2.1 Non-Trapped Network

Considering the traps to be the effect of applying the stress, a virgin oxide can be modeled as a non-trapped network of cells. In a non-trapped network, every cell is simply a Markov state. Figure 6.3 shows the Markov chain schematic of a network of size $M \times N$. The dummy transitions are not shown in the figure. Note that since the transitions initiating from a state in Markov chain have probabilities adding to 1, it is assumed that the electron transits with probability $2q$ from an edge cell to its horizontal neighbor. The initial state

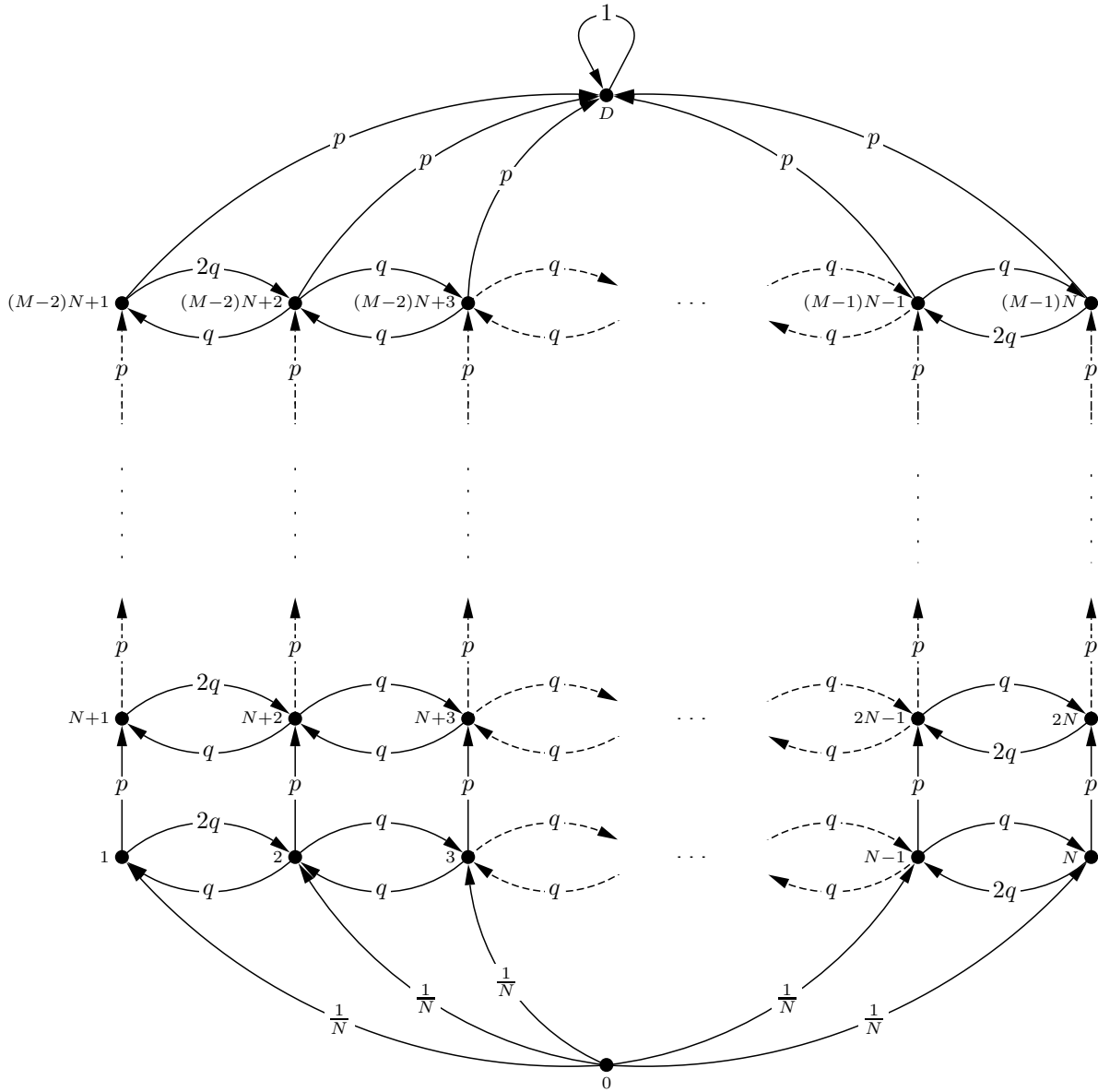


Figure 6.3: Markov chain model for the oxide

or

$$h^D(m) = \frac{p}{1-2q} h^D(m-1).$$

This together with the the initial condition $h^D(1) = 1$ result in $h^D(m) = (\frac{p}{1-2q})^{m-1}$. Now, using the Uniqueness principle [168, 169] for harmonic functions, one can deduce that this is the only solution to the system of equations 6.4. This last observation completes the proof. \square

6.2.2 Trapped Network

The Markov chain of a trapped network is constructed from that of its non-trapped counterpart by merging the cells of every trapped region to single states called *trapped states* which have no outgoing transition. The incoming transitions to a trapped state contain all the incoming transitions that are towards the cells comprising the corresponding region. Figures 6.4 and 6.5 show a trapped network and its corresponding Markov chain (before and after merging the trapped cells), respectively.

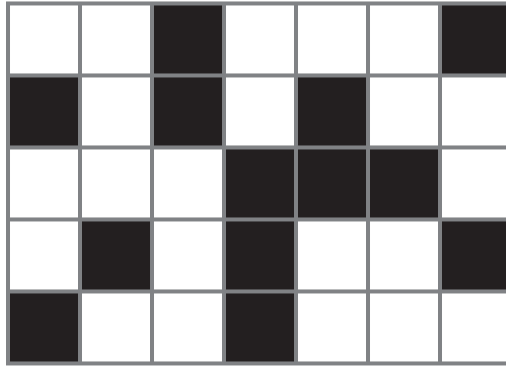
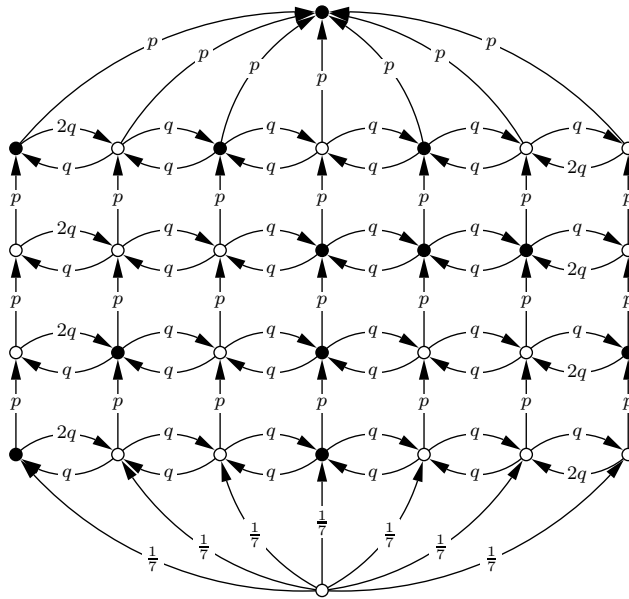
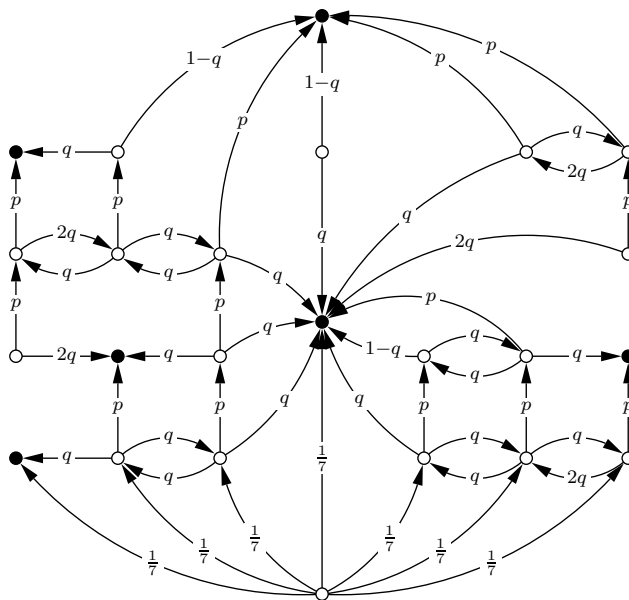


Figure 6.4: A sample 5×7 trapped network



(a) The corresponding Markov chain (before merging the trapped cells)



(b) The final Markov chain

Figure 6.5: The Markov chain corresponding to the trapped network of Figure 6.4

To study the behavior of current inside the oxide using Markov chains, the absorption probability is considered as a representative of the current. This is because the current inside the oxide is proportional to the absorption probability of electrons to the cathode. In this model, it is indeed assumed that a fixed number of electrons enters the oxide through the anode. The absorption (hitting) probability then represents the percentage of these electrons that arrive at the cathode, which is a reasonable measure of current.

In the trapped network, we have two different types of absorbing states: (a) traps, (b) the anode. Traps are absorbing because there exists no detrap probability.

It is usually more convenient if we reorder the states so that the absorbing states come first and the non-absorbing states come last in the transition matrix. Then, the transition matrix would have the *canonical* form [168]:

$$\mathbf{P} = \begin{pmatrix} \mathbf{I} & \mathbf{0} \\ \mathbf{R} & \mathbf{Q} \end{pmatrix}.$$

If u and v are the number of absorbing and non-absorbing states in the Markov chain, respectively, then \mathbf{I} is a u -by- u identity matrix and $\mathbf{0}$ is a u -by- v all-zero matrix. Using the canonical form and Theorem 6.2, it can be shown that the hitting probabilities can be obtained using the following equation [168]:

$$\mathbf{H} = (\mathbf{I} - \mathbf{Q})^{-1}\mathbf{R} \tag{6.7}$$

where $\mathbf{H} = (h_{ij})_{v \times u}$ is the desired hitting probability matrix with h_{ij} being the absorption probability to state j starting from state i .

Figure 6.6 shows the simulated absorption probability for a 5×40 network. In this simulation, the network is trapped accumulatively with trap density 0.001. The inter-layer and intra-layer transition probabilities are set to be $p = 0.3$ and $q = 0.05$. Equation 6.7 is

then used to calculate the absorption probability from the initial state (the cathode) to the final state (the anode). As observed in the figure, the proposed Markov model well describes the breakdown phenomena in the oxide through the plateaus in the absorption probability curve in a characteristic way. In section 6.3, we will see how trap-detrap phenomenon results in a significant noise in post-BD current. This noise is known as a significant sign of breakdown.

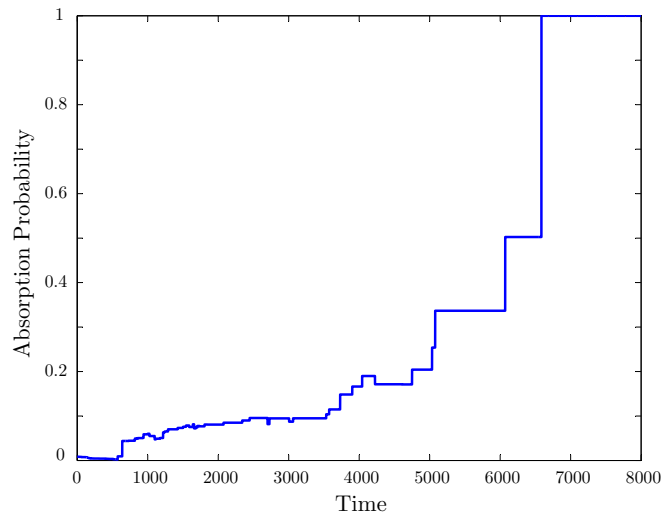


Figure 6.6: Absorption probability versus time for a 5×40 accumulatively trapped network

6.3 Trap-Detrap

For ultra-thin oxides, there is a large possibility of de-trapping of electrons. To study the effects of detrapping of electrons, during the accumulation of the traps inside the oxide, we add a possibility of detrapping to the network. It can be assumed that after a detrap, electron escapes from the trap state. Therefore, the detrap can be modeled as random

uniform reduction of the trap density inside the network. More specifically, after each trapping step in the accumulative model, the cells (trapped cells) are detrapped using a “detrapping density” which is typically less than the applied trap density. The absorption probability is again exploited as a measure of the oxide current.

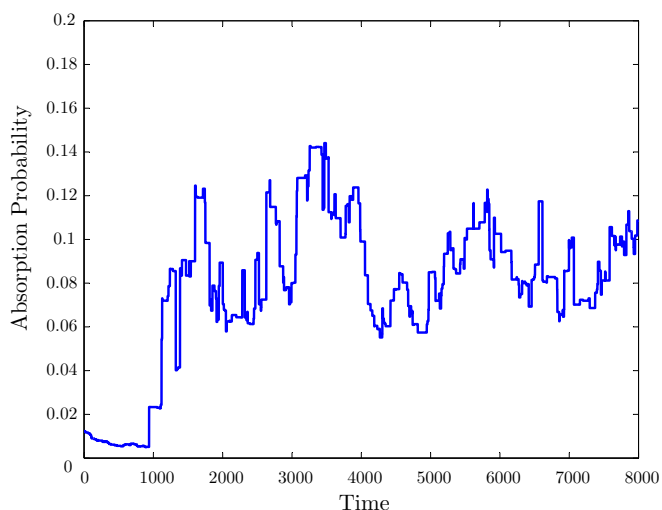


Figure 6.7: Absorption probability versus time for a 5×40 accumulatively trapped-detrapped network

It is observed that both before- and after-breakdown currents are noisy due to the de-trappings. The interesting and useful result is that the noise power increases compared to the pre-breakdown noise component, although both noises have the same characteristics that has already been observed in experiments [170]. The observation of this fact justifies the credibility of relying on an increase in gate noise as a precise indication of soft breakdown.

Figure 6.7 sketches the hitting probability of electrons versus time. By time, defects are accumulated inside the oxide, and electrons get trapped inside them during the trans-

port. The de-trap also occurs after each step of trapping. It is observed that the hitting probability jumps to a higher value, with a noisy component. This plateau is the result of creation of a path inside the oxide while the observed noise originates mainly from the variation of trap density resulted from the alternate trapping and detrapping process.

In order to characterize the noise behavior, the Power Spectral Density (PSD) of noise is considered. Two different methods are used to estimate the PSD of noise (see [171] for a detailed description of these methods):

Periodogram This method is essentially a nonparametric FFT-based estimation method in which the PSD is estimated directly from the noise itself. Figure 6.8 shows the PSD of noise before and after breakdown using Periodogram.

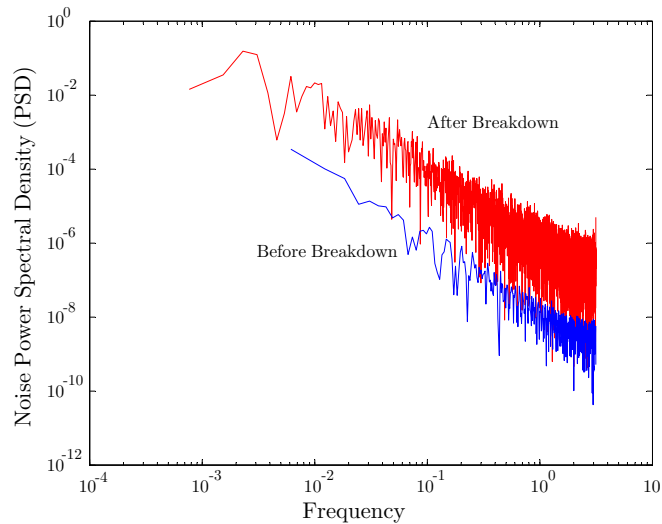


Figure 6.8: The PSD of noise using Periodogram method

Burg This method, which usually gives smoother results than the Periodogram, is a parametric one in which the PSD is estimated from a signal that is assumed to be the

output of a linear system driven by white noise. This method estimates the PSD by first estimating the parameters (coefficients) of the linear system that hypothetically generates the signal. Results of this estimation method are shown in Figure 6.9. This method has the advantage to help us compare and characterize the noises.

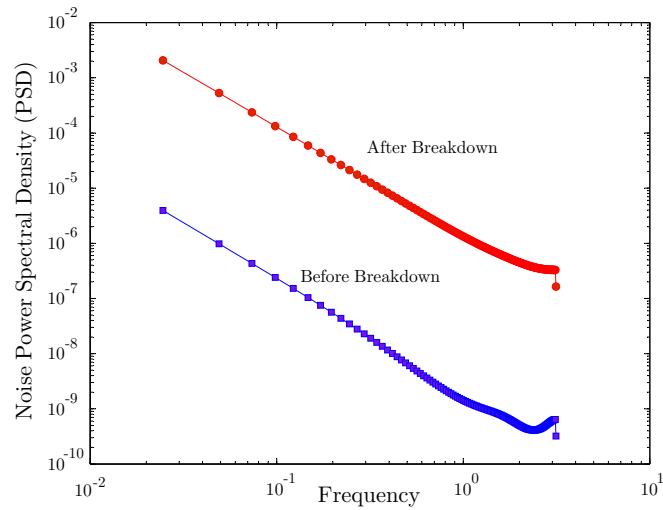


Figure 6.9: The PSD of noise using Burg method

The simulation results show that the noise power after the BD is about $10^4 - 10^5$ larger than before breakdown, while the noise characteristics do not change. To understand the increase in noise power after breakdown, notice that before breakdown, there exists no trapped path between the anode and the cathode. Therefore, in this regime the main origin of the noise is fluctuation in density of *isolated* trapped regions due to the alternate trapping and detrapping process. Since the absorption probability is not significant, any change in density of these isolated trapped regions does not affect the the absorption probability significantly.

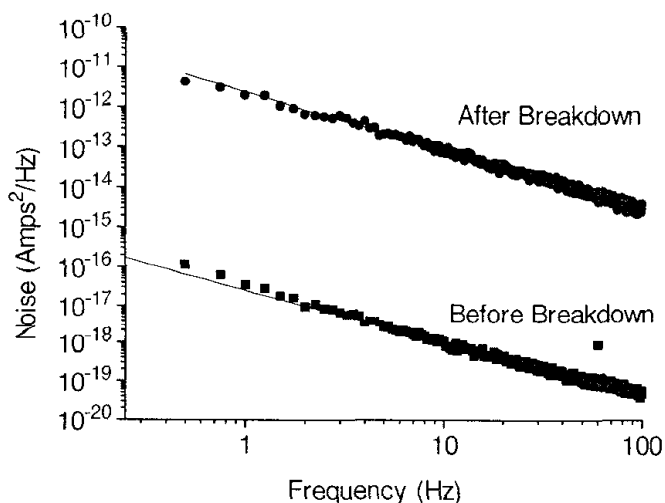


Figure 6.10: The PSD of experimental current noise [170]

After breakdown, however, at least one conducting path of traps has been formed between the anode and the cathode. Since the breakdown is soft, the absorption probability is not very large (it is around 0.2 in Figure 6.7) and the isolated regions absorb the electrons with a probability comparable to this absorption probability. Therefore, in this regime, the noise is again due to fluctuations in density of the isolated trapped regions which result in a noise with fluctuations comparable to the absorption probability itself. Thus, the noise power is significantly increased after breakdown.

Interestingly, the noises, however, turn out to have the same distributions before and after breakdown and are $1/f^\alpha$ ($\alpha \cong 2$) noises (according to Figures 6.8 and 6.9). It is well known that $1/f^2$ noise characterizes a *Brown* noise. On the other hand, the accumulative nature of the trapping and detrapping process (which is the source of the noise) here has indeed a Brownian nature. In the accumulative process, the distribution of trapped cells throughout the oxide at each step is ascertained by randomly adding/removing some traps

to/from the existing trap distribution.

The simulation results very well match the experimental data reported in the literature [112, 170]. Cester et al. [112] have found that the current noise power density can be generally described by a $1/f^\alpha$ -law (with α between 1 and 2) over the frequency range from 1 Hz to 100 kHz. As an other example, Figure 6.10 illustrates the PSD of experimental current noise before and after breakdown as obtained in [170]. The authors have found that the current noise after the soft breakdown has a $1/f$ characteristics and the noise power increases by over 4 orders of magnitude in a 2nm oxide. It can be seen that the proposed model well characterizes the current noise reported in the literature.

6.4 Markov Model of Trapped Configuration as a Resistor Network

Analyzing a trapped network to be equivalent to a resistor network, similar to section 3.6, I have simulated the post-breakdown conductance. Here a resistor network is modeled and analyzed using Markov chain model. Probabilistic interpretations are given as in [168, 169] for voltage and current analyses. The resistor network model for a trapped network is then analyzed using this Markov chain technique.

6.4.1 Resistor Network Equivalent Markov Chain

In order to model a resistor network with Markov chain, the states and transition probabilities should be determined. The circuit nodes are obviously taken as the Markov states. We further assume that all nodes in D are connected to each other or nodes in B with

only resistors (*cf.* Definition 6.2). For transition probabilities, let us take a look at the equations between node voltages in the circuit (node equations):

$$\sum_{j \in S_i} G_{ij}(v_i - v_j) = 0, \quad \forall i \in D \quad (6.8)$$

which can be rewritten as follows:

$$v_i = \sum_{j \in S_i} \frac{G_{ij}}{G_i} v_j, \quad \forall i \in D \quad (6.9)$$

where $G_i = \sum_{j \in S_i} G_{ij}$ and $G_{ij} = 1/R_{ij}$ is the conductance of branch ij . Now, if we define p_{ij} for all $i, j \in S$ to be equal to G_{ij}/G_i , then $\{p_{ij}\}$ is clearly a probability mass function for a fixed i . More specifically, we have $0 \leq p_{ij} \leq 1$ for all $i, j \in S$ and $\sum_{j \in S_i} p_{ij} = 1$ for all $i \in S$.

Therefore, (6.9) is equivalent to

$$v_i = \sum_{j \in S_i} p_{ij} v_j, \quad \forall i \in D \quad (6.10)$$

which shows that voltage of the nodes is a harmonic function. If we now set the nodes in B to have some specific voltages, then according to the Uniqueness principle, a unique set of voltages satisfies (6.10).

6.4.2 Voltage Interpretation

There is an interesting interpretation for voltages of the nodes when B consists of only two nodes a and b , having voltages 1 and 0, respectively. Note that the outgoing transition probabilities of nodes in B do not appear in the equations of a harmonic function, and hence, do not affect the solution. Therefore we can assume that all nodes in B are

absorbing. Thus, we have

$$\begin{aligned} v_a &= h_a^a = 1 \\ v_b &= h_b^a = 0 \end{aligned} \tag{6.11}$$

where h_i^j is absorption probability of state i to state j .

In this case, it is easy to see that voltages of the nodes satisfy the same equations as the absorption (hitting) probabilities of the nodes to node a . Then, according to the Uniqueness principle [168, 169], voltages of the nodes are their absorption probabilities to node a .

6.4.3 Current Interpretation

In order to give a probabilistic interpretation for current, note that in reality, the positive charge enters the network at node a and wanders around from node to node until it arrives at node b . In this its journey throughout the network, an electron may transition several times from node i to j or in the opposite direction. Therefore, one expects that the net current from i to j is equal to expected value of the difference between number of $i \rightarrow j$ and $j \rightarrow i$ transitions. This is in fact true and is established in the following argument.

As noted in [168], let u_i be the expected number that a positive charge starting from a visits state i before arriving at b . Note that if the walker returns to a before reaching b it keeps walking. Therefore, unlike the voltage analysis, the outgoing transitions from state a are considered in the Markov chain. Then, $u_b = 0$ and

$$u_i = \sum_{j \in S} p_{ji} u_j, \quad \forall i \neq a, b \tag{6.12}$$

since every transition to i has to be done through one of the other states in S .

Writing transition probabilities of (6.12) in terms of branch conductances, we have

$$\begin{aligned} u_i &= \sum_{j \in S} \frac{G_{ij}}{G_j} u_j \\ &= \sum_{j \in S_i} p_{ij} u_j \frac{G_i}{G_j} \end{aligned} \quad (6.13)$$

Defining $\hat{v}_i = u_i/G_i$ for all $i \in S$, we have $\hat{v}_i = \sum_{j \in S_i} p_{ij} \hat{v}_j$ which suggests that \hat{v} is a harmonic function with $\hat{v}_a = u_a/G_a$ and $\hat{v}_b = 0$. \hat{v} is in fact voltage of the nodes when the input voltage $\hat{v}_a = u_a/G_a$ is applied to the network at the point a .

Now, if the current $I_{i \rightarrow j}$ is written in terms of voltages of nodes i and j in this network, we have

$$I_{i \rightarrow j} = (\hat{v}_i - \hat{v}_j)G_{ij} = \left(\frac{u_i}{G_i} - \frac{u_j}{G_j}\right)G_{ij} = u_i p_{ij} - u_j p_{ji}. \quad (6.14)$$

Notice that, $u_i p_{ij}$ is the expected number of times that the walker (positive charge) transitions from i to j . This establishes the first guess for current analysis.

It should be observed that the above argument gives a probabilistic approach for calculating electrical currents in branches of a network with input voltage u_a/G_a . This quantity is no longer a constant (as to the case with a constant 1-volt input to the network for the voltage analysis). Now if we consider the total current flowing into the network from node a , we observe that

$$\sum_{i \in S_a} I_{a \rightarrow i} = 1. \quad (6.15)$$

The last equation is true because, except the first time the walker enters the network at node a , each time it enters node a it has to leave that node. Therefore, the expected value of difference of the number of times the walker enters and leaves node a will be 1. Thus, in the current interpretation, a unit current is assumed to enter the network.

6.4.4 Simulation Results

Simulating the disordered nature of defected oxide as a resistor network, similar to what was proposed in section 3.6, the conductance was calculated. Setting $\frac{R_2}{R_1} = 1000$, the conductance has been calculated and is plotted in Figure 6.11. R_2 and R_1 are the resistance of non-conducting and conducting bonds in the resistor network, respectively, and define the transition probabilities in transition matrix of the Markov chain as described in sections 6.4.2 and 6.4.3.

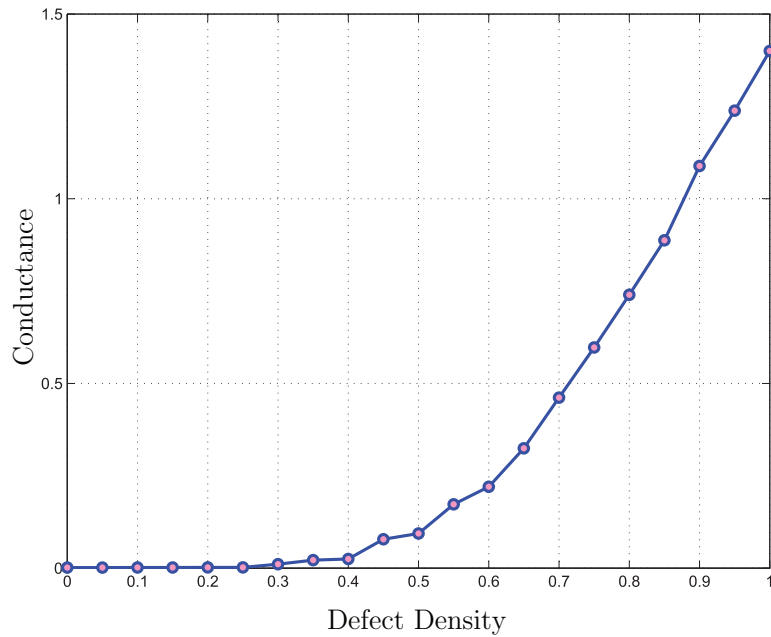


Figure 6.11: Conductance for a resistor network with thickness = 5 cells, and width = 7 cells

6.5 Summary and Conclusion

In this chapter, the electron transport inside the oxide was modeled as a Markov chain process. The trap sites were considered as absorbing states, which confine the electron transport through the oxide. These absorbing states, however, conduct current when a path is created. The effect of detrapping of electrons on the oxide current was simulated and the resulting noise became characterized.

In a different approach, the conductance of the defected material as a resistor network was calculated using Markov chain. In this method, the voltage can be interpreted as the hitting probability if a unit voltage is applied to the sample. The current in each branch was interpreted as the expected number of net transitions from site to site.

Chapter 7

Tunneling Model of SILC

The increase of gate current in a MOS device following a high field is referred to as Stress-Induced Leakage Current (SILC). SILC in ultrathin SiO₂ films is one of the most crucial reliability concerns for realizing dependable future ULSIs. The SILC increases with decreasing oxide thickness and has been identified as a scaling limitation for nonvolatile memory tunnel oxide. Therefore, the physical understanding of carrier transport mechanism of SILC is quite important in realizing highly reliable SiO₂ films. Although several models for the transport mechanism have been proposed, the physical origin and the definitive model to describe it has not been established yet.

In this chapter, I study the quasi-critical nature of the phase transition in ultra-thin oxides can result in the SILC at low electric fields. The concept of quantum percolation with tunneling will be introduced to model and study the observed results.

This chapter is organized as follows:

- (i) In section 7.1, the physical models that are reported in the literature to explain the SILC origin will be reviewed.

- (ii) In section 7.2, the concept of “quantum percolation” will be introduced. It will be discussed how the finite tunneling barrier between trap sites will result in smaller percolation threshold, and results in the SILC before SBD occurs.
- (iii) In section 7.3, it will be shown how the SILC can be modeled as two parallel F-N tunneling currents which pass through a high and low-bandgap materials. We will explain how the quasi-critical nature of the phase-transition in ultra-thin oxides results in the creation of several very thin conducting paths that with the continuation of applying the stress will change to stronger defected damage and irreversible oxide breakdown.
- (iv) In section 7.4, the experimental results will fit to F-N tunneling, and the simulation results will be presented. It will be shown that the experimental data obtained under different stress conditions match the simulation results.

7.1 SILC Physical Models

SILC is defined as a low field gate leakage current following high-field stressing of thin oxide MOS capacitors (Figure 7.1), which was discovered in the 1980’s for the first time [172–174]. Such a leakage current occurs during write and erase operations of electrically erasable programmable read only memory devices. SILC has also been demonstrated to be the factor that limits the scaling of tunnel oxides, because the loss of stored charge from the floating gate of nonvolatile memory devices degrades data retention times [174, 175]. Therefore, SILC in ultra-thin SiO₂ films is one of the most crucial reliability concerns for realizing dependable future ULSIs [174–178].

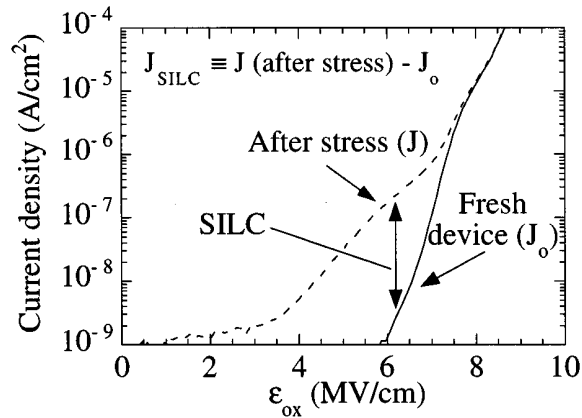


Figure 7.1: The current density versus the oxide electric field (E_{ox}) before (the solid line) and after (the dashed line) applying the stress [175]; The stress induced leakage current is defined as the difference between the current going through the virgin oxide (J_0) and the after-stress current (J): $J_{SILC} = J - J_0$.

In recent years, there has been a significant effort to understand the physics of the leakage current. In general, the models proposed to explain the leakage mechanism in SiO_2 films can mainly be categorized into four main groups. Figure 7.2 shows the principles of these models in a band diagram. These models include charge-assisted tunneling [179,180], conduction due to local thinning of the gate oxide [101,181], elastic trap-assisted tunneling [182–185], inelastic single-trap-assisted tunneling and inelastic multi-trap assisted tunneling [176].

The charge-assisted tunneling model was first proposed by Maserjian and Zamani [172]. In this model, it is assumed that, following the electron injection due to stress, positive charges are generated near the Si/ SiO_2 interface which cause the observed excess current behavior. The other model which was proposed by Olivo et al. [173,179] explains the SILC

origin by generation of localized weak spots near the injecting interface and thinning of the oxide. Other researchers modeled the SILC as a trap-assisted tunneling (TAT) via the neutral trap sites inside the oxide [183–192]. In this model, it is believed that the neutral trap sites are generated during the high field stress, and capture and emission of electrons in these trap sites cause the SILC. Yasuda et al. modeled a two-step elastic tunneling process [183], considering different time constants for the capture and emission of electrons.

It has been observed experimentally that the SILC carriers lose roughly 1.5 eV in the SiO₂ layer [176]. There are two possible explanations for this phenomenon. It is proposed that a possible explanation of this energy loss would be that SILC is due to elastic valance-band tunneling rather than conduction band electrons tunneling. However, this hypothesis has been rejected based on carrier-separation experiments [176]. A second explanation is that SILC is due to inelastic tunneling process rather than elastic TAT [176, 178]. According to this model, resonant tunneling occurs from trap-to-trap, and energy relaxation happens by emitting multiple phonons within the trap. Currently, inelastic TAT is the mostly accepted model to describe the SILC phenomenon as it is better consistent with the experimental observations [192].

7.2 Quantum Percolation with Tunneling

In the classical percolation theory, electrons are considered as particle-like classical objects. In the real world, however, due to the quantum interference effect, the electron has a wave-nature. The quantum percolation theory is based on this effect [145]. Assuming electrons as quantum particles is the basis of quantum percolation theory. Quantum percolation

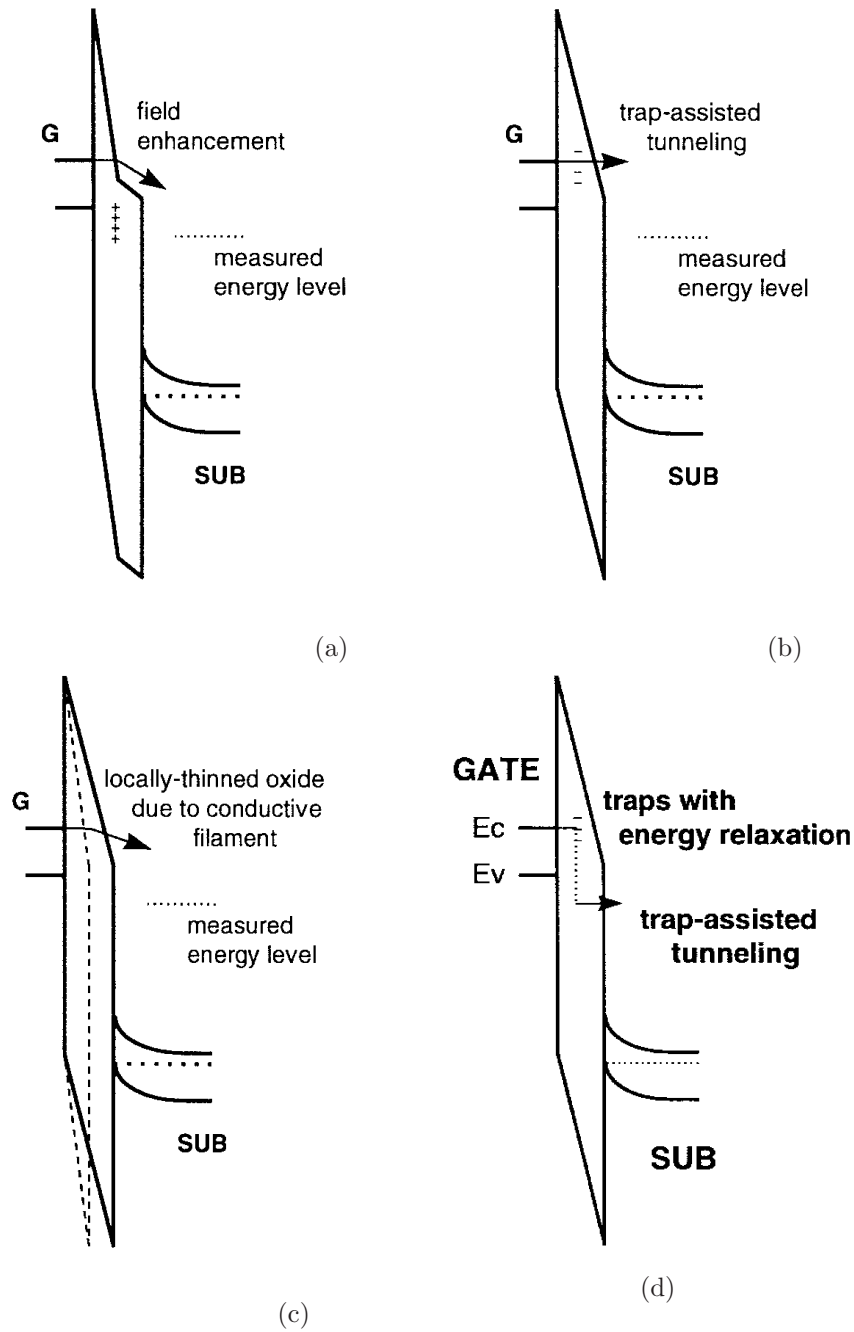


Figure 7.2: The conduction models for SILC [176]; (a) The field enhancement due to trapped positive charges [179,180]; (b) Trap-assisted elastic tunneling model of SILC [182–185]; (c) Conduction due to local thinning of the gate oxide [101,181]; (d) Inelastic trap-assisted tunneling [176]

is useful to model the electron transport in a disordered medium. If the disorder is very strong, the electron wave function may become localized, in that the envelope of the wave function decays exponentially from some point in space (see Figure 7.3b) [193]. Otherwise, the wave nature is extended as it is observed in Figure 7.3a [193].

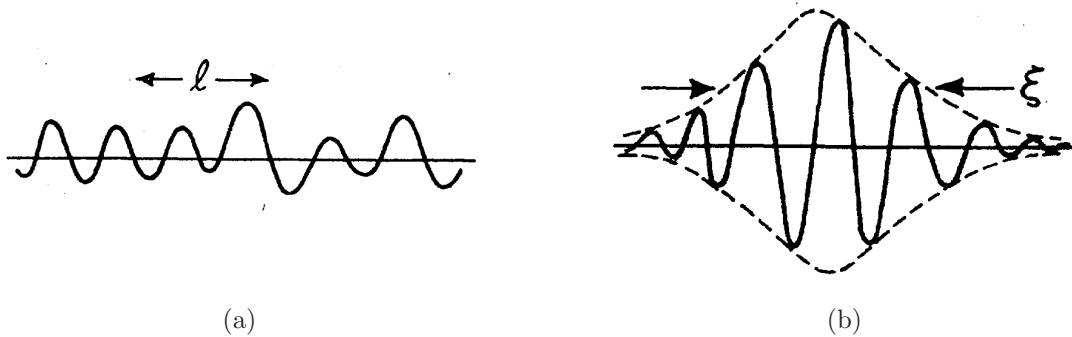


Figure 7.3: Typical wave functions of (a) extended state with mean free path l ; (b) localized state with localization length ξ [193]

In the classical percolation picture, only two phases are defined: percolated or non-percolated [194]. In this theory, we are only concerned with geometrical connection, therefore, the bonds are either conducting or insulating. When the quantum percolation is considered, three phases: “classically localized”, “quantum localized” and “extended” are defined [195]. The appearance of quantum localized phase is due to the wave nature of electrons [196]. The existence of the quantum localized phase causes the classical and quantum percolation thresholds to be significantly different [194, 196]. Increase of percolation threshold is observed considering the quantum effects [197]. Studying the quantum effects on the percolation threshold and the mobility edge as in amorphous materials is beyond the scope of this research, and the reader is referred to [198] for details.

In quantum percolation theory, no conduction from site to site (*i.e.*, a blocked bond) is

modeled with the infinite site energy or the zero transfer energy [194]. This infinite potential barrier prohibits the propagation of a quantum particle and makes the quantum problem formally similar to the classical problem [196]. In real systems, however, the potential barrier may not be infinite even though it prohibits propagation of a classical particle and the classical percolation picture is still valid for classical particles [194]. For quantum particles, the finiteness of the potential barrier height brings in another important quantum effect, namely, tunneling effect [194,196]. It is physically interesting and important to study quantum tunneling effects since they realistically reflect the physical situation of disordered materials [194].

Quantum tunneling can be incorporated in the quantum percolation model by reducing the barrier height of the infinite potential to a finite value so that the tunneling probability is non-zero. When tunneling is taken into consideration, it competes with the localization effect and tends to reduce the percolation threshold [194].

Consideration of the tunneling effects changes the three phases of the percolation theory. If the tunneling is sufficiently weak, we would expect to have similar phases. As the tunneling strength increases, the quantum percolation threshold decreases and will eventually crossover to the classical percolation threshold. In this case, the quantum percolation threshold is smaller than its classical counterpart and now the three phases are: “localized”, “quantum tunneling” and “extended”. Localization transition does not take place when tunneling is sufficiently strong.

A tunneling effect, and the reduction of the percolation threshold, can phenomenologically produce the SILC inside the dielectric. Considering such a phenomenon, I model the SILC as a tunneling conduction through the oxide at lower barrier height.

7.3 Modeling of SILC as Parallel Tunneling through Broken Path and the Whole Oxide

Assuming that applying a high field stress on silicon dioxide generates defects inside the oxide is the basis of this model. Since the stress is not applied for a long time, the accumulation of defects up to the critical defect density is not achieved, and the breakdown does not occur. This is true if we consider the electrons as classical particles.

Although the number of the generated defects is not enough to overlap and create a conducting path, there is a probability that electrons tunnel from one trap site to the other.

One can explain the formation of this conducting path with a Monte-Carlo simulation. However, the experimental results obtained by different research groups during the last decade show that the conduction process after creation of such a path is not a percolation conduction, but mostly similar to a quantum tunneling [172–174].

In this work, I propose that the stress-induced leakage current can be modeled as a quantum tunneling through the isolated traps. It appears reasonable that there exists a non-zero probability of tunneling between traps due to the wave-nature of the electron. In a detailed and parametric way, Kramer et al. [196] show that near the points where percolating wave functions approach each other closely, quantum tunneling takes place, and the percolating wave functions of the electron carry an equilibrium current density.

7.3.1 Fowler-Nordheim Tunneling

The theory of Fowler-Nordheim emission is used to find the tunneling current inside a dielectric. In Fowler-Nordheim mechanism, electrons tunnel through the energy barrier at

the cathode interface to the conduction band of insulator and drift to the anode [199]. In the simplest case for emission into vacuum, a triangular barrier and the temperature $T = 0$ K are assumed. Using a free-electron gas model for the metal and the Wentzel-Kramers-Brillouin (WKB) approximation for the tunneling probability expressed as a Taylor series expansion at the Fermi level, one obtains the following expression for the current density [200]:

$$J = AE_{ox}^2 \exp\left(-\frac{B}{E_{ox}}\right) \quad (7.1)$$

$$A = \frac{q^3}{8\pi h\phi}$$

$$B = -\frac{4(2m)^{1/2}\phi^{3/2}}{3\hbar q}$$

where h = Planck's constant, q = electronic charge, E_{ox} = electric field inside the oxide, ϕ = barrier height, and m = free-electron mass.

7.4 Simulation of Tunneling with MATLAB

The experimental results in this chapter are extracted from [179]. In this paper, n+ poly-Si gate-thermal oxide-n+ Si substrate MOS capacitors with area of 10^{-4} cm² have been stressed with ramp voltage stresses, and the pre-stress and post-stress leakage currents have been measured for each sample.

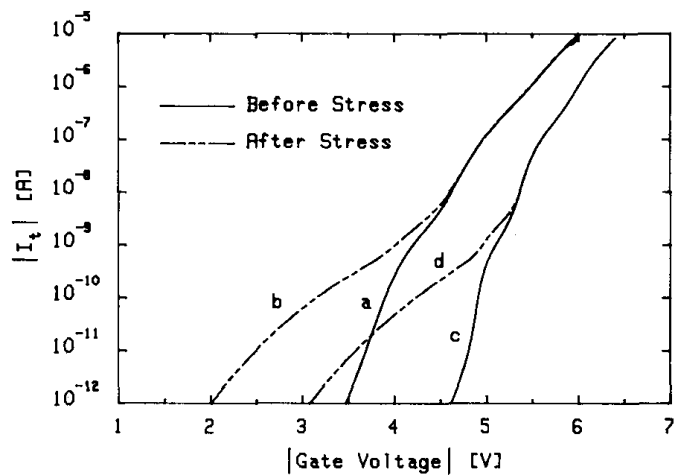
By fitting the experimental results to Fowler-Nordheim (F-N) curves, it is observed that the conducting path must have a small area and lower tunneling barrier. The small

barrier results in higher leakage current in low field region, but having a smaller area of the path compared to the whole area of the oxide causes a dominant quantum tunneling through the whole insulator at high electric fields.

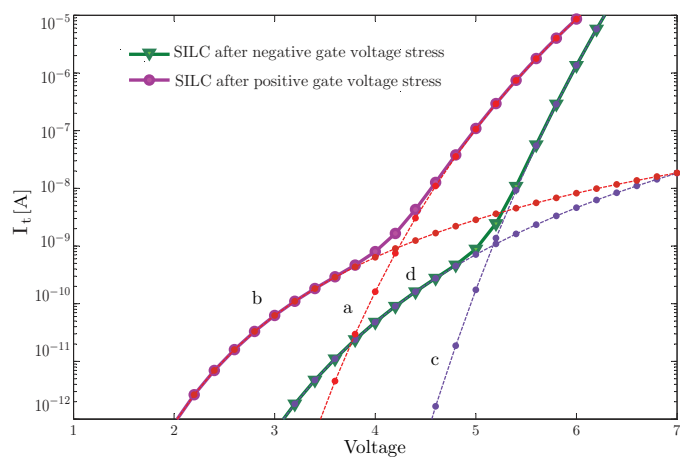
Figure 7.4a depicts the leakage current through virgin and stressed oxides, for two similar samples. Both oxides are 5.1 nm thick and have been stressed applying a ramp voltage stress up to 12 MV/cm. Curves (a) and (c) are the tunneling currents through virgin oxide that have been measured using positive and negative voltage respectively. Curve (c), therefore, depicts hole current while curve (a) represents the electron current. It is proved in the literature that these currents are due to Fowler-Nordheim tunneling process. In Figure 7.4b, the SILC is modeled using F-N tunneling (Equation 7.1). The barrier energy is found to be 2.2923 and 3.7547 eV for electron and hole tunneling, respectively. The results are in Table 7.1.

In Figure 7.4a, curves (b) and (d) represent the post-stress currents. That curves (b) and (d) can be modeled as two parallel F-N tunnelings. Fig 7.4b shows the curves (a), (b), (c) and (d) fitted to F-N tunneling. From the simulation data, it is found that for both positive and negative stressed samples, the electron and hole barrier energy reduces to 30% of the energy barrier in the virgin devices. The ratio of the effective area of the low-barrier tunneling path to the whole oxide area is about 0.17×10^{-10} . This area, however, is the effective area. It means that current goes through many parallel tunneling-percolating paths distributed over the oxide area which act as a F-N tunneling with this effective area.

Figure 7.5a illustrates the currents before and after positive and negative voltage stresses. The curves (a) and (b) are the virgin device's current, while curves (c) and (d) are post-stress currents. Both post-stress currents are measured by applying positive gate voltage. It is observed that the the polarity of the stress electric filed does not affect



(a)



(b)

Figure 7.4: (a) The curves illustrate the experimental I-V characteristics of two similar 5.1 nm oxide n+ poly gate capacitors (area of 10^{-4} cm²) after a ramp voltage stress up to an oxide field of $E_{ox} = 12$ MV/cm [179]. (b) The simulation of the experimental I-V characteristics with two parallel F-N tunneling currents

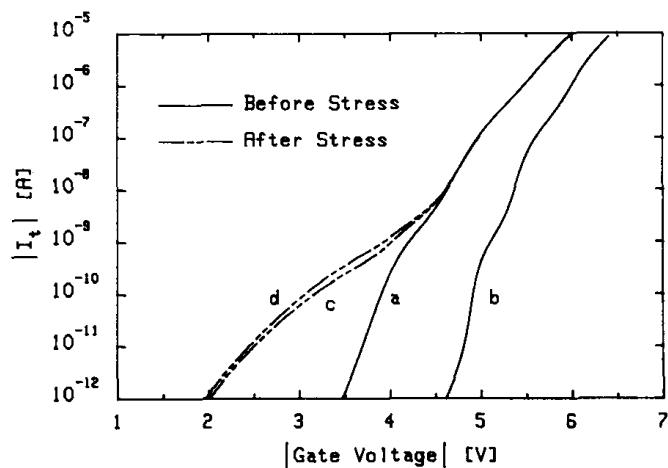
Table 7.1: The tunneling energy barriers resulted from the simulation of I-V curves in Figure 7.4a with F-N tunneling current; The energy barriers are calculated for the virgin device current and after applying the ramp gate voltage stress.

(a) Current is measured by applying positive gate voltages. $\frac{\phi_S}{\phi_V} = 0.31$ and $\frac{A_{SILC}}{A_{ox}} = 1.77 \times 10^{-11}$

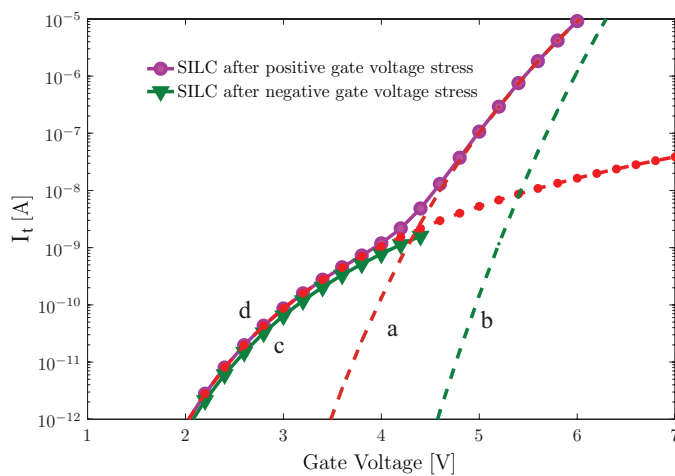
Device status	Tunneling Barrier (ϕ_S) (eV)
Virgin	2.2923
Stressed	0.77943

(b) Current is measured applying negative gate voltages. $\frac{\phi_S}{\phi_V} = 0.31$ and $\frac{A_{SILC}}{A_{ox}} = 4.26 \times 10^{-19}$

Device status	Tunneling Barrier (ϕ_S) (eV)
Virgin	3.7547
Stressed	1.3067



(a) Experimental I-V Characteristics [179]



(b) Simulation of the SILC as the sum of two parallel F-N tunneling

Figure 7.5: The after-stress I-V characteristics are measured with positive gate voltage after positive and negative voltage stress. The curves illustrate the independence of the stress induced leakage current on the stress polarities.

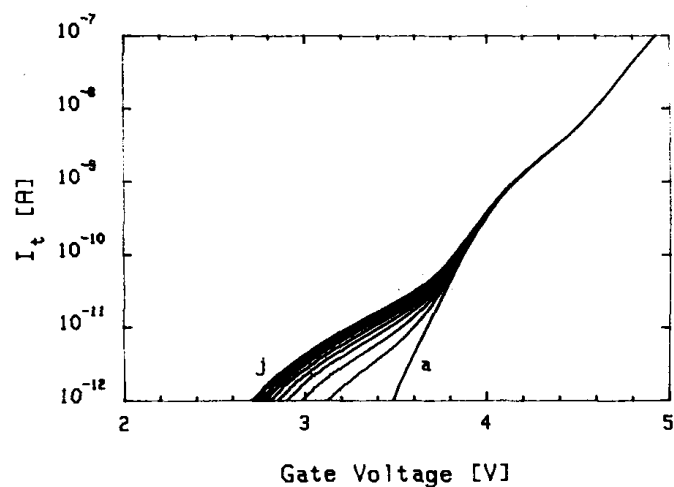
Table 7.2: The tunneling energy barriers before and after applying positive and negative voltage stress; The results show the independence of the SILC on the polarity of the stress.

(a) The virgin current and the after stress current, both, are measured using positive ramp voltage stress. $\frac{\phi_S}{\phi_V} = 0.33$ and $\frac{A_{SILC}}{A_{ox}} = 2.12 \times 10^{-11}$

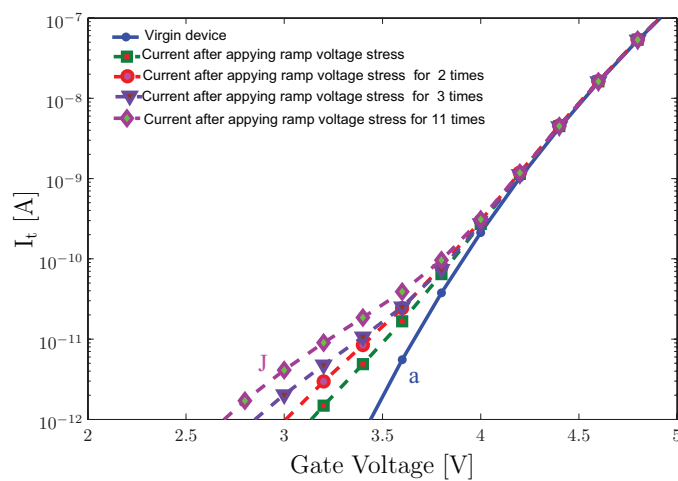
Device status	Tunneling Barrier (ϕ_S) (eV)
Before applying the stress	2.2154
After applying the stress	0.72142

(b) Positive voltage is applied to measure the current after applying the negative voltage stress. $\frac{\phi_S}{\phi_V} = 0.33$ and $\frac{A_{SILC}}{A_{ox}} = 2.99 \times 10^{-11}$

Device status	Tunneling Barrier (ϕ_S) (eV)
Before applying the stress	3.6237
after applying stress	0.72419



(a) Experimental results



(b) Simulation results

Figure 7.6: Leakage current increase induced by repeated voltage ramps; (a) Sequence of curves (from a, virgin device, to j) with the same maximum voltage (5.5 V) [179]

Table 7.3: The tunneling energy barriers that are calculated using the experimental results in Figure 7.6a, showing the dependence of after-stress current on repeating the stress.

Device status	Tunneling Barrier (ϕ_S)
Before applying the stress (Virgin device)	2.2051 eV
After applying ramp voltage stress for 1 time	1.8474 eV
After applying ramp voltage stress for 2 times	1.1635 eV
After applying ramp voltage stress for 3 times	0.98025 eV
After applying ramp voltage stress for 9 times	0.98514 eV

the SILC.

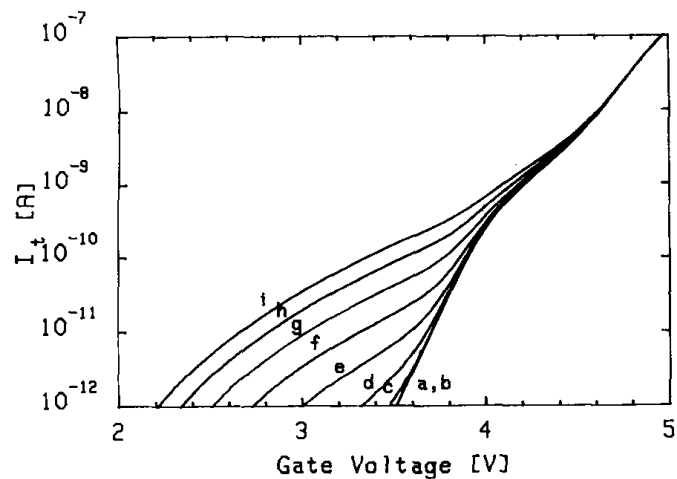
Repeating the ramp voltage stress increases the SILC, as depicted in Figure 7.6a. This is a good confirmation that the accumulation of defects inside the oxide is the cause of SILC, and therefore the quantum percolation is found to be a reasonable model for the SILC.

The experimental SILC results in Figure 7.7a illustrate that the SILC increases by increasing the stop voltage of the ramp stress.

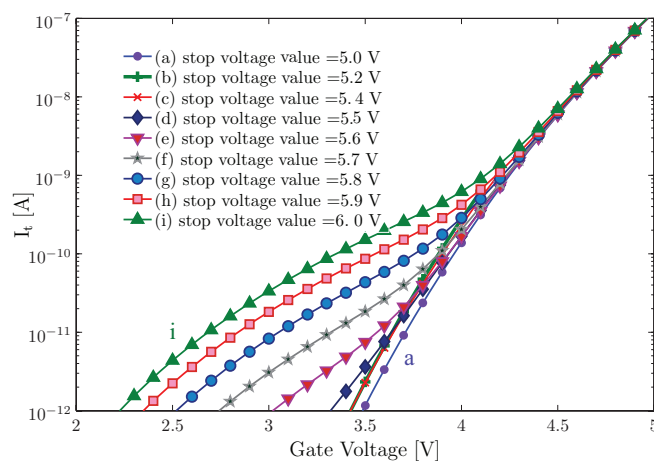
Figure 7.8a depicts the dependence of SILC on temperature. The virgin oxide current and the SILC have been measured at four different temperatures of 77 K, 23 °C, 100 °C and 250 °C.

Fitting the post-stress currents to two parallel-tunneling paths, the barrier energy and effective area of the SILC current path has been found. The fitted curves are observed in Figure 7.8b, and the simulation results are presented in Table 7.5.

Figure 7.9a shows the dependence of the leakage current on oxide thickness. All the



(a) Experimental results

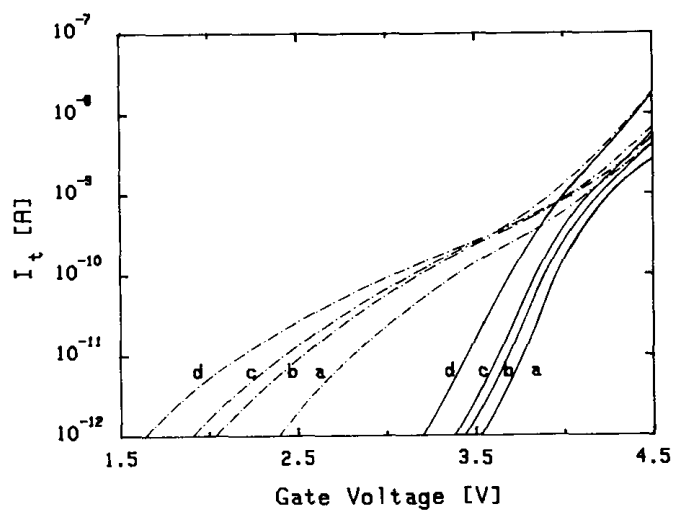


(b) Simulation results

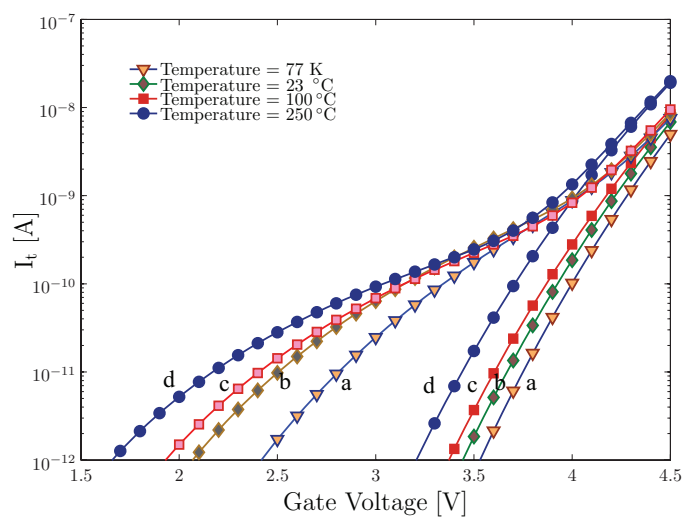
Figure 7.7: The leakage current increase depends on the maximum applied voltage [179]. The voltage ramp is repeated on the same capacitor with increasing stop values: 5 V (curve a, virgin sample), 5.2 V (curve b), 5.4 V (curve c), 5.5 V (curve d), 5.6 V (curve e), 5.7 V (curve f), 5.8 V (curve g), and 5.9 V (curve h).

Table 7.4: The tunneling energy barriers that are calculated using the experimental results in Figure 7.7a, showing the dependence of after-stress current on the stop voltage of the ramp stress.

Stop-Voltage of the ramp I-V stress (V)	Tunneling Barrier (ϕ_S) (eV)	$\frac{\phi_S}{\phi_V}$
5	2.2433	1
5.2	2.2433	1
5.4	2.1215	0.95
5.5	1.9413	0.87
5.6	0.94458	0.42
5.7	0.85176	0.38
5.8	0.81783	0.36
5.9	0.78817	0.35
6	0.76547	0.34



(a) Experimental results



(b) Simulation results

Figure 7.8: Before-stress (solid lines) and after-stress (dashed-dotted lines) characteristics at different temperatures (77 K (curve a), 23 °C (curve b), 100 °C (curve c), and 250 °C (curve d)); Curves b, c, and d were obtained from the same device, and curve a from a similar device presenting the same virgin I-V characteristic at room temperature [179].

capacitors were prepared by the same fabrication process and subjected to the same stress conditions. In Figure 7.9a, curves (a), (b), (c) and (d) represent the current for 5.1 nm, 6.0 nm, 7.5 nm and 9.7 nm thick thermal oxides, respectively. It is observed that the post-stress leakage current increases significantly in very thin oxides.

Fitting the pre-stress current to F-N tunneling (see Figure 7.9b), we observe that the tunneling energy barrier is the same for all oxide thickness, $\phi_V = 2.35$ eV, which is reasonable. Barrier energy extracted from fitting the post-stress currents decreases by oxide thickness reduction. The results are presented in Table 7.7.

The strong dependence of SILC on thickness can be explained by the quasi-critical nature of percolation for ultra-thin oxides. As explained in chapter 5, the quasi-critical nature of the percolation results in the creation of several separate small area conduction paths through the oxide. The same phenomenon occurs for SILC, with the difference that the number of defects is not that high to conduct classical particles, and the conduction between the traps in the oxide occurs by tunneling.

7.5 Summary and Conclusion

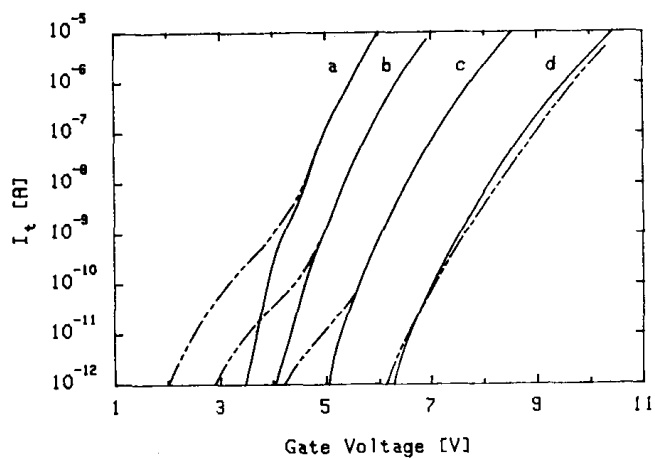
In this chapter, I have showed that the SILC can be explained with the concept of “quantum percolation”. In quantum percolation, the states are categorized to three phases of “classically localized”, “quantum localized” and “extended”. Due to wave nature of electrons in quantum scale, the overlap of electron energy in some states results in tunneling between them, even though those sites are not physically connected. The threshold of conduction also decreases, compared to classical percolation. Using this model, I explained how accumulation of defects inside oxide causes the creation of tunneling conducting paths,

Table 7.5: The tunneling energy barriers that are calculated using the experimental results in Figure 7.8, showing the dependence of after-stress current on temperature.

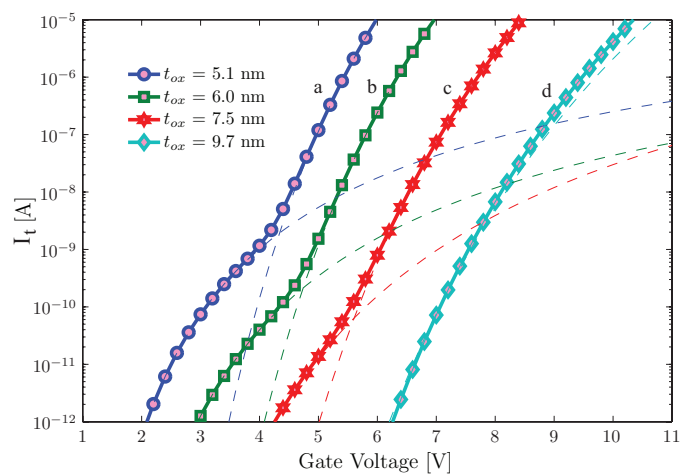
	Device status	Tunneling Barrier (ϕ_S) (eV)
T=77 K	virgin	2.2433
	stressed	0.99345
T=23 °C	virgin	2.0474
	stressed	0.67315
T=100 °C	virgin	1.701
	stressed	0.49931
T=250 °C	virgin	1.3366
	stressed	0.3267

Table 7.6: The tunneling energy barriers that are calculated using the experimental results in Figure 7.8, showing the dependence of after-stress current on temperature.

Temperature	$\frac{\phi_S}{\phi_V}$	$\frac{A_{SILC}}{A_{ox}}$
77 K	0.41	9.33×10^{-10}
23 °C	0.33	2.46×10^{-10}
100 °C	0.29	2.40×10^{-10}
250 °C	0.24	2.16×10^{-10}



(a) Experimental results



(b) Simulation results

Figure 7.9: Dependence of the leakage current on the oxide thickness; The I-V curves are from virgin and stressed samples. The oxide thickness is: 5.1 nm (curve a), 6.0 nm (curve b), 7.5 nm (curve c), and 9.7 nm (curve d) [179].

Table 7.7: The change of tunneling energy barrier of the damaged current path with oxide thickness; The results are based on the experimental data presented on Figure 7.9a. The data is collected based on the current inside virgin and stressed oxide samples with thickness = 5.1 nm, 6.0 nm, 7.5 nm, and 9.7 nm.

	Device status	Tunneling Barrier (ϕ_S) (eV)
$T_{ox} = 5.1$ nm	virgin device	2.3431
	after applying stress	0.79141
tox=6.0 nm	virgin device	2.3572
	after applying stress	0.89059
tox=7.5 nm	virgin device	2.3623
	after applying stress	1.1565
tox=9.7 nm	virgin device	2.3534
	after applying stress	2.2397

before the breakdown happens. Therefore, we modeled the SILC as a combination of two parallel tunneling paths. The tunneling through the defects, that are made by applying high electric field stress, occurs at smaller energy electrons which can be modeled by a smaller band barrier voltage. This tunneling path occurs because of the overlap of quantum localized states, and appears as a small effective area path. The tunneling at high electric fields is through the whole area of the oxide which dominates over smaller defective areas.

Chapter 8

Summary and Conclusion

8.1 Summary

The primary objective of the thesis is to investigate the complex conduction behaviors of gate oxides as they occur at breakdown or under stress. Since the oxides are being thinned down due to scaling, these issues are important both from the point of reliability and understanding. Using percolation theory and Markov modeling approaches breakdown characteristics of the gate oxides have been studied. Percolation theory had been used to model and study both soft and hard breakdown characteristics.

It was shown that by using a constant probability of defect generation (CPDG), the results of CVS or CCS reliability tests were simulated. In this method, a constant stress was applied to a set of samples, causing gradual degradation and accumulation of defects inside the oxide films. The time-to-percolation was calculated as a measure of time-to-breakdown.

Using this method, the breakdown statistics were successfully characterized for different

thickness and width of the oxide, and also different stress conditions.

Using the percolation model developed, Time-to-breakdown (T_{BD}) and Weibull slope (β) were calculated, fitting the generated failure data to a Weibull failure function. From the simulation results, it was found that the Weibull slope changes linearly with oxide thickness, and remains almost constant by changing the oxide width and the oxide area.

T_{BD} was shown to increase as a function of thickness, but almost saturates for very large thickness. Change of T_{BD} with oxide width was recognized to follow a power-law relationship. Lifetime was shown to decrease by increasing the applied stress. It was shown that T_{BD} has a power-law relationship with the applied stress, as well.

To simulate the electrical conduction at post-breakdown, a parallel-series resistor network model developed. In this model, the conducting path in a site percolation network is modeled as a combination of series of parallel resistors. Using this model, the post-breakdown conductance in the oxide, after soft and hard breakdown, could be realistically calculated.

It was found that decreasing the oxide thickness results in the emergence of some plateaus in the post-breakdown current. These plateaus are known as soft-breakdown in the literature. The simulations in this thesis show that these effects emerge when the width of the samples are increased, thus resulting in the softening of the breakdown.

Breakdown statistics and post-breakdown conductance simulation results are shown to match the experiments quite well. This study demonstrates that the proposed Monte-Carlo simulation method offers a useful method to understand the physics and origin of breakdown.

It was discussed how the effect of change of thickness and width of samples on the breakdown statistics and the post-breakdown current can be justified by percolation theory.

For this purpose, it was argued that the breakdown can be considered as a phase-transition from a non-conducting (insulating) to a conducting state. By plotting the percolation probability versus defect density, it was shown that thinning of oxides results in a more gradual phase transition, with a smaller threshold. This was named as a quasi-critical phase transition, which results in quasi-breakdown.

As a different approach, the electron transport inside the oxide was modeled as a Markov chain process. The trap sites work as absorbing states and confine the electron transport through the oxide. The absorbing states, however, conduct current when enough traps are accumulated inside the oxide and a path is created. Using this model, the effect of detrapping of electrons was simulated. It was discovered that the trapping-detrapping of electrons results in a $1/f$ noise in the current.

Modeling of the defected oxide as a disordered material, the conductance was calculated using Markov chain. In this method, the voltage was interpreted as the hitting probability if a unit voltage is applied to the sample, and the current was interpreted as the expected number of net transitions in each branch.

Introducing a concept of quantum percolation, the origin of the stress-induced leakage current was explained. In quantum percolation, the states are categorized to three phases of classically localized, quantum localized and extended. Due to wave nature of electrons in quantum scale, the overlap of electron energy in some states results in tunneling between them, even though those sites are insulated from each other electrically. Then, the threshold of conduction decreases compared to the classical percolation. In this thesis, this fact was described as a cause of the SILC, before the defect density reaches the critical defect density and the breakdown occurs. In such a way, the SILC was simulated as a combination of two parallel tunneling paths, one through the localized states, occurring at low electric fields,

and one through the whole oxide area which dominates at high electric fields.

An analytical expression was developed to describe the percolation probability versus defect density in a 2-D ($M \times N$) site percolation model. The complexity of the problem was reduced via using recursive approaches of counting. For $3 \times N$, $4 \times N$ and $M \times 2$ networks, another method was introduced and closed-form expressions were obtained for the percolation probability.

8.2 Future Works

The proposed percolation model lacks the explicit analysis of effects of different parameters, such as temperature and gate voltage polarity, on the breakdown.

As an extension of the proposed model, the following research issues are proposed:

- Studying and understanding the effect of temperature on breakdown characteristics is important for the advantage of projection of the reliability from the statistical data collected at accelerated temperatures. Hamilton et al. [201] studied the conductivity of porous silicon films using the percolation theory. They suggested that the temperature dependence of conductance may be understood in terms of a percolation process occurring through sites in the porous network in which the conductivity is thermally activated [201]. In this work, the authors assumed that the activation energy may be the consequence of the Coulomb blockade effect [202, 203] in the porous medium. This assumption can be also used to explain the temperature-dependence of time-to-breakdown and also the post-breakdown conductance in ultra-thin oxides.
- To investigate the polarity-dependence of the oxide breakdown, the use of a directed-

percolation model is suggested. For such a purpose, a random resistor-diode network rather than a resistor-network can be used to model the defected oxide. It has been shown in the literature that using a random diode-resistor network results in an anisotropic behavior of the system, and different percolation thresholds are observed depending on the polarity of the voltage [204,205]. Solving the Laplace equations in the lattice, depending on different configuration of the traps, is a challenging issue in this research.

In a more advanced model, it seems reasonable to consider the gate tunneling current as the source of the stress and the origin of defect generation inside the oxide. It worths mentioning that the exact origin of defect generation inside the oxide is still unclear. Compared to the majority carrier (electron) current, the smaller minority carrier (hole) current will result in lower rate of defect generation, and longer lifetime of the device. This fact can also affect the polarity dependence of the breakdown characteristics. A carefully designed detailed experimental research is necessary to find the role of current on the defect generation rate.

Use of high-K dielectrics as the future gate insulator is the other important issue to be studied. Due to oxygen ions diffusion out of the gate dielectric to the Si interface, using high-K materials as the gate dielectric results in a 1-2 nm silicon dioxide layer at the interface. Understanding the behavior of the gate-dielectric stack is critical. The breakdown simulation for a high-K dielectric stack, and the effects of the additional thin SiO₂ interface layer, can be considered as a useful extension of this research work. The polarity dependence of breakdown in high-K stack is to be modeled using different stress and critical defect densities in the two layers. Reasonably, the modeling of the high-K

stack is possible by modifying the proposed Markov model. The possible modifications are listed as follows:

- The transition probabilities differ in the two materials due to distinct local electric fields and different barrier height.
- The interface charges at the intersection of the high-K and the SiO₂ can be modeled as a layer of fixed trap states.
- The trapping-detrapping rate must be affected by nature and electric field inside the material.

Moreover, it was shown that the SILC can be modeled as two parallel tunneling currents. However, the simulation results suggested that different parameters such as temperature and the duration of applying the stress affect the barrier height. Understanding the effect of these parameters on the density of the localized electrons, and the localization of the electron wave is an issue to be discovered in the future.

Furthermore, the DC stress gives the upper limit of the reliability. In this dissertation, a constant stress was applied and the effects of a DC stress was studied. As an extension, the effects of a pulsed stress can be analyzed considering a partial reversibility of the breakdown due to repetitive hole and current injection. For a bilayer stack, for example, depending on the polarity of the stress, the defect generation rate would differ in two materials.

The brief discussion above are some of the avenues for further research in this area.

Appendices

Appendix A

Analytical Formulae for Percolation Probability in a 2-D System

Although the percolation problem has been investigated for decades, the exact solution of the problem for an K -dimensional system ($1 < K < \infty$) has not been found yet¹. Therefore, numerical methods have been traditionally used to investigate the percolation behavior. This is so because of the complexity of transport through a disordered system. Thus, finding an analytical approach to describe percolation probability versus defect density would be of critical importance, and will help us for a better understanding of the percolation process.

In this appendix, in section [A.1](#), I elaborate on the complexity of finding percolation probability in a 2-D ($M \times N$) network. I describe how to reduce complexity of the problem via finding recursive ways of counting. For $3 \times N$ and $4 \times N$ networks, another recursive

¹For $K = 1$ the exact formula is discovered. Bethe lattice, also known as Cayley tree, is equivalent to $K = \infty$, and is the other exactly solved percolation problem [129].

approach is introduced in section A.2 and closed-form expressions are obtained for the percolation probability. In section A.3, I present cases with $N = 2$ and let M vary and provide a closed-form formula for the percolation probability.

A.1 Percolation Probability for General $M \times N$ Networks

Naming the appearance of percolating path as a “good” case, the exhaustive search approach for finding “good” cases in our counting problem leads to an exponential complexity in both dimensions of the network. The idea is to use combinatorial arguments to obtain a recursive expression for percolation probability which turns out to be polynomial in one dimension (vertical). This enables us to compute and find closed-form expressions for percolation probability as a function of trap density for an *arbitrary* thickness and a range of widths (the width is limiting here since the complexity grows exponentially with the width as will be shown later).

Assume that we have an $M \times N$ network in which each site (cell) is trapped independently with probability p (trap density). The problem is to find the percolation probability $Q_{M,N}(p)$ defined as probability that there exists a “percolation path” of cells between the lowermost and uppermost rows which satisfies the following conditions:

- It consists of only trapped cells.
- It is 4-connected, *i.e.*, only horizontal and vertical adjacencies in cells are allowed.

Now, since there is a total of 2^{MN} possible patterns, the exhaustive search to obtain $Q_{M,N}(p)$ leads to an exponential complexity in both M and N . The approach here is to

decompose $Q_{M,N}(p)$ into disjoint cases according to trapping pattern of the uppermost row. There are 2^N different patterns for the uppermost row. Considering each of these row patterns as a binary number, define $Q_{M,N}(p|i)$ as the percolation probability of an M -by- N network given that the binary representation of i (denoted by $b(i)$) is the uppermost row pattern. Define $\alpha(i)$ as the number of 1's in $b(i)$. Therefore,

$$Q_{M,N}(p) = \sum_{i=0}^{2^N-1} Q_{M,N}(p|i) p^{\alpha(i)} (1-p)^{N-\alpha(i)} \quad (\text{A.1})$$

A “1-region” in a binary representation is defined as a sequence of 1's in that representation which is terminated by 0's on both sides. For example, 1001110010 has three 1-regions while 0011110000 has only one 1-region. “X-intersection” of i with j is defined as follows:

- Retain in $b(i)$ only those 1-regions which have an intersection with at least one 1-region in $b(j)$, and discard the rest (*i.e.*, convert all of their 1's to 0). Denote by $X(i, j)$ the *integer* equivalent of the resulting binary sequence.

The following theorem gives a recursive expression for percolation probability of an $M \times N$ network:

Theorem A.1. *The percolation probability for an $M \times N$ network with trap density p , $0 \leq p \leq 1$, is equal to (A.1) where $Q_{M,N}(p|i)$ is given by:*

$$Q_{M,N}(p|i) = \sum_{j=1}^{2^N-1} Q_{M-1,N}(p|X(j, i)) p^{\alpha(j)} (1-p)^{N-\alpha(j)}, \quad 1 \leq i \leq 2^N - 1, \quad M > 1 \quad (\text{A.2})$$

$$Q_{1,N}(p|i) = 1 - \delta(i), \quad 0 \leq i \leq 2^N - 1 \quad (\text{A.3})$$

Proof. For $M = 1$, notice that if $i > 0$ then, given that the binary representation of the 1-by- N network is $b(i)$, $Q_{1,N}(p|i) = 1$. If $i = 0$, however, there is no trapped cell and so, $Q_{1,N}(p|0) = 0$.

For $M > 1$, the desired probability is conditioned on the events in which the binary representation of the second row (below the uppermost row) is $b(j)$ for every $1 \leq j \leq 2^N - 1$. Then, for a specific j , it can be easily shown from definition of $X(j, i)$ that, conditioned on having $b(i)$ and $b(j)$ respectively as the uppermost and second row patterns, there is a path between the lowermost and uppermost rows if and only if there is a path connecting the lowermost row to one of the 1's in $b(X(j, i))$ in the second row. But this is equal to the percolation probability of an $(M - 1) \times N$ network conditional on having $b(X(j, i))$ as the uppermost row pattern, or $Q_{M-1,N}(p|X(j, i))$. Then, (A.2) follows immediately from conditioning over $1 \leq j \leq 2^N - 1$. \square

Suppose that we have $X(i, j)$ and $\alpha(i)$ for every $1 \leq i, j \leq 2^N - 1$. It can be seen from (A.2) that if we have $Q_{M-1,N}(p|i)$ for every $1 \leq i \leq 2^N - 1$, then for every $1 \leq i \leq 2^N - 1$, a number of at most 2^N extra additions is needed to calculate $Q_{M,N}(p|i)$. Therefore, at most 2^{2N} extra additions are needed if we increase M by 1. For $M = 1$, from A.3 the total number of additions for $Q_{1,N}(p|i)$ is zero.

Therefore, the total number of additions needed for calculation of $Q_{M,N}(p|i)$ is at most equal to

$$\#(Q(M, N)(p|i)) = (M - 1)2^{2N} \quad (\text{A.4})$$

It is seen from (A.4) that the computational complexity grows linearly with M . It should be noted that computational complexity of $X(i, j)$ and $\alpha(i)$ are all functions of *only* N and do not depend on M .

Using the above argument, for a fixed N , $X(i, j)$ and $\alpha(i)$ (and also $p^{\alpha(i)}(1-p)^{N-\alpha(i)}$) are calculated *once* and saved in the memory. Then, for any $M > 1$, $Q_{M,N}(p|i)$ can be calculated using (A.2) and saved in the memory to be used in calculation of $Q_{M+1,N}(p|i)$. $Q_{M,N}(p)$ is finally calculated using (A.1).

Corrolary A.2. *As a result of theorem A.1 for $M = 2$, it can be shown that*

$$Q_{2,N}(p) = 1 - (1 - p^2)^N, \quad 0 \leq p \leq 1. \quad (\text{A.5})$$

Proof. Although (A.5) can be inferred from (A.2) and (A.1) and doing some simplifications, a direct and more instructive proof is given here:

In a 2-by- N network, the percolation probability is equal to the probability of having at least a trapped column (a column with two trapped cells). Therefore, $\overline{Q}_{2,N}(p) = 1 - Q_{2,N}(p)$ represents the probability of having *no* trapped column or, equivalently, the probability that every column contains at least one non-trapped cell. But, probability of the latter event is $(1 - p^2)^N$, completing the proof. \square

To obtain the results, the percolation probabilities as polynomial functions of trap density p are calculated for a range of M and N using Theorem A.1. The percolation probabilities for $2 \leq M \leq 10$ and $N = 6$ are summarized as follows:

$$Q_{2,6}(p) = -p^2(p^2 - 2)(p^4 - 3p^2 + 3)(p^4 - p^2 + 1) \quad (\text{A.6})$$

$$\begin{aligned} Q_{3,6}(p) = & p^3(p^{15} - 12p^{14} + 68p^{13} - 238p^{12} + 558p^{11} - 872p^{10} + 809p^9 \\ & - 264p^8 - 184p^7 + 92p^6 + 90p^5 - 12p^4 - 39p^3 - 12p^2 + 10p + 6) \end{aligned} \quad (\text{A.7})$$

$$\begin{aligned}
Q_{4,6}(p) = & p^4(p^{20} - 42p^{18} + 148p^{17} - 6p^{16} - 848p^{15} + 1506p^{14} + 24p^{13} \\
& - 2547p^{12} + 1984p^{11} + 898p^{10} - 1308p^9 - 254p^8 + 360p^7 + 188p^6 \\
& - 12p^5 - 63p^4 - 48p^3 - 6p^2 + 20p + 6)
\end{aligned} \tag{A.8}$$

$$\begin{aligned}
Q_{5,6}(p) = & -p^5(p^{25} - 18p^{24} + 153p^{23} - 858p^{22} + 3446p^{21} - 10788p^{20} \\
& + 27944p^{19} - 57772p^{18} + 86014p^{17} - 80926p^{16} + 37688p^{15} \\
& - 2158p^{14} + 3584p^{13} - 11310p^{12} + 3052p^{11} + 2620p^{10} + 416p^9 \\
& - 834p^8 - 288p^7 - 202p^6 + 89p^5 + 126p^4 + 74p^3 - 18p^2 - 30p - 6)
\end{aligned} \tag{A.9}$$

$$\begin{aligned}
Q_{6,6}(p) = & -p^6(p^{30} - 138p^{28} + 1284p^{27} - 5280p^{26} + 8196p^{25} + 18842p^{24} \\
& - 123660p^{23} + 272346p^{22} - 261488p^{21} - 52700p^{20} + 392344p^{19} \\
& - 333835p^{18} - 3084p^{17} + 147286p^{16} - 62132p^{15} + 23820p^{14} \\
& - 45228p^{13} + 23236p^{12} + 176p^{11} + 2780p^{10} - 2240p^9 + 96p^8 \\
& - 932p^7 - 189p^6 + 276p^5 + 248p^4 + 80p^3 - 60p^2 - 40p - 6)
\end{aligned} \tag{A.10}$$

$$\begin{aligned}
Q_{7,6}(p) = & p^7(p^{35} - 24p^{34} + 256p^{33} - 2152p^{32} + 13442p^{31} - 55694p^{30} \\
& + 158895p^{29} - 394016p^{28} + 1139514p^{27} - 3319396p^{26} + 7286887p^{25} \\
& - 10573794p^{24} + 9041098p^{23} - 2869430p^{22} - 1991290p^{21} \\
& + 1946512p^{20} - 269364p^{19} + 254628p^{18} - 736129p^{17} + 454658p^{16} \\
& - 158822p^{15} + 148908p^{14} - 84098p^{13} + 13954p^{12} - 8350p^{11} \\
& + 1172p^{10} + 960p^9 + 732p^8 + 2003p^7 - 104p^6 - 682p^5 - 416p^4 \\
& - 34p^3 + 120p^2 + 50p + 6)
\end{aligned} \tag{A.11}$$

$$\begin{aligned}
Q_{8,6}(p) = & p^8(p^{40} - 260p^{38} + 3768p^{37} - 30140p^{36} + 161796p^{35} - 573076p^{34} \\
& + 1067320p^{33} + 722254p^{32} - 10712680p^{31} + 31903842p^{30} \\
& - 49232756p^{29} + 32115174p^{28} + 23391028p^{27} - 66417284p^{26} \\
& + 49029856p^{25} + 566043p^{24} - 20400632p^{23} + 6522094p^{22} \\
& + 3357584p^{21} - 804924p^{20} + 355468p^{19} - 2519364p^{18} + 1963376p^{17} \\
& - 677556p^{16} + 371716p^{15} - 180042p^{14} + 27032p^{13} - 4668p^{12} \\
& - 11888p^{11} + 746p^{10} + 2592p^9 + 3009p^8 + 3176p^7 - 966p^6 \\
& - 1424p^5 - 574p^4 + 96p^3 + 198p^2 + 60p + 6)
\end{aligned} \tag{A.12}$$

$$\begin{aligned}
Q_{9,6}(p) = & -p^9(p^{45} - 30p^{44} + 211p^{43} - 1098p^{42} + 19475p^{41} - 225360p^{40} \\
& + 1328913p^{39} - 4181004p^{38} + 5453475p^{37} + 6264470p^{36} \\
& - 25372802p^{35} - 36409036p^{34} + 338146825p^{33} - 866610354p^{32} \\
& + 1208299756p^{31} - 903702720p^{30} + 156306219p^{29} + 282778156p^{28} \\
& - 133079855p^{27} - 116840990p^{26} + 93017278p^{25} + 16848612p^{24} \\
& - 14369657p^{23} - 17062790p^{22} + 8885744p^{21} - 3137762p^{20} \\
& + 9066205p^{19} - 7354090p^{18} + 2534720p^{17} - 917338p^{16} \\
& + 367066p^{15} - 98884p^{14} + 24578p^{13} + 18110p^{12} + 22380p^{11} \\
& - 5050p^{10} - 7677p^9 - 7182p^8 - 3924p^7 + 2912p^6 + 2600p^5 \\
& + 608p^4 - 342p^3 - 294p^2 - 70p - 6)
\end{aligned} \tag{A.13}$$

$$\begin{aligned}
Q_{10,6}(p) = & p^{10}(5p^{50} - 160p^{49} + 2506p^{48} - 24814p^{47} + 168681p^{46} - 872280p^{45} \\
& + 4054776p^{44} - 18437808p^{43} + 72195696p^{42} - 199980844p^{41} \\
& + 285737512p^{40} + 259275474p^{39} - 2379976260p^{38} + 5914009936p^{37} \\
& - 7926931846p^{36} + 4669667052p^{35} + 2750675084p^{34} - 7339011340p^{33} \\
& + 4656742582p^{32} + 761992670p^{31} - 2295906622p^{30} + 441978308p^{29} \\
& + 454823580p^{28} + 198138736p^{27} - 444550902p^{26} + 126493308p^{25} \\
& - 51473670p^{24} + 122796702p^{23} - 78574644p^{22} + 36026808p^{21} \\
& - 38084548p^{20} + 25598888p^{19} - 8155912p^{18} + 2062112p^{17} - 539348p^{16} \\
& + 139004p^{15} + 64864p^{14} - 85496p^{13} - 51814p^{12} - 27568p^{11} + 14739p^{10} \\
& + 20812p^9 + 13042p^8 + 3032p^7 - 6736p^6 - 4180p^5 - 346p^4 + 736p^3 \\
& + 408p^2 + 80p + 6)
\end{aligned} \tag{A.14}$$

Figure A.1 plots the percolation probabilities versus trap density $0 \leq p \leq 1$ for $N = 6$ and $1 \leq M \leq 10$.

A.2 Percolation Probability for $3 \times N$ and $4 \times N$ Networks

Since networks with large area and small thickness are more typical in the oxide percolation analysis, in this section, we let N be an arbitrary parameter while setting M to be fixed ($M = 3$ and $M = 4$). Recursive approaches will be deployed for $Q_{3,N}(p)$ and $Q_{4,N}(p)$ in terms of N which result in closed-form expressions.

Before going through the theorems, let us define an auxiliary function $Q_{M,N}^b(p)$ where

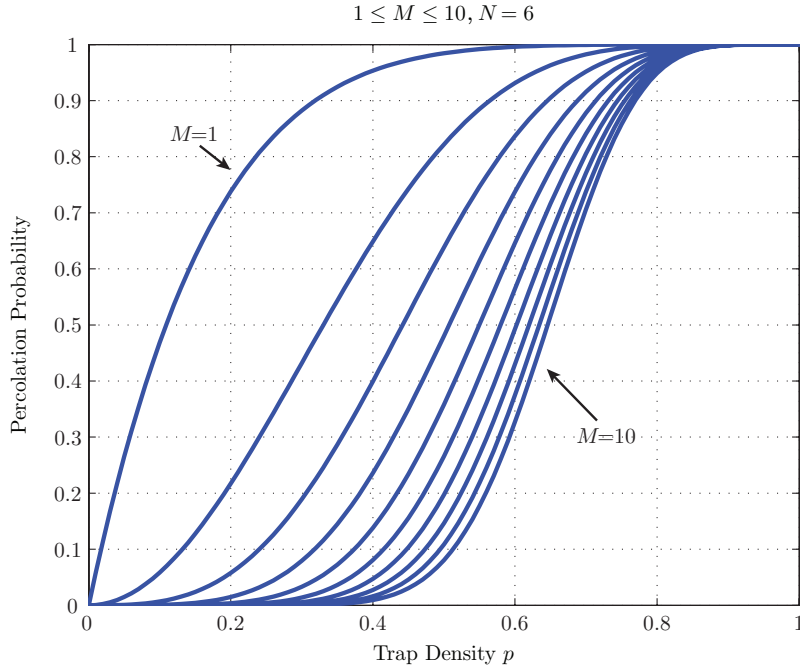
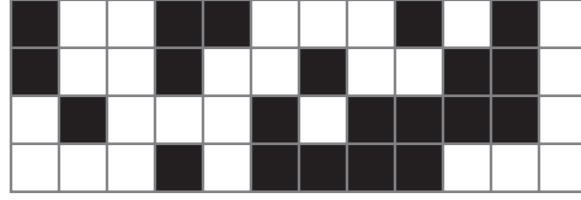
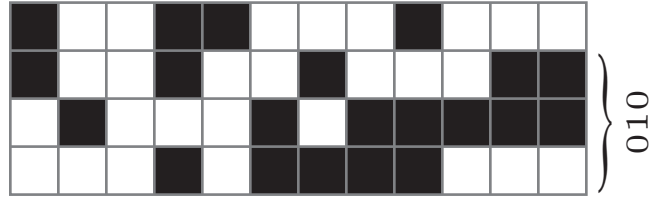


Figure A.1: Percolation probability for $N = 6$ and $1 \leq M \leq 10$ obtained using Theorem [A.1](#)

b is an arbitrary $(M - 1)$ -bit binary pattern. $Q_{M,N}^b(p)$ is the probability that an $M \times N$ network (trapped with trap density p) has a path connecting the lowermost row to any cell in the uppermost row *or* any cell in the rightmost column whose corresponding place in b is 1.

To clarify this definition, Figure [A.2](#) exemplifies this auxiliary function for $b = 010$, $M = 4$, $N = 12$. While the network shown in Figure [A.2a](#) is counted in both $Q_{4,12}(p)$ and $Q_{4,12}^{(010)}(p)$, the network of Figure [A.2b](#) is counted only in $Q_{4,12}^{(010)}(p)$. Obviously, we have $Q_{M,N}^b(p) \geq Q_{M,N}(p)$ for any b , and also, $Q_{M,N}^{(00\dots0)}(p) = Q_{M,N-1}(p)$.

The results are summarized in the following two theorems:

(a) A network counted in both $Q_{4,12}(p)$ and $Q_{4,12}^{(010)}(p)$ (b) A network counted only in $Q_{4,12}^{(010)}(p)$ Figure A.2: An example for the auxiliary function $Q_{4,12}^{(010)}(p)$

Theorem A.3. For any $N > 1$ and $0 \leq p \leq 1$, $Q_{3,N}(p)$ is given by the following recursion:

$$\underline{Q}_{3,N}(p) = \underline{Q}_{3,1}(p) + \mathbf{A}(p)\underline{Q}_{3,N-1}(p) \quad (\text{A.15})$$

where,

$$\begin{aligned} \underline{Q}_{3,1}(p) &= [p^3, p^2]^T, \\ \underline{Q}_{3,N}(p) &= [Q_{3,N}(p), Q_{3,N}^{(10)}(p)]^T, \\ \mathbf{A}(p) &= (1-p) \begin{pmatrix} 1+p-p^2 & 2p^2 \\ 1 & p \end{pmatrix}. \end{aligned}$$

Furthermore, the solution to this recursive equation is as follows:

$$\underline{Q}_{3,N}(p) = [\mathbf{I} - \mathbf{A}(p)]^{-1} [\mathbf{I} - (\mathbf{A}(p))^N] \underline{Q}_{3,1}(p). \quad (\text{A.16})$$

Proof. The recursive formula can be obtained by considering the percolation probability $Q_{3,N}(p)$ conditioned on having a specific pattern as the rightmost column, multiplying by

probability of that column pattern, and then summing over all of the possible column patterns. Therefore, eight possible column patterns attend the summation by a their corresponding terms as listed in Table A.1 which can be easily verified.

As it is observed in the table, the auxiliary function $Q_{3,N-1}^{(10)}(p)$ enters the calculation of $Q_{3,N}(p)$ which calls for finding a recursive equation for $Q_{3,N}^{(10)}(p)$. Using the same approach as $Q_{3,N}(p)$, the eight possible column patterns for $Q_{3,N}^{(10)}(p)$ and their corresponding terms are also summarized in Table A.1.

Using these two tables, the vector recursive equation A.15 is obtained for the vector $\underline{Q}_{3,N}(p) = [Q_{3,N}(p), Q_{3,N}^{(10)}(p)]^T$. The initial condition $\underline{Q}_{3,1}(p) = [p^3, p^2]^T$ is easily verified from the definition. Since, the linear recursive equation (A.15) with the given initial condition has a unique solution, the final solution (A.16) can be readily verified by substituting in (A.15). Note finally that, the desired percolation probability $Q_{3,N}(p)$ is the first element of the vector $\underline{Q}_{3,N}(p)$. \square

A similar argument can be deployed to establish the following result for a $4 \times N$ network:

Theorem A.4. *For any $N > 1$, $Q_{4,N}(p)$ is given by the following recursion:*

$$\underline{Q}_{4,N}(p) = \underline{Q}_{4,1}(p) + \mathbf{B}(p)\underline{Q}_{4,N-1}(p) \quad (\text{A.17})$$

where,

$$\underline{Q}_{4,1}(k) = [p^4, p^2, p^3, p^2]^T,$$

$$\underline{Q}_{4,N}(p) = \left[Q_{4,N}(p), Q_{4,N}^{(010)}(p), Q_{4,N}^{(100)}(p), Q_{4,N}^{(110)}(p) \right]^T,$$

$$\mathbf{B}(p) = (1-p) \begin{pmatrix} (1-p)(1+p)^2 & 0 & 2p^2 & 2p^3 \\ (1-p)(1+p) & p(1-p) & p^2 & p^2 \\ (1-p)(1+p) & 0 & p(1+p) & p^2 \\ 1-p & p(1-p) & p & p^2 \end{pmatrix}.$$

Furthermore, the solution to this recursive equation is as follows:

$$\underline{Q}_{4,N}(p) = [\mathbf{I} - \mathbf{B}(p)]^{-1} [\mathbf{I} - (\mathbf{B}(p))^N] \underline{Q}_{4,1}(p). \quad (\text{A.18})$$

Proof. The outline of proof is the same as the proof for Theorem A.3. Here, $Q_{4,N}^{(010)}(p)$, $Q_{4,N}^{(100)}(p)$ and $Q_{4,N}^{(110)}(p)$ are used as auxiliary functions. The rightmost column patterns and their corresponding term for each of the auxiliary functions are summarized in Table A.2. □

For $M = 3$ and $M = 4$, and a large range of N ($N = 1, 5, 10, 20, 50, 100, 200, 500$), the percolation probabilities are obtained by Theorems A.3 and A.4. Figures A.3 and A.4 draw the resulting percolation probabilities as functions of trap density p .

A.3 Percolation Probability for an $M \times 2$ Network

The case of fixed N ($N = 2$) is actually a special case of the general problem addressed in section A.1. Therefore, the general recursive equation A.2 together with equation A.1 can be used to solve the problem. However, it turns out that, in this special case, using a slightly different approach to obtain the desired recursive equation will simplify the solution. The idea is again to condition the percolation probability over the patterns of the uppermost row and then define an auxiliary function to yield a vector recursion. The auxiliary function

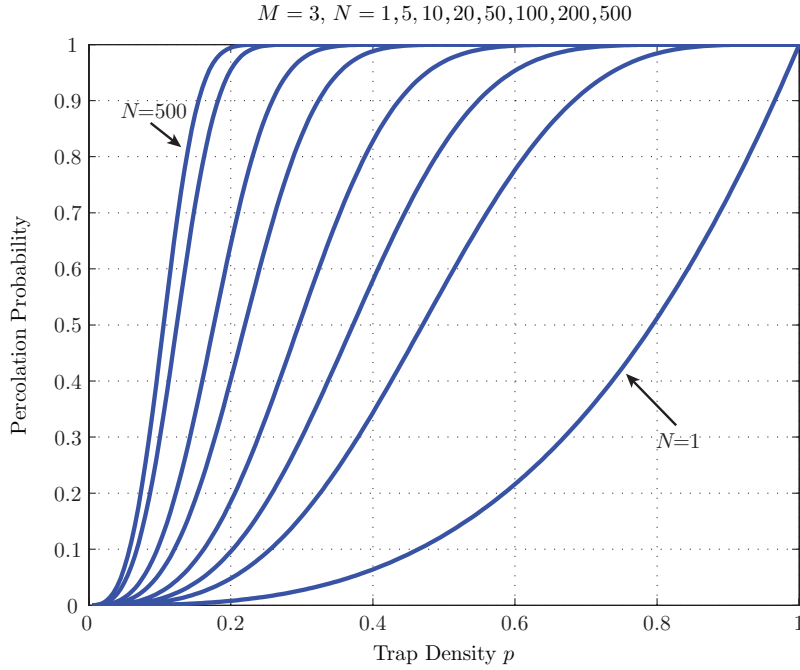


Figure A.3: Percolation probability for $M = 3$ and $N = 1, 5, 10, 20, 50, 100, 200, 500$ obtained by Theorem A.3

here, in contrast to those of section A.2, is defined regarding the uppermost row pattern of the network:

Let b be an N -bit binary pattern. Define $P_{M,N}^b(p)$ to be the probability that an $M \times N$ network (trapped with trap density p) has a path of trapped cells connecting the lowermost row to any cell in the uppermost row whose corresponding bit in b is 1. It is clear that $P_{M,N}^b(p) \leq Q_{M,N}(p)$ for any b , and also, $P_{M,N}^{(11\dots 1)}(p) = Q_{M,N}(p)$.

Using this auxiliary function, the following theorem gives the percolation probability of an M -by-2 network as the first element of the vector $\underline{P}_{M,2}(p) \triangleq [Q_{M,2}(p), P_{M,2}^{(10)}(p)]^T$:

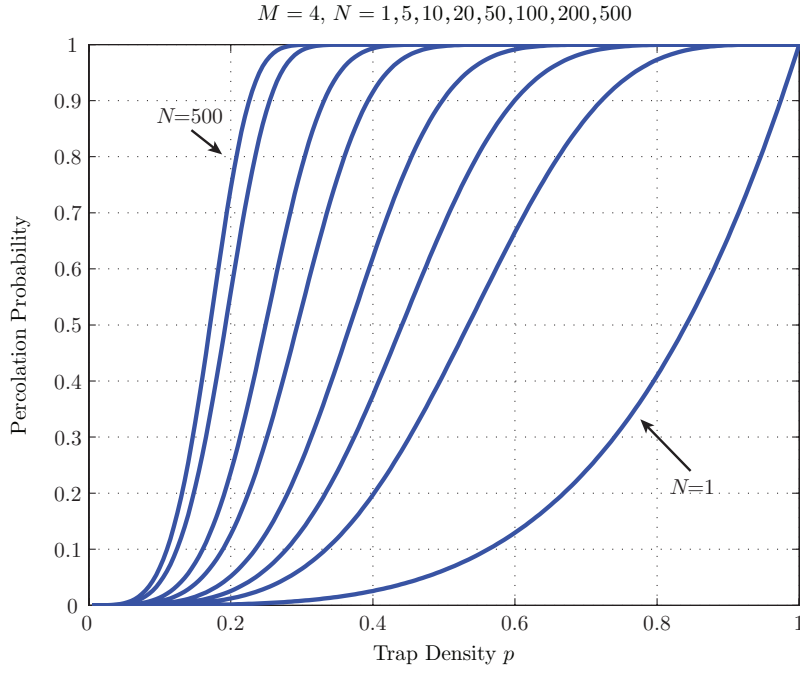


Figure A.4: Percolation probability for $M = 4$ and $N = 1, 5, 10, 20, 50, 100, 200, 500$ obtained by Theorem A.4

Theorem A.5. For any $M > 1$, $Q_{M,2}(p)$ is the solution of the following recursion:

$$\underline{P}_{M,2}(p) = \mathbf{C}(p)\underline{P}_{M-1,2}(p) \quad (\text{A.19})$$

where,

$$\mathbf{C}(p) = \begin{pmatrix} p^2 & 2p(1-p) \\ p^2 & p(1-p) \end{pmatrix},$$

$$\underline{P}_{M,2}(p) = [Q_{M,2}(p), P_{M,2}^{(10)}(p)]^T$$

with the initial condition

$$\underline{P}_{1,2}(p) = [1 - (1-p)^2, p]^T.$$

Therefore,

$$\underline{P}_{M,2}(p) = (\mathbf{C}(p))^{M-1} \underline{P}_{1,2}(p). \quad (\text{A.20})$$

Proof. Note that, conditional on having two trapped cells as the uppermost row of an M -by-2 network, the percolation probability would be equal to the percolation probability of the $(M - 1)$ -by-2 network which has the second row of the original network as its uppermost row. This is, in turn, $Q_{M-1,2}(p)$. Conditional on having only one trapped cell in the uppermost row (either (10) or (01)), the percolation probability is equal to $P_{M-1,2}^{(10)}(p)$ of the mentioned $(M - 1)$ -by-2 network.

For $P_{M,2}^{(10)}(p)$, doing the same conditioning as before, we will have $Q_{M-1,2}(p)$ and $P_{M-1,2}^{(10)}(p)$ for (11) and (10), respectively, and 0 for (01), where, (\cdot) shows the uppermost row pattern on which $P_{M-1,2}^{(10)}(p)$ is conditioned.

Regarding the above observations and arranging the resulting equations in a matrix form, the desired recursion [A.19](#) will be derived. The initial condition is then straightforward to verify. \square

In the following, I will give another approach to percolation probability of an $M \times 2$ network which could be interesting and also instructive: Let $F_{M,N}(k)$ be the number of trapped networks of size $M \times N$ that the number of their trapped cells is k and have “percolation path”. With this definition, the percolation probability can be written as follows:

$$Q_{M,N}(p) = \sum_{k=1}^{MN} F_{M,N}(k) p^k (1-p)^{MN-k}. \quad (\text{A.21})$$

Thus, the problem of finding the percolation probability reduces to the problem of finding $F_{M,N}(k)$ for every $1 \leq k \leq MN$. However, the problem of finding $F_{M,N}(k)$ for an arbitrary pair (M, N) is as hard as the problem of finding the percolation probability

itself. Nevertheless, using some combinatorial strategies and simplifications, a closed-form expression can be found for $F_{M,2}(k)$. The following theorem gives the resulting formula:

Theorem A.6. *For every $M > 0$ and $M \leq k \leq 2M$,*

$$F_{M,2}(k) = \sum_{l=0}^{k-M+1} \binom{k-M+1}{l} \binom{2M-k-1}{l-1} 2^l. \quad (\text{A.22})$$

Proof. Note that every desired network is formed by concatenating elementary patterns of Figure A.5. Figure A.6 illustrates this concatenation for an M -by-2 network. The elementary patterns of type 2 (Figure A.5b) have heights $1 \leq m \leq k - M$. To see why this is true, assume that a concatenation is given containing d patterns of type 1 and l patterns of type 2. The number of trapped cells in type 2 patterns is $M - d$. This together with the fact that the whole number of trapped cells is k imply that $d = k - M$.

Let m_i , $1 \leq i \leq d$, be the number of trapped cells between $i-1$ th and i th type 1 pattern (counting from up to down). Define m_0 (m_{d+1}) to be the number of trapped cells above (below) the first (last) type 1 pattern. Clearly, $0 \leq m_i \leq M - d = 2M - k$. Therefore,

$$F_{M,2}(k) = \sum_{\substack{m_0+m_1+\dots+m_{d+1}=2M-k \\ \forall i, 0 \leq m_i}} \prod_{i=0}^{d+1} 2^{\text{sgn}(m_i)}. \quad (\text{A.23})$$

The function $\text{sgn}(\cdot)$ in (A.23) reflects the fact that each $m_i > 0$ corresponds to a type 2 pattern which contributes with a factor of 2 in the product (according to which pattern of figure A.5b is selected). It follows that the product in (A.23) depends only on the number of nonzero m_i 's. Thus, $F_{M,2}(k)$ can be written as follows:

$$F_{M,2}(k) = \sum_{l=0}^{d+1} \binom{d+1}{l} \binom{2M-k-1}{l-1} 2^l. \quad (\text{A.24})$$

This last equation follows from the fact that there are $\binom{d+1}{l}$ possibilities to select l nonzero m_i 's ($0 \leq l \leq d+1$). If i_0, i_1, \dots, i_{l-1} are indices of the l selected nonzero m_i 's,

then one should find the number of solutions to $m_{i_0} + m_{i_1} + \dots + m_{i_{l-1}} = 2M - k$ with $m_{i_s} > 0$ for all $0 \leq s \leq l - 1$. This is a standard combinatorial problem whose solution is $\binom{2M-k-1}{l-1}$. (A.22) is then immediate by replacing d with $k - M$ in (A.24). \square

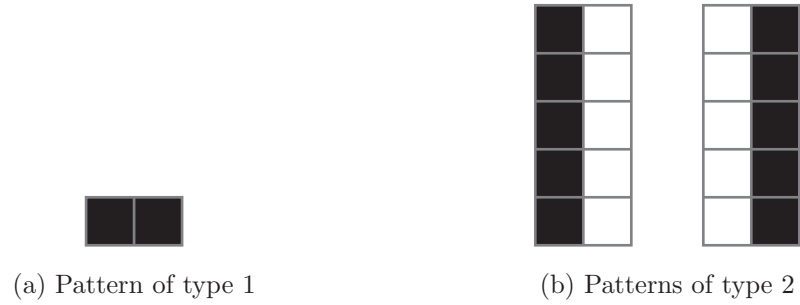


Figure A.5: Elementary patterns

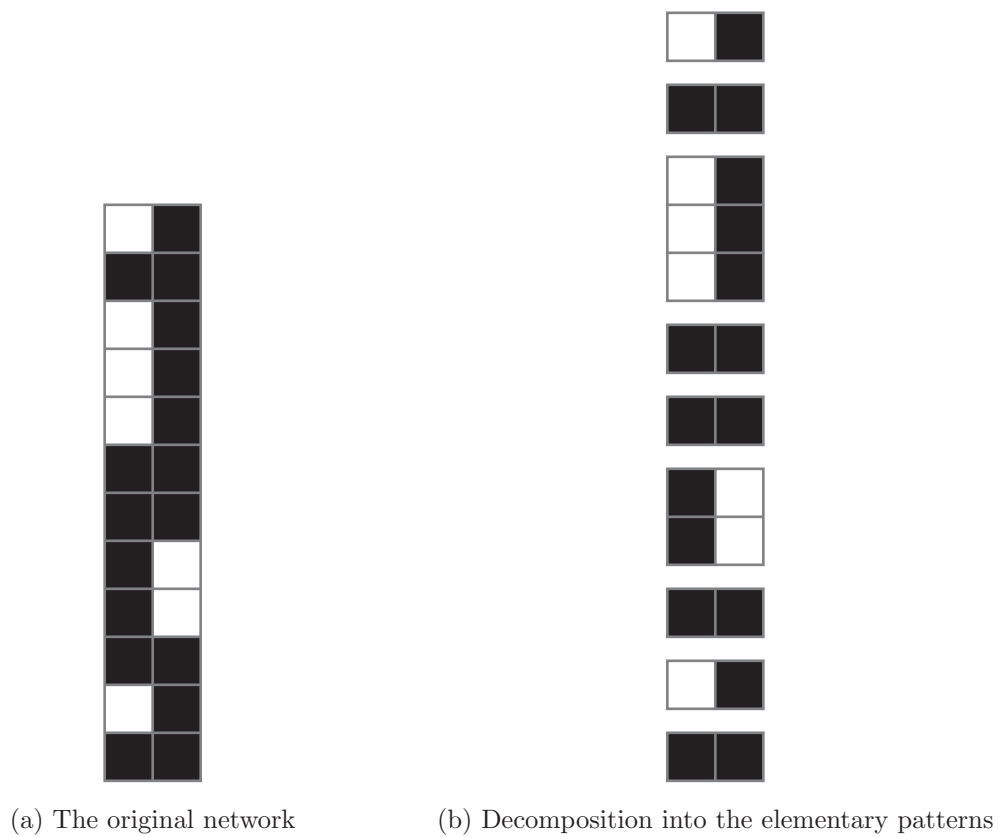


Figure A.6: An example: 12×2 trapped network

Table A.1: The eight possible rightmost column patterns for a $3 \times N$ network and their corresponding terms in calculation of the auxiliary functions

























Rightmost Column Pattern		$Q_{3,N}(p)$	$Q_{3,N}^{(10)}(p)$
	$(1-p)^3 \times$	$Q_{3,N-1}(p)$	$Q_{3,N-1}(p)$
	$p(1-p)^2 \times$	$Q_{3,N-1}(p)$	$Q_{3,N-1}(p)$
	$p(1-p)^2 \times$	$Q_{3,N-1}(p)$	$Q_{3,N-1}^{(10)}(p)$
	$p(1-p)^2 \times$	$Q_{3,N-1}(p)$	$Q_{3,N-1}(p)$
	$p^2(1-p) \times$	$Q_{3,N-1}^{(10)}(p)$	$Q_{3,N-1}^{(10)}(p)$
	$p^2(1-p) \times$	$Q_{3,N-1}(p)$	$Q_{3,N-1}(p)$
	$p^2(1-p) \times$	$Q_{3,N-1}^{(10)}(p)$	1
	$p^3 \times$	1	1

Table A.2: The sixteen possible rightmost column patterns for a $4 \times N$ network and their corresponding terms in calculation of the auxiliary functions

Rightmost Column Pattern	$Q_{4,N}(p)$	$Q_{4,N}^{(010)}(p)$	$Q_{4,N}^{(100)}(p)$	$Q_{4,N}^{(110)}(p)$
	$(1-p)^4 \times$	$Q_{4,N-1}(p)$	$Q_{4,N-1}(p)$	$Q_{4,N-1}(p)$
	$p(1-p)^3 \times$	$Q_{4,N-1}(p)$	$Q_{4,N-1}(p)$	$Q_{4,N-1}(p)$
	$p(1-p)^3 \times$	$Q_{4,N-1}(p)$	$Q_{4,N-1}(p)$	$Q_{4,N-1}^{(100)}(p)$
	$p(1-p)^3 \times$	$Q_{4,N-1}(p)$	$Q_{4,N-1}^{(010)}(p)$	$Q_{4,N-1}^{(010)}(p)$
	$p(1-p)^3 \times$	$Q_{4,N-1}(p)$	$Q_{4,N-1}(p)$	$Q_{4,N-1}(p)$
	$p^2(1-p)^2 \times$	$Q_{4,N-1}^{(100)}(p)$	$Q_{4,N-1}^{(100)}(p)$	$Q_{4,N-1}^{(100)}(p)$
	$p^2(1-p)^2 \times$	$Q_{4,N-1}(p)$	$Q_{4,N-1}^{(010)}(p)$	$Q_{4,N-1}^{(010)}(p)$
	$p^2(1-p)^2 \times$	$Q_{4,N-1}(p)$	$Q_{4,N-1}(p)$	$Q_{4,N-1}(p)$
	$p^2(1-p)^2 \times$	$Q_{4,N-1}(p)$	$Q_{4,N-1}^{(110)}(p)$	$Q_{4,N-1}^{(110)}(p)$
	$p^2(1-p)^2 \times$	$Q_{4,N-1}(p)$	$Q_{4,N-1}(p)$	$Q_{4,N-1}^{(100)}(p)$
	$p^2(1-p)^2 \times$	$Q_{4,N-1}^{(100)}(p)$	1	$Q_{4,N-1}^{(100)}(p)$
	$p^3(1-p) \times$	$Q_{4,N-1}^{(110)}(p)$	$Q_{4,N-1}^{(110)}(p)$	$Q_{4,N-1}^{(110)}(p)$
	$p^3(1-p) \times$	$Q_{4,N-1}^{(100)}(p)$	$Q_{4,N-1}^{(100)}(p)$	$Q_{4,N-1}^{(100)}(p)$
	$p^3(1-p) \times$	$Q_{4,N-1}^{(100)}(p)$	1	$Q_{4,N-1}^{(100)}(p)$
	$p^3(1-p) \times$	$Q_{4,N-1}^{(110)}(p)$	1	1
	$p^4 \times$	1	1	1

Appendix B

Estimation of the Cell Size in the 2-D Percolation Model

In the dissertation, we described the oxide dimensions (width and thickness) based on number of cells. Now, there is a question that what the cell size should be.

As it was explained in chapter 5, the Weibull slope only changes by thickness, and changing the width and the applied stress do not affect it that much. Therefore, one of the best ways to estimate the cell size is by fitting the β -vs- t_{ox} simulation curve to the experiment.

Figures 5.11a and 5.11b show the β -vs- t_{ox} simulation and experimental results, respectively. Both simulation and experimental results express β as a linear function of thickness.

Fitting the results to a linear function, β_{sim} (*i.e.*, the Weibull shape factor from simulation) can be expressed as follows:

$$\beta_{sim} \simeq 0.6413 \times \frac{t_{ox}}{a_0} + 1.2373$$

where, a_0 is the cell size. t_{ox}/a_0 is equal to the number of cells of thickness.

Experimental data, on the other hand, fits to :

$$\beta \simeq 0.5478 \times t_{ox} + 0.2083.$$

Therefore,

$$a_0 \simeq 0.6413/0.5478 = 1.17 \text{ nm}.$$

Appendix C

MATLAB Simulation Codes

The major MATLAB simulation codes are included in this Appendix. The codes are categorized based on their related usage in the thesis.

C.1 2-D Network Simulation

- `function` percolate = check_percol(cluster)
% Leila Rezaee, 2005
% This function checks if the input matrix has a vertical path or not.

[N,M] = size(cluster);
Row1 = cluster(1,:);
Row2 = cluster(N,:);
percolate = length(setdiff(intersect(Row1,Row2),[0]))>0;
- `function` Prob = Cal_Perc_Prob(N,M,P)
% Leila Rezaee, 2005
% This function calculates the percolation-probability for a network with
% size = [N, M] and the defect density =P. The function check_percol is
% called to test the percolation.

```

f=zeros(N,M);
cluster=zeros(N,M);
vv=0;
for i=1:200
    cluster=bwlabel( (rand(N,M)<=P),4);
    percolate=check_percol(cluster);
    vv=vv+percolate;
end;
Prob=vv/200;

```

C.2 Resistor Network Conductance

- ```

function G = Eq_Resistor_Network(Net,R1,R2)
% Leila Rezaee, 2006
% This function returns the resistor network corresponding to trapped
% network Net. R1 and R2 : trap and non-trap resistances

% NOTE: elements of Net are called 'cell'

[M,N] = size(Net);
G1 = 1/R1;
G2 = 1/R2;
K = 1+(M-1)*N; % number of nodes in the resistor network (all the
 % uppermost cells are connected to eachother and to
 % a current voltage source)
index = reshape(2:K,M-1,N);
index = [ones(1,N);index];

% 'index' is an M-by-N matrix containing voltage index of cells
G = zeros(K);
for i = 2:M-1
 for j = 2:N-1

```

```

G(index(i,j),index(i-1,j)) = -((G1-G2)*Net(i,j)*Net(i-1,j)+G2);
G(index(i,j),index(i+1,j)) = -((G1-G2)*Net(i,j)*Net(i+1,j)+G2);
G(index(i,j),index(i,j-1)) = -((G1-G2)*Net(i,j)*Net(i,j-1)+G2);
G(index(i,j),index(i,j+1)) = -((G1-G2)*Net(i,j)*Net(i,j+1)+G2);
G(index(i,j),index(i,j)) = -(G(index(i,j),index(i-1,j))+ ...
 G(index(i,j),index(i+1,j))+G(index(i,j),index(i,j-1))+ ...
 G(index(i,j),index(i,j+1)));
end
end
for i = 2:M-1
G(index(i,1),index(i-1,1)) = -((G1-G2)*Net(i,1)*Net(i-1,1)+G2);
G(index(i,1),index(i+1,1)) = -((G1-G2)*Net(i,1)*Net(i+1,1)+G2);
G(index(i,1),index(i,2)) = -((G1-G2)*Net(i,1)*Net(i,2)+G2);
G(index(i,1),index(i,1)) = -(G(index(i,1),index(i-1,1))+ ...
 G(index(i,1),index(i+1,1))+G(index(i,1),index(i,2)));

G(index(i,N),index(i-1,N)) = -((G1-G2)*Net(i,N)*Net(i-1,N)+G2);
G(index(i,N),index(i+1,N)) = -((G1-G2)*Net(i,N)*Net(i+1,N)+G2);
G(index(i,N),index(i,N-1)) = -((G1-G2)*Net(i,N)*Net(i,N-1)+G2);
G(index(i,N),index(i,N)) = -(G(index(i,N),index(i-1,N))+ ...
 G(index(i,N),index(i+1,N))+G(index(i,N),index(i,N-1)));
end
for j = 2:N-1
G(index(M,j),index(M-1,j)) = -((G1-G2)*Net(M,j)*Net(M-1,j)+G2);
G(index(M,j),index(M,j-1)) = -((G1-G2)*Net(M,j)*Net(M,j-1)+G2);
G(index(M,j),index(M,j+1)) = -((G1-G2)*Net(M,j)*Net(M,j+1)+G2);
G(index(M,j),index(M,j)) = -(G(index(M,j),index(M-1,j))+ ...
 G(index(M,j),index(M,j-1))+G(index(M,j),index(M,j+1)))+...
 (G1-G2)*Net(M,j)+G2;
end
G(index(M,1),index(M-1,1)) = -((G1-G2)*Net(M,1)*Net(M-1,1)+G2);
G(index(M,1),index(M,2)) = -((G1-G2)*Net(M,1)*Net(M,2)+G2);
G(index(M,1),index(M,1)) = -(G(index(M,1),index(M,2))+ ...
 G(index(M,1),index(M-1,1)))+(G1-G2)*Net(M,1)+G2;

```

```

G(index(M,N),index(M-1,N)) = -((G1-G2)*Net(M,N)*Net(M-1,N)+G2);
G(index(M,N),index(M,N-1)) = -((G1-G2)*Net(M,N)*Net(M,N-1)+G2);
G(index(M,N),index(M,N)) = -(G(index(M,N),index(M,N-1))+ ...
 G(index(M,N),index(M-1,N)))+(G1-G2)*Net(M,N)+G2;

for j = 1:N
 G(1,index(2,j)) = -((G1-G2)*Net(1,j)*Net(2,j)+G2);
 G(1,1) = G(1,1)-G(1,index(2,j));
end

```

### C.3 Parallel-Series Network Model

- ```

function y = conduction_cal(cluster)
% Leila Rezaee, 2006
% This function calculates the conductance of an input lattice
% Using the Parallel-Series Network model.
% Cluster : the input network
% Lattice_Conductance : the conductance of the lattice
[N,M] = size(cluster);
r1 = cluster(1,:); % The top row of the network.
r2 = cluster(N,:); % The bottom row of the network.
patt = setdiff(intersect(r1,r2),[0]);
number_of_paths=length(patt); % The number of percolating paths
                                % inside the network.

cluster_ref=zeros(N,M);
for i=1:number_of_paths
    cluster_ref= (cluster==patt(i))|cluster_ref;
end
cluster_ref=cluster.*cluster_ref;

for k=1:number_of_paths
    cluster_to_check=patt(k);

```

```

for i=1:N
    horizontal_resistor_count=0;
    for j=1:M
        if (cluster_ref(i,j)==cluster_to_check)
            horizontal_resistor_count=horizontal_resistor_count+1;
        end;
    end;
    res_count(k,i)=horizontal_resistor_count ;
end;
for i=1:N-1
    contact_count=0;
    for j=1:M
        if ((cluster_ref(i,j)==cluster_to_check) && ...
            (cluster_ref(i+1,j)==cluster_to_check))
            contact_count=contact_count+1;
        end
    end;
    con_count(k,i)=contact_count;
end;

contact_res=1000*10^(3);
cell_res=10^(4);
conductivity=0;
for l=1:number_of_paths
    RR=0;
    for i=1:N-1
        RR=RR + cell_res/res_count(l,i)+ contact_res/con_count(l,i);
    end;
    for i=N:N
        RR=RR + cell_res/res_count(l,i);
    end;
    RES(l)=RR;
end

```



```

S=0;
for l=1:number_of_paths
    S=S+1/RES(l);
end;
Lattice_Conductance = S;
return

```

- `function y = resistor_count(cluster)`
% Leila Rezaee, 2005
% This function calculates the conductance of the input network.

```

[N,M] = size(cluster);
r1 = cluster(1,:);
r2 = cluster(N,:);
path = setdiff(intersect(r1,r2),[0]);
y = 0;
for i = 1:length(path)
    cluster_path = cluster==path(i);
    cluster_path = [cluster_path(1,:);cluster_path;cluster_path(N,:)];
    cluster_path = filter2([1;1;1],cluster_path);
    cluster_path = cluster_path==3;
    y1 = sum(cluster_path(2:N+1,:),2);
    y1 = y1(find(y1~=0));
    y1 = 1/sum(1./y1);
    y = y+y1;
end

```

C.4 TDDB Simulation

- `function TBD = CVSS_statistics(N,M,P,sample_number,measuring_time)`
% Leila Rezaee, 2006
%This function computes the Time to breakdown statistics; The size of the
%samples is (N,M). P = The applied stress = P. sample_number = Number of

```

%samples that are tested. The test is done over the measuring time = 200.
%F = Trapped Network. TBD = time-to-breakdown.
%
%note : the post-breakdown conductance is not calculated in this function.

F=zeros(N,M);
cluster=zeros(N,M);
TBD=zeros(sample_number,1);
time = [1:measuring_time];
for sample=1:sample_number
    F = zeros(N,M);
    for counter=1:measuring_time
        Test = (rand(N,M)<=P);% P = applied stress
        F = F|Test; %modelimng the accumulation of defects
        cluster=bwlabel(F,4);
        percolate=check_percol(cluster);
        if percolate==1
            if TBD(sample)>=time(counter)
                TBD(sample) = time(counter);
            end;
        else
            TBD(sample)=measuring_time;
        end;
    end;
end;
end;

```

C.5 Markov Simulation

- `function [MarkovTrans,NetMat,NTrap] = MarkovGen(M,N,p,q,NetMat)`
 % Leila Rezaee, 2007
 % The inputs are:
 % p : upward transition probability
 % q : horizontal transition probability

```

% NetMat : input trapped network (binary matrix)
% M & N : NetMat dimensions
%
% The outputs are:
% MarkovTrans : Markov Chain transition matrix
% NetMat      : output Network matrix (clustered)
% NTrap      : number of trapped states in the resulting Markov chain
%              (the first) row cells and those who are in the same
%              cluster with any of these cells are considered a the
%              trap state #1
% This function gets the trapped network matrix as input and
% constructs the Markov chain corresponding to this network
% using the input transition probabilities.

NetMat = [ones(1,N);NetMat];
NetMat = bwlabel(NetMat,4);
NetMat = NetMat(2:M+1,:);
NetMat(1,:) = 1;

NMax = max(max(NetMat)); %Number of trap regions
NTrap = NMax;

% *****numbering the Markov chain states
for i = 1:M
    for j = 1:N
        if NetMat(i,j)==0
            NMax = NMax+1;
            NetMat(i,j) = NMax;
        end
    end
end

% NMax : number of Markov chain states

```

```

MarkovTrans = zeros(NMax);%sym(zeros(NMax));

for i = NTrap+1:NMax
    [x,y] = find(NetMat==i);
    MarkovTrans(i,NetMat(x-1,y)) = p;
    if 1<y & y<N
        MarkovTrans(i,NetMat(x,y+1)) = q;
        MarkovTrans(i,NetMat(x,y-1)) = q;
    elseif y==1
        MarkovTrans(i,NetMat(x,y+1)) = 2*q;
    else
        MarkovTrans(i,NetMat(x,y-1)) = 2*q;
    end
end
end
MarkovTrans(1:NTrap,1:NTrap) = eye(NTrap); % Trap states (There assumed
                                           % to be no outgoing transitions
                                           % from the trap states)

% ***** The initial state assignment
temp = zeros(1,NMax);
temp1 = unique(NetMat(M,:));
temp(temp1) = 1/length(temp1); % The initial state has transition
                               % only to trap states of the last row
MarkovTrans = [MarkovTrans;temp];
MarkovTrans = [MarkovTrans,zeros(NMax+1,1)];

• function ap = Absorption_Prob(P,A)
% Leila Rezaee, 2007
% This function gets the markov chain transition matrix (P) and
% a subset of states (A) and calculates absorption probabilities of
% states belonging to A

absorbing_states = find(diag(P)==1); % absorbing states in P
A1 = setdiff(absorbing_states(:)',A); % absorbing states excluding A

```

```

index = setdiff(1:size(P,1),[A,A1]);    %
P_hat = P(index,index);                %
u = sum(P(index,A),2);
ap = (eye(size(P_hat,1))-P_hat)\u;

• function I = Ave_Current_Detrap(M,N,p,q,pd,D,T)
% Leila Rezaee, 2007
% The inputs are:
%     M & N   : network dimensions
%     p       : upward transition probability
%     q       : horizontal transition probability
%     pd      : detrap density
%     D       : trap density
%     T       : maximum simulation steps
%
% The output is:
%     I       : average current (absorption probability)

% This function uses accumulation of defects algorithm together
% with alternate trap/detrap approach to compute the absorption
% probability of the network with the input parameters

NetMat = zeros(M,N);
k = 0;
d=1;
for i=1:d+1:T
    for j=1:d
        if k<M*N
            temp = rand(M,N);
            temp = temp<D;
            NetMat = NetMat|temp;
            k = sum(sum(NetMat));
            k1(i+j-1) = k/(M*N);
        end
    end
end

```

```

        [P,NetMat1,NTrap] = MarkovGen(M,N,p,q,NetMat);
        h = Absorption_Prob(P,1);
        I(i+j-1) = h(length(h));
    end;
    if k<M*N
        temp = rand(M,N);
        temp = temp>pd*(1-I(i+j-1));
        NetMat = NetMat&temp;
        k = sum(sum(NetMat));
        k1(i+d) = k/(M*N);
    end
    [P,NetMat1,NTrap] = MarkovGen(M,N,p,q,NetMat);
    h = Absorption_Prob(P,1);
    I(i+d) = h(length(h));
end

```

C.6 Analytical Formula Extraction

- `function k = G.intersect(i,j,n)`
% Leila Rezaee, 2008
% This function puts the n-bit binary patterns of i and j
% on top of eachother and constructs the n-bit binary pattern
% k whose 1-bits are those in i which are connected to at least
% one 1-bit in j (in 4-connection sense).

```

A = bwlabel([de2bi(j,n);de2bi(i,n)],4);
B = setdiff(A(2,:),A(1,:));
C = A(2,:);
for i = 1:length(B)
    C(find(C==B(i))) = 0;
end
k = bi2de(C>0);

```

```

• function [Fout,Pout] = Pr_trap(m,n,p,Fin)
  % Leila Rezaee, 2008
  % m & n : network size
  % p : cell trap density
  % Fin : (m-1)-row Pattern-Breakdown-Distribution matrix
  %
  % Fout : m-row Pattern-Breakdown-Distribution matrix
  % Pout : breakdown probability for the m*n network
  %
  % The m-row Pattern-Breakdown-Distribution matrix is a
  % (2^n)-by-(m*n) matrix whose ij-th element is the
  % number of m*n trapped networks that have :
  %     1- The n-bit binary number corresponding to i
  %     as their first row pattern.
  %     2- j trapped cells
  %     3- a path between their uppermost and lowermost rows

  Fout = zeros(2^n,m*n);
  L = de2bi(0:2^n-1);
  L = sum(L',1);
  if m==2
    for i = 0:2^n-1
      for k=1:2*n
        for j = max(1,k-n):min(L(i+1),k-L(i+1))
          Fout(i+1,k) = Fout(i+1,k)+nchoosek(L(i+1),j)* ...
            nchoosek(n-L(i+1),k-L(i+1)-j);
        end
      end
    end
  else
    for i = 0:2^n-1
      for k = 1:m*n
        for j = 0:2^n-1
          G = G_intersect(j,i,n);

```

```

        ktemp = k-L(i+1)-L(j+1)+L(G+1);
        if 0<ktemp & ktemp<=(m-1)*n
            Fout(i+1,k) = Fout(i+1,k)+Fin(G+1,ktemp);
        end
    end
end
end
end
end

```

```

Pout = 0;
temp = sum(Fout);
for k = 1:m*n
    Pout = Pout+temp(k)*p^k*(1-p)^(m*n-k);
end
Pout = sort(factor(simple(Pout)));
vF = sprintf('F_%d_%d',m,n);
vP = sprintf('P_%d_%d',m,n);
eval([vF ' = Fout;']);
eval([vP ' = Pout;']);
filename = sprintf('A_%d_%d.mat',m,n);
eval(['save ' filename ' ' vF ' ' vP ';'']);

```


Bibliography

- [1] J. E. Lilienfeld, *Method and apparatus for controlling electric currents*. U.S. Patent 1 745 175, 1930.
- [2] D. Kahng and M. M. Atalla, “Silicon-silicon dioxide field induced surface devices,” *IRE Solid-State Device Res. Conf., Pittsburgh, PA*, June 1960.
- [3] D. J. Frank, R. H. Dennard, E. Nowak, P. M. Solomon, Y. Taur, and H.-S. P. Wong, “Device scaling limits of Si MOSFET’s and their application dependencies,” *Proceedings of the IEEE*, vol. 89, no. 3, pp. 259–288, March 2001.
- [4] H. Iwai, “Future of silicon integrated circuit technology,” *Second International Conference on Industrial and Information Systems, ICIIIS 2007, Sri Lanka*, pp. 571–576, August 2007.
- [5] H. Wong and H. Iwai, “On the scaling issues and high- K replacement of ultrathin gate dielectrics for nanoscale MOS transistors,” *Microelectron. Eng.*, vol. 83, no. 10, pp. 1867–1904, October 2006.
- [6] P. M. Zeitzoff, J. Hutchby, and H. Huff, “MOSFET and front-end process integration: Scaling trends, challenges, and potential solutions through the end of the roadmap,”

- International Journal of High-Speed Electronics and Systems*, vol. 12, no. 2, pp. 267–293, 2002.
- [7] P. M. Zeitzoff, “Circuit, MOSFET, and front end process integration trends and challenges for the 180 nm and below technology generations: An International Technology Roadmap for Semiconductors perspective,” *in: Proc. 6th International Conference on Solid-State and Integrated-Circuit Technology*, vol. 1, pp. 23–28, October 2001.
- [8] W. Haensch, E. J. Nowak, R. H. Dennard, P. M. Solomon, A. Bryant, O. H. Dokumaci, A. Kumar, X. Wang, J. B. Johnson, and M. V. Fischetti, “Silicon cmos devices beyond scaling,” *IBM J. RES. DEV.*, vol. 50, no. 4/5, pp. 339–362, July/September 2006.
- [9] S. Krishnan, S. V. Garimella, G. M. Chrysler, and R. V. Mahajan, “Towards a thermal Moores law,” *IEEE Trans. Advanced Packaging*, vol. 30, no. 3, pp. 462–474, August 2007.
- [10] J. D. Plummer and P. B. Griffin, “Material and process limits in silicon VLSI technology,” *Proceedings of the IEEE*, vol. 89, no. 3, pp. 240–258, March 2001.
- [11] G. E. Moore, *Intel-Memories and the Microprocessor*. Daedalus, Spring 1996, vol. 125, no. 2.
- [12] —, “Cramming more components onto integrated circuits,” *Electronics*, vol. 38, pp. 114–116, April 1965.
- [13] J.-C. Boudenot, “From transistor to nanotube,” *Comptes Rendus. Physique*, vol. 9, no. 1, pp. 41–52, January 2008.

- [14] M. Wu, Y. I. Alivov, and H. Morko, "High- K dielectrics and advanced channel concepts for Si MOSFET," *J. Mater. Sci.: Mater. Electron.*, vol. 19, pp. 915–951, May 2008.
- [15] S. et al., "International Technology Roadmap for Semiconductors, 2007 Edition, <http://www.itrs.net/Links/2007ITRS/Home2007.htm>."
- [16] H. Iwai, "Future semiconductor manufacturing - challenges and opportunities," *in: Proc. IEEE IEDM Tech. Dig.*, pp. 11 – 16, December 2004.
- [17] "<http://www.itrs.net>."
- [18] R. F. Pease and S. Y. Chou, "Lithography and other patterning techniques for future electronics," *Proceedings of IEEE*, vol. 96, no. 2, p. 248, February 2008.
- [19] W. M. Arden, "The international technology roadmap for semiconductors Perspectives and challenges for the next 15 years," *Current Opinion in Solid State and Materials Science*, vol. 6, no. 5, pp. 371–377, October 2002.
- [20] R. Chau, J. Kavalieros, B. Doyle, A. Murthy, N. Paulsen, D. Lionberger, D. Barlage, R. Arghavani, B. Roberds, and M. Doczy, "A 50nm depleted-substrate cmos transistor," *in: Proc. IEEE IEDM Tech. Dig.*, pp. 621–624, December 2001.
- [21] T. Yoshitomi, M. Saito, T. Ohguro, M. Ono, H. S. Momose, and H. Iwai, "Silicided silicon-sidewall source and drain (S^4D) structure for high-performance 75 nm gate length pMOSFETs," *in: Proc. Symp. VLSI Tech. Dig.*, pp. 11–12, June 1995.
- [22] T. Yoshitomi, M. Saito, T. Ohguro, M. Ono, H. S. Momose, E. Morifuji, T. Morimoto, Y. Katsumata, and H. Iwai, "High performance of silicided siliconsidewall source and

- drain (S^4D) structure,” *IEEE Trans. Electron. Devices*, vol. 45, no. 6, pp. 1295–1299, June 1998.
- [23] I. Aiba, Y. Sasaki, K. Okashita, H. Tamura, Y. Fukagawa, K. Tsutsui, H. Ito, K. Kakushima, B. Mizuno, and H. Iwai, “Feasibility study of plasma doping on Si substrates with photo-resist patterns,” *Intl Workshop on Junction Technology(IWJT)*, pp. 75–76, June 2005.
- [24] B. L. Yang, E. C. Jonesa, N. W. Cheung, J. Shaob, H. Wongc, and Y. C. Chengd, “N⁺P ultra-shallow junction on silicon by immersion ion implantation,” *Microelectron. Reliab.*, vol. 38, no. 19, pp. 1489–1494, September 1998.
- [25] Y. Sasaki, C. G. Jin, H. Tamura, B. Misuno, R. Higaki, T. Satoh, K. Majima, H. Sauddin, K. Takagi, S. Ohmi, K. Tsutsui, and H. Iwai, “B₂H₆ plasma doping with insitu he pre-amorphization,” *in: Proc. Symp. VLSI Tech. Dig.*, pp. 180–181, June 2004.
- [26] T. Iijima, A. Nishiyama, Y. Ushiku, T. Ohguro, I. Kunishima, K. Suguro, and H. Iwai, “A novel selective Ni₃Si contact plug technique for deep-submicron ULSIs,” *in: Proc. Symp. VLSI Tech. Dig.*, pp. 70–71, June 1992.
- [27] T. Morimoto, H. S. Momose, T. Inuma, I. Kunishima, K. Suguro, H. Okana, I. Katakabe, H. Nakajima, M. Tsuchiaki, M. Ono, Y. Katsumata, and H. Iwai, “A NiSi salicide technology for advanced logic devices,” *in: Proc. IEEE IEDM Tech. Dig.*, pp. 653–656, December 1991.
- [28] S. Takagi, T. Mizuno, T. Tezuka, N. Sugiyama, T. Numata, K. Usuda, Y. Moriyama, S. Nakaharai, J. Koga, A. Tanabe, N. Hirashita, and T. Maeda, “Channel structure

- design, fabrication and carrier transport properties of strained-Si/SiGe-on-insulator (strained-SOI) MOSFETs,” *in: Proc. IEEE IEDM Tech. Dig.*, pp. 57–60, December 2003.
- [29] J. Welser, J. L. Hoyt, , and J. F. Gibbons, “NMOS and PMOS transistors fabricated in strained silicon/relaxed silicon-germanium structures,” *in: Proc. IEEE IEDM Tech. Dig.*, pp. 1000–1002, December 1992.
- [30] K. Ismail, S. F. Nelson, J. O. Chu, , and B. S. Meyerson, “Electron transport properties of Si/SiGe heterostructures: Measurements and device implications,” *Appl. Phys. Lett.*, vol. 63, no. 5, pp. 660–662, August 1993.
- [31] J. Cai, K. Rim, A. Bryant, K. Jenkins, C. Ouyang, D. Singh, Z. Ren, K. Lee, H. Yin, J. Hergenrother, T. K. aand A. Kumar, X. Wang, S. Bedell, A. Reznicek, H. H. Hovel, D. Sadana, D. Uriarte, R. Mitchell, J. Ott, D. Mocuta, P. O’Neil, A. Mocuta, E. Leobandung, R. Miller, W. Haensch, and M. Leong, “Performance comparison and channel length scaling of strained Si FETs on SiGe-on-insulator (SGOI),” *in: Proc. IEEE IEDM Tech. Dig.*, pp. 165–168, December 2004.
- [32] S. Monfray, D. Chanemougame, S. Borel, A. Talbot, F. Leverd, N. Planes, D. Delille, D. Dutartre, R. Palla, Y. Morand, S. Descombes, M.-P. Samson, N. Vulliet, T. Sparks, A. Vandooren, and T. Skotnicki, “SON (silicon-on-nothing) technological CMOS platform: Highly performant devices and SRAM Cells,” *in: Proc. IEEE IEDM Tech. Dig.*, pp. 635–638, December 2004.
- [33] R. Tsuchiya, M. Horiuchi, S. Kimura, M. Yamaoka, T. Kawahara, S. Maegawa, T. Ipposhi, Y. Ohji, and H. Matsuoka, “Silicon on thin box: A new paradigm of the

- CMOSFET for low-power and high performance application featuring wide-range back-bias control,” *in: Proc. IEEE IEDM Tech. Dig.*, pp. 631–634, December 2004.
- [34] D. Hisamoto, W.-C. Lee, J. Kedzierski, H. Takeuchi, K. Asano, C. Kuo, E. Anderson, T.-J. King, J. Bokor, and H. Chenming, “Finfet-a self-aligned double-gate MOSFET scalable to 20 nm,” *IEEE Trans. Electron. devices*, vol. 47, no. 12, pp. 2320–2325, December 2000.
- [35] H.-S. Wong, D. Frank, , and P. Solomon, “Device design considerations for double-gate, ground-plane, and single-gated ultrathin SOI MOSFETs at the 25 nm channel length generation,” *in: Proc. IEEE IEDM Tech. Dig.*, pp. 407–410, December 1998.
- [36] K. Suzuki, T. Tanaka, Y. Tosaka, H. Horie, and Y. Arimoto, “Scaling theory for double-gate SOI MOSFETs,” *IEEE Trans. Electron. Devices*, vol. 40, no. 12, pp. 2326–2329, December 1993.
- [37] D. Hisamoto, T. Kaga, and E. Takeda, “Impact of vertical SOI “DELTA” structure on planar device technology,” *IEEE Trans. Electron. Devices*, vol. 38, no. 6, pp. 1419–1424, June 1991.
- [38] G. D. Wilk, R. M. Wallace, , and J. M. Anthony, “High-k gate dielectrics: current status and materials properties considerations,” *J. Appl. Phys.*, vol. 89, no. 10, pp. 5243–5275, May 2001.
- [39] S. Ohmi, C. Kobayashi, E. Tokumitsu, H. Ishiwara, and H. Iwai, “Low leakage La_2O_3 gate insulator film with EOTs of 0.8-1.2 nm,” *Int. Conf. Solid State Devices and Materials (SSDM), Ext. Abs.*, pp. 496–497, September 2001.

- [40] H. Iwai, S. Ohmi, and S. Akama, "Advanced gate dielectric materials for sub-100 nm CMOS," *in: Proc. IEEE IEDM Tech. Dig.*, pp. 625–628, December 2002.
- [41] B. H. Lee, L. Kang, W. J. Qi, R. Nieh, Y. Jeon, K. Onishi, and J. C. Lee, "Ultrathin hafnium oxide with low leakage and excellent reliability for alternative gate dielectric application," *in: Proc. IEEE IEDM Tech. Dig.*, pp. 133–136, December 1999.
- [42] H. Wong, K. L. Ng, N. Zhan, M. C. Poon, and C. W. Kok, "Interface bonding structure of hafnium oxide prepared by direct sputtering of hafnium in oxygen," *J. Vac. Sci. Technol. B*, vol. 22, no. 3, pp. 1094–1100, May 2004.
- [43] J. K. Schaeffer, C. Capasso, L. R. C. Fonseca, S. Samavedam, D. Gilmer, Y. Liang, S. Kalpat, B. Adetutu, H.-H. Tseng, Y. Shiho, A. Demkov, R. Hegde, W. Taylor, R. Gregory, J. Jiang, E. Luckowski, M. Raymond, K. Moore, D. Triyoso, D. Roan, B. W. Jr., and P. Tobin, "Challenges for the integration of metal gate electrodes," *in: Proc. IEEE IEDM Tech. Dig.*, pp. 287–290, December 2004.
- [44] S. Bae, W. Bai, H. Wen, S. Mathew, L. K. Bera, N. Balasubramanian, N. Yamada, M. M. F. Li, and D. L. Kwong, "Laminated metal gate electrode with tunable work function for advanced CMOS," *in: Proc. Symp. VLSI Tech. Dig.*, pp. 188–189, June 2004.
- [45] S. Nitta, S. Purushothaman, S. Smith, M. Krishnan, D. Canaperi, T. Dalton, W. Volksen, R. D. Miller, B. Herbst, C. Hu, E. Liniger, J. Lloyd, M. Lane, D. L. Rath, M. Colburn, and L. Gignac, "Successful dual damascene integration of extreme low-k materials ($k < 2.0$) using a novel gap fill based integration scheme," *in: Proc. IEEE IEDM Tech. Dig.*, pp. 321–324, December 2004.

- [46] H. Miyajima, K. Watanabe, K. Fujita, S. Ito, K. Tabuchi, T. Shimayama, K. Akiyama, T. Hachiya, K. Higashi, N. Nakamura, A. Kajital, N. Matsunagal, Y. Enomoto, R. Kanamura, M. Inohara, K. Honda, H. Kamijo, R. Nakata, H. Yano, N. Hayasaka, T. Hasegawa, S. Kadomural, H. Shibata, and T. Yoda, "Challenge of low-k materials for 130, 90, 65 nm node interconnect technology and beyond," *in: Proc. IEEE IEDM Tech. Dig.*, pp. 329–332, December 2004.
- [47] J. H. Stathis, "Physical and predictive models of ultrathin oxide reliability in CMOS devices and circuits," *IEEE Trans. Device and Materials Reliability*, vol. 1, no. 1, pp. 43–59, March 2001.
- [48] J. W. McPherson and H. C. Mogul, "Underlying physics of the Thermochemical E model in describing low-field time-dependent dielectric breakdown in SiO₂ thin films," *J. Appl. Phys.*, vol. 84, no. 3, pp. 1513–1523, August 1998.
- [49] I. C. Chen, S. Holland, and C. Hu, "A quantitative physical model for time-dependent breakdown in sio," *in: Proc. Int. Reliab. Phys. Symp.(IRSP)*, vol. 23, pp. 24–27, April 1985.
- [50] I. C. Chen, S. E. Holland, K. K. Young, C. Chang, and C. Hu, "Substrate hole current and oxide breakdown," *Appl. Phys. Lett.*, vol. 49, no. 11, pp. 669–671, September 1986.
- [51] K. F. Schuegraf and C. Hu, "Hole injection SiO₂ breakdown model for very low voltage lifetime extrapolation," *IEEE Trans. Electron. Devices*, vol. 41, no. 5, pp. 761–767, May 1994.

- [52] R. E. Stahlbush and E. Cartier, "Interface defect formation in MOSFETs by atomic hydrogen exposure," *IEEE Trans. Nucl. Sci.*, vol. 41, no. 6, pp. 1844–1853, December 1994.
- [53] L. do Thanh and P. Balk, "Elimination and generation of Si/SiO₂ interface traps by low temperature hydrogen annealing," *J. Electrochem. Soc.*, vol. 135, no. 7, pp. 1797–1801, July 1988.
- [54] E. Cartier and J. H. Stathis, "Atomic hydrogen-induced degradation of the Si/SiO₂ structure," *Microelectron. Eng.*, vol. 28, no. 1–4, pp. 3–10, June 1995.
- [55] J. H. Stathis and E. Cartier, "Atomic hydrogen reactions with p centers at the (100) Si/SiO₂ interface," *Phys. Rev. Lett.*, vol. 72, no. 17, pp. 2745–2748, April 1994.
- [56] E. Cartier, J. H. Stathis, and D. A. Buchanan, "Passivation and depassivation of silicon dangling bonds at the Si/SiO₂ interface by atomic hydrogen," *Appl. Phys. Lett.*, vol. 63, no. 11, pp. 1510–1512, September 1993.
- [57] J. S. Suehle, "Ultrathin gate oxide reliability: Physical models, statistics, and characterization," *IEEE Trans. Electron. Devices*, vol. 49, no. 6, pp. 958–971, June 2002.
- [58] J. H. Stathis, "Reliability limits for the gate insulator in CMOS technology," *IBM J. Res. Dev.*, vol. 46, no. 2–3, pp. 265–286, March-May 2002.
- [59] T. C. Shen, C. Wang, G. C. Abeln, J. R. Tucker, J. W. Lyding, P. Avouris, , and R. E. Walkup, "Atomic-scale desorption through electronic and vibrational excitation mechanisms," *Science*, vol. 268, no. 5217, pp. 1590–1592, June 1995.

- [60] K. Hess, I. C. Kizilyalli, and J. W. Lyding, "The giant isotope effect in hydrogen desorption and CMOS lifetime," *IEEE Trans. Electron. Devices*, vol. 3, no. 1-3, pp. 1–7, October 1998.
- [61] C. H. Lin, F. Yuan, B. C. Hsu, and C. W. Liu, "Isotope effect of hydrogen release in metal/oxide/n-silicon tunneling diodes," *Solid-State Electron.*, vol. 47, no. 6, pp. 1123–1126, June 2003.
- [62] J. Wu, E. Rosenbaum, B. MacDonald, E. Li, J. Tao, B. Tracy, and P. Fang, "Anode hole injection versus hydrogen release: The mechanism for gate oxide breakdown," *in: Proc. Int. Reliab. Phys. Symp.(IRSP)*, vol. 38, pp. 27–32, April 2000.
- [63] Y. Mitani, H. Satake, H. Ito, and A. Toriumi, "Highly reliable gate oxide under FowlerNordheim electron injection by deuterium pyrogenic oxidation and deuterated poly-Si deposition," *in: Proc. IEEE IEDM Tech. Dig.*, pp. 343–346, December 2000.
- [64] D. J. DiMaria and J. H. Stathis, "Explanation for the oxide thickness dependence of breakdown characteristics of metal-oxide-semiconductor structures," *Appl. Phys. Lett.*, vol. 70, no. 20, pp. 2708–2710, May 1997.
- [65] D. J. DiMaria, "Electron energy dependence of metal-oxide semiconductor degradation," *Appl. Phys. Lett.*, vol. 75, no. 16, pp. 2427–2428, October 1999.
- [66] S. Lombardo, J. H. Stathis, B. P. Linder, K. L. Pey, F. Palumbo, and C. H. Tung, "Dielectric breakdown mechanisms in gate oxides," *J. Appl. Phys.*, vol. 98, no. 98, 121301, pp. 1–36, December 2005.

- [67] R. Degraeve, B. Kaczer, and G. Groeseneken, "Degradation and breakdown in thin oxide layers: mechanisms, models and reliability prediction," *Microelectron. Reliab.*, vol. 39, no. 10, pp. 1445–1460, October 1999.
- [68] M. V. Fischetti, "Model for the generation of positive charge at the Si/SiO₂ interface based on hot-hole injection from the interface," *Phys. Rev. B*, vol. 31, no. 4, pp. 2099–2113, February 1985.
- [69] D. J. DiMaria, E. Cartier, and D. A. Buchanan, "Anode hole injection and trapping in silicon dioxide," *J. Appl. Phys.*, vol. 80, no. 1, pp. 304–317, July 1996.
- [70] D. J. DiMaria, D. Arnold, and E. Cartier, "Impact ionization and positive charge formation in silicon dioxide films on silicon," *Appl. Phys. Lett.*, vol. 60, no. 17, pp. 2118–2120, April 1992.
- [71] J. Kim, J. J. Sanchez, T. A. DeMassa, M. T. Quddus, D. Smith, F. Shaapur, K. Weiss, and C. H. Liu, "Surface plasmons and breakdown in thin silicon dioxide films on silicon," *J. Appl. Phys.*, vol. 84, no. 3, pp. 1430–1438, August 1998.
- [72] P. E. Nicollian, W. R. Hunter, and J. C. Hu, "Experimental evidence of voltage driven breakdown models in ultrathin gate oxides," *in: Proc. Int. Reliab. Phys. Symp. (IRSP)*, pp. 7–15, April 2000.
- [73] J. D. Bude, B. E. Weir, and P. J. Silverman, "Explanation of stress-induced damage in thin oxides," *in: Proc. IEEE IEDM Tech. Dig.*, pp. 179–182, December 1998.
- [74] M. A. A. B. E. Weir, J. D. Bude, P. J. Silverman, A. Ghetti, F. Baumann, P. Diodato, D. Monroe, T. Sorsch, G. L. Timp, Y. Ma, M. M. Brown, A. Hamad, D. Hwang, and

- P. Mason, "Gate oxide reliability projection to the sub-2 nm regime," *Semicond. Sci. Technol.*, vol. 15, no. 5, pp. 455–461, May 2000.
- [75] J. H. Stathis and D. J. DiMaria, "Reliability projection for ultra-thin oxides at low voltage," *in: Proc. IEEE IEDM Tech. Dig.*, pp. 167–170, December 1998.
- [76] D. J. DiMaria, "Defect generation under substrate-hot-electron injection into ultra-thin silicon dioxide layers," *J. Appl. Phys.*, vol. 86, no. 4, pp. 2100–2109, August 1999.
- [77] ———, "Defect generation in ultrathin silicon dioxide films produced by anode hole injection," *Appl. Phys. Lett.*, vol. 77, no. 17, pp. 2716–2718, October 2000.
- [78] D. J. DiMaria and J. H. Stathis, "Anode hole injection, defect generation, and breakdown in ultrathin silicon dioxide films," *J. Appl. Phys.*, vol. 89, no. 9, pp. 5015–5024, May 2001.
- [79] P. M. Lenahan and J. F. Conley, "What can electron paramagnetic resonance tell us about the Si/SiO₂ system," *J. Vac. Sci Technol. B*, vol. 16, no. 4, pp. 2134–2153, July 1998.
- [80] J. McPherson, V. Reddy, K. Banerjee, and H. Le, "Comparison of E and 1/E TDDB models for SiO₂ under long-term/low-field test condition," *in: Proc. IEEE IEDM Tech. Dig.*, pp. 171–174, December 1998.
- [81] A. Teramoto, H. Umeda, K. Azamawari, K. Kobayashi, K. Shiga, J. Komori, Y. Ohno, and H. Miyoshi, "Study of oxide breakdown under very low electric field," *in: Proc. Int. Reliab. Phys. Symp. (IRSP)*, vol. 37, pp. 66–71, March 1999.

- [82] J. S. Suehle, P. Chaparala, C. Messick, W. M. Miller, and K. C. Boyko, "Field and temperature acceleration of time-dependent dielectric breakdown in intrinsic thin SiO₂," *in: Proc. Int. Reliab. Phys. Symp. (IRSP)*, pp. 120–125, April 1994.
- [83] J. S. Suehle and P. Chaparala, "Low electric field breakdown of thin SiO₂ films under static and dynamic stress," *IEEE Trans. Electron. Devices*, vol. 44, no. 5, pp. 801–808, May 1997.
- [84] A. Yassine, H. E. Nariman, and K. Olasupo, "Field and temperature dependence of tddb of ultrathin gate oxide," *IEEE Electron. Device Lett.*, vol. 20, no. 8, pp. 390–392, August 1999.
- [85] J. S. Suehle, P. Chaparala, C. Messick, W. M. Miller, and K. C. Boyko, "Field and temperature acceleration model for time-dependent dielectric breakdown," *IEEE Trans. Electron. Devices*, vol. 46, no. 1, pp. 220–229, January 1999.
- [86] K. Umeda, T. Tomita, and K. Taniguchi, "Silicon dioxide breakdown induced by SHE (Substrate Hot Electron) injection," *Electronics and Communications in Japan*, vol. 80, no. 8, pp. 11–19, December 1997.
- [87] E. Y. Wu, W. W. Abadeer, L.-K. Han, S. H. Lo, and G. Hueckel, "Challenges for accurate reliability projections in the ultra-thin oxide regime," *in: Proc. Int. Reliab. Phys. Symp. (IRSP)*, vol. 37, pp. 57–65, March 1999.
- [88] G. Ghibaudo, G. Pananakakis, R. Kies, E. Vincent, and C. Papadas, "Accelerated dielectric breakdown and wear out standard testing methods and structures for reliability evaluation of thin oxides," *Microelectron. Reliab.*, vol. 39, pp. 597–613, 1999.

- [89] Y. Yaw and R. S. Muller, "A theoretical derivation of the log-normal distribution of time-dependent dielectric breakdown in thin oxides," *Solid-State Electro.*, vol. 32, no. 7, pp. 541–546, July 1989.
- [90] E. Y. Wu and R. P. Vollertsen, "On the weibull shape factor of intrinsic breakdown of dielectric films and its accurate experimental determination. Part I: theory, methodology, experimental techniques," *IEEE Trans. Electron. Devices*, vol. 49, no. 12, pp. 2131 – 2140, December 2002.
- [91] E. Y. Wu, J. H. Stathis, and L. K. Han, "Ultra-thin oxide reliability for ULSI applications," *Semicon. Sci. Technol.*, vol. 15, no. 5, pp. 425–435, May 2000.
- [92] R. Degraeve, *High Dielectric Constant Materials: VLSI MOSFET Applications*. Springer, 2005, ch. 4: Oxide Reliability Issues, pp. 91–120.
- [93] R. Degraeve, N. Pagon, B. Kaczer, T. Nigam, G. Groeseneken, and A. Naem, "Temperature acceleration of oxide breakdown and its impact on ultra-thin gate oxide reliability," *in: Proc. Symp. VLSI Tech. Dig.*, pp. 59–60, June 1999.
- [94] C. C. Chen, C. Y. Chang, C. Chien, T. H. Huang, H. C. Lin, and M. S. Liang, "Temperature-accelerated dielectric breakdown in ultrathin gate oxides," *Appl. Phys. Lett.*, vol. 74, no. 24, pp. 3708–3710, June 1999.
- [95] A. Yassine and H. E. Nariman, "Field and temperature dependence of TDDB of ultrathin gate oxide," *IEEE Electron. Device Lett.*, vol. 20, no. 8, pp. 390–392, August 1999.

- [96] O. Briere, A. Halimaoui, and G. Ghibaudo, "Breakdown characteristics of ultra-thin gate oxides following field and temperature stresses," *Solid State Electron.*, vol. 41, no. 7, pp. 981–985, July 1997.
- [97] D. J. DiMaria and J. H. Stathis, "Non-arrhenius temperature dependence of reliability in ultrathin silicon dioxide films," *Appl. Phys. Lett.*, vol. 74, no. 12, pp. 1752–1754, March 1999.
- [98] J. S. Suehle, B. Zhu, Y. Chen, and J. B. Bernstein, "Acceleration factors and mechanistic study of progressive breakdown in small area ultra-thin gate oxides," *in: IEEE Int. Reliab. Phys. Symp. Proc. (IRSP)*, pp. 95–101, April 2004.
- [99] H. Fukuda, M. Yasuda, and T. Iwabuchi, "Oxide wearout phenomena of ultrathin SiO₂ film during high-field stress," *Electron. Lett.*, vol. 28, no. 16, pp. 1516–1518, July 1992.
- [100] M. Depas, T. Nigam, and M. M. Heyns, "Soft breakdown of ultra-thin gate oxide layers," *IEEE Trans. Electron. Devices*, vol. 43, no. 9, pp. 1499–1504, September 1996.
- [101] S. Lee, B. Cho, J. Kim, and S. Choi, "Quasibreakdown of ultrathin gate oxide under high field stress," *in: Proc. IEEE IEDM Tech. Dig.*, pp. 605–608, December 1994.
- [102] A. Halimaoui, O. Briere, and G. Ghibaudo, "Quasi-breakdown in ultrathin gate dielectrics," *Microelectron. Eng.*, vol. 36, no. 1, pp. 157–60, June 1997.
- [103] K. Fu, "Partial breakdown of the tunnel oxide in floating gate devices," *Solid-State Electron.*, vol. 41, no. 5, pp. 774–777, May 1997.

- [104] J. C. Jackson, T. Robinson, O. Oralkan, D. J. Dumin, and G. A. Brown, “Non-uniqueness of time-dependent-dielectric-breakdown distributions,” *Appl. Phys. Lett.*, vol. 71, no. 25, pp. 3682–3684, December 1997.
- [105] E. Miranda and J. Suñé, “Electron transport through broken-down ultra-thin SiO₂ layers in MOS devices,” *Microelectron. Reliab.*, vol. 44, no. 1, pp. 1–23, January 2004.
- [106] T. Sakura, H. Utsunomiya, Y. Kamakura, and K. Taniguchi, “A detailed study of soft- and pre-soft-breakdowns in small geometry MOS structures,” *in: Proc. IEEE IEDM Tech. Dig.*, pp. 183–186, December 1998.
- [107] G. Cellere, L. Larcher, M. Valentini, and A. Paccagnella, “Micro-breakdown in small-area ultrathin gate oxides,” *IEEE Trans. Electron. Dev.*, vol. 49, no. 8, pp. 1367–74, August 2002.
- [108] T. Chen, M. Tse, C. Sun, and S. Fung, “Post-breakdown conduction instability of ultrathin SiO₂ films observed in ramped-current and ramped-voltage measurements,” *Jpn. J. Appl. Phys.*, vol. 41, no. 5A, pp. 3047–51, May 2002.
- [109] M. Houssa, T. Nigam, P. Mertens, and M. Heyns, “Model for the current-voltage characteristics of ultrathin gate oxides after soft breakdown,” *J. Appl. Phys.*, vol. 84, no. 8, pp. 4351–4355, October 1998.
- [110] J. Suñé and E. Miranda, “Post soft breakdown conduction in SiO₂ gate oxides,” *in: Proc. IEDM Tech. Dig.*, pp. 533 – 536, December 2000.

- [111] E. Miranda, J. Suñé, R. Rodríguez, M. Nafría, and X. Aymerich, “Detection and fitting of the soft breakdown failure mode in MOS structures,” *Solid-State Electron*, vol. 43, no. 9, pp. 1801–5, September 1999.
- [112] A. Cester, L. Bandiera, G. Ghidini, I. Bloom, and A. Paccagnella, “Soft breakdown current noise in ultra-thin gate oxides,” *Solid-State Electron.*, vol. 46, no. 7, pp. 1019–25, July 2002.
- [113] F. Crupi, C. Ciofi, G. Iannaccone, B. Neri, and S. Lombardo, “Current noise at the oxide hard-breakdown,” *Microelectron. Eng.*, vol. 59, no. 1–4, pp. 43–47, November 2001.
- [114] F. Crupi, G. Iannaccone, I. Crupi, R. Degraeve, G. Groeseneken, and H. Maes, “Characterization of soft breakdown in thin oxide NMOSFETs based on the analysis of the substrate current,” *IEEE Trans. Electron. Devices*, vol. 48, no. 6, pp. 1109–13, June 2001.
- [115] F. Crupi, R. Degraeve, G. Groeseneken, T. Nigam, and H. Maes, “On the properties of the gate and substrate current after soft breakdown in ultrathin oxide layers,” *IEEE Trans. Electron. Devices*, vol. 45, no. 11, pp. 2329–34, November 1998.
- [116] M. Rasras, I. D. Wolf, G. Groeseneken, R. Degraeve, and H. Maes, “Origin of substrate hole current after gate oxide breakdown,” *J. Appl. Phys.*, vol. 91, no. 4, pp. 2155–2160, February 2002.
- [117] E. Viganò, A. Ghetti, G. Ghidini, and A. Spinelli, “Post-breakdown characterization in thin gate oxides,” *Microelectron. Reliab.*, vol. 42, no. 9–11, pp. 1491–1496, January 2002.

- [118] M. Rasras, I. D. Wolt, G. Groeseneken, B. Kaczer, R. Degraeve, and H. E. Maes, “Photo-carrier generation as the origin of Fowler-Nordheim-induced substrate hole current in thin oxides,” *in: Proc. IEEE IEDM Tech. Dig.*, pp. 465–468, December 1999.
- [119] K. Cheung, J. Colonell, C. Chang, W. Lai, C. Liu, and R. Liu, “Energy funnels a new oxide breakdown model,” *in: Proc. Symp. VLSI Technology*, vol. 10, no. 12, pp. 145–146, June 1997.
- [120] K. Okada and K. Taniguchi, “Electrical stress-induced variable-range-hopping conduction in ultrathin silicon dioxides,” *Appl. Phys. Lett.*, vol. 70, no. 3, pp. 351–353, January 1997.
- [121] N. F. Mott, E. A. Davis, and R. A. Street, “States in the gap and recombination in amorphous semiconductors,” *Philosophical Magazine*, vol. 32, no. 5, pp. 961–996, November 1975.
- [122] N. Vandewalle, M. Ausloos, M. Houssa, P. Mertens, and M. Heyns, “Non-gaussian behavior and anticorrelations in ultrathin gate oxides after soft breakdown,” *Appl. Phys. Lett.*, vol. 74, no. 11, pp. 1579–81, March 1999.
- [123] M. Houssa, N. Vandewalle, T. Nigam, M. Ausloos, P. Mertens, and M. Heyns, “Analysis of the gate voltage fluctuations in ultra-thin gate oxides after soft breakdown,” *in: Proc. IEDM Tech. Dig.*, pp. 909–912, December 1998.
- [124] E. Miranda, R. Rodríguez, J. Suñé, M. Nafria, and X. Aymerich, “Switching behavior of the soft breakdown conduction characteristics in ultrathin SiO₂ layers,” *in: Proc. IEEE Int. Reliab. Phys. Symp. (IRSP)*, pp. 42–45, March 1998.

- [125] E. Miranda and J. Suñé, “Mesoscopic approach to the soft breakdown failure mode in ultrathin SiO₂ films,” *Appl. Phys. Lett.*, vol. 78, no. 2, pp. 225–227, January 2001.
- [126] J. Suñé, E. Miranda, M. Nafria, and X. Aymerich, “Point contact conduction at the oxide breakdown of MOS devices,” *in: Proc. IEDM Tech. Dig.*, pp. 191–194, December 1998.
- [127] P. Flory, “Molecular size distribution in three dimensional polymers. I. Gelation,” *J. Am. Chem. Soc.*, vol. 63, pp. 3083–3090, November 1941.
- [128] W. Stockmayer, “Theory of molecular size distribution and Gel formation in branched polymers,” *J. Chem. Phys.*, vol. 12, no. 4, pp. 45–55, April 1944.
- [129] D. Stauffer and A. Aharony, *Introduction to Percolation Theory*, 2nd ed. London, Washington DC: Taylor and Francis, 1992.
- [130] S. R. Broadbent and J. M. Hammersley, “Percolation processes. I,II. crystals and mazes,” *in: Proc. Cambridge Philos. Soc.*, vol. 53, no. 3, pp. 629 – 641 and 642–645, July 1957.
- [131] J. W. Essam and K. M. Gwilym, “Scaling laws for percolation processes,” *J. Physics, Part C: Solid State Physics*, vol. 4, no. 10, pp. L228–L232, July 1971.
- [132] R. G. Larson, L. E. Scriven, and H. T. Davis, “Percolation theory of two phase flow in porous-media,” *Chemical Engineering Science*, vol. 36, no. 1, pp. 57–73, 1981.
- [133] R. Zallen and H. Scher, “Percolation on a continuum and localization-delocalization transition in amorphous semiconductors,” *Physical Review B*, vol. 4, no. 12, pp. 4471–4479, 1971.

- [134] J. W. Essam, K. M. Gwilym, and J. M. Loveluck, “Thermodynamic scaling laws for a dilute ferromagnet in percolation limit by series methods,” *J. Phys. C - Solid State Physics*, vol. 9, no. 2, pp. 365–378, 1976.
- [135] A. G. Zilman and S. A. Safran, “Thermodynamics and structure of self-assembled networks,” *Physical review. E, Statistical physics, plasmas, fluids, and related interdisciplinary topics*, vol. 66, no. 5, pp. 051 107–1–28, November 2002.
- [136] W. Vonniessen and A. Blumen, “Dynamics of forest-fires as a directed percolation model,” *Journal Of Physics A-Mathematical And General*, vol. 19, no. 5, pp. L289–L293, April 1986.
- [137] S. Clar, B. Drossel, and F. Schwabl, “Forest fires and other examples of self-organized criticality,” *J. Phys.: Condens. Matter*, vol. 8, no. 37, pp. 6803–6824, September 1996.
- [138] D. L. Turcotte, “Self-organized criticality,” *Rep. Prog. Phys.*, vol. 62, no. 10, pp. 1377–1429, October 1999.
- [139] H. L. Frisch and J. M. Hammersley, “Percolation process and related topics,” *J. Soc. Indust. Appl. Math.*, vol. 11, no. 4, pp. 894–918, December 1963.
- [140] V. K. S. Shante and S. Kirkpatrick, “An introduction to percolation theory,” *Advances in Physics*, vol. 20, no. 85, pp. 325–357, May 1971.
- [141] S. Y. Wang, N. T. Liang, and Y. Shan, “Percolation and areal electrical conductance in an ultra thin bismuth film,” *Chinese Journal of Physics*, vol. 15, no. 4, p. 243, August 1977.

- [142] G. Grimmett, *Percolation*, 2nd ed. Berlin: Springer, 1999, vol. 321 of Grundlehren der Mathematischen Wissenschaften.
- [143] M. E. Fisher, “Critical probabilities for cluster size and percolation problems,” *J. of Mathematical Physics*, vol. 2, no. 4, pp. 620–627, July 1961.
- [144] S. K. Sinha, *Introduction to Statistical Mechanics*, 1st ed. Alpha Science International, 2006.
- [145] J. Shi, “Two-dimensional metal-insulator transition,” Ph.D. Thesis, Oklahoma State University, May 2002.
- [146] N. J. Kim, “2D metal-insulator transition in si-based materials,” Ph.D. Thesis, University of North Carolina, Department of Physics and Astronomy, 2001.
- [147] J. M. Ziman, “The localization of electrons on ordered and disordered system,” *J. Phys C :Solid State Phys.*, vol. 1, no. 2, pp. 1532–1538, December 1968.
- [148] V. Ambegaokar, B. I. Halperin, and J. S. Langer, “Hopping conductivity in disordered systems,” *Phys. Rev. B*, vol. 4, no. 8, pp. 2612–2620, October 1971.
- [149] B. J. Last and D. J. Thouless, “Percolation theory and electrical conductivity,” *Phys. Rev. Lett.*, vol. 27, no. 25, pp. 1719 – 1721, December 1971.
- [150] S. Kirckpatrick, “Percolation and conductance,” *Rev. Modern Phys.*, vol. 45, no. 4, pp. 574 – 588, October 1973.
- [151] J. Hoshen and R. Kopelman, “Percolation and cluster distribution. I. cluster multiple labeling technique and critical concentration algorithm,” *Phys. Rev. B.*, vol. 1, no. 8, pp. 3438–3445, October 1976.

- [152] M. A. Alam, B. Weir, J. Bude, P. Silverman, and D. Monroe, "Explanation of soft and hard breakdown and its consequences for area scaling," *in: Proc. IEEE IEDM Tech. Dig.*, pp. 449–452, December 1999.
- [153] E. Miranda, J. Suñé, R. Rodríguez, M. Nafria, X. Aymerich, L. Fonseca, and F. Campabadal, "Soft breakdown conduction in ultrathin (3-5 nm) gate dielectrics," *IEEE Trans. Electron. Devices*, vol. 47, no. 1, pp. 82–89, January 2000.
- [154] T. Yoshida, S. Miyazaki, and M. Hirose, "Analytical modeling of quasi-breakdown of ultrathin gate oxides under constant current stressing," *Int. Conf. Solid State Dev. Mater. (SSDM), Ext. Abst.*, pp. 539–541, September 1996.
- [155] E. Y. Wu, R. P. Vollertsen, and W. Lai, "On the weibull shape factor of intrinsic breakdown of dielectric films and its accurate experimental determination. Part II: Experimental results and the effects of stress conditions," *IEEE Trans. Electron. Devices*, vol. 49, no. 12, pp. 2141 – 2150, December 2002.
- [156] B. E. Weir, M. A. Alam, P. J. Silverman, F. Baumann, D. Monroe, J. D. Bude, G. L. Timp, A. Hamad, Y. Ma, M. M. Brown, D. Hwang, T. W. Sorsch, A. Ghetti, and G. Wilk, "Ultra-thin gate oxide reliability projections," *Solid-State Electron.*, vol. 46, no. 3, pp. 321–328, March 2002.
- [157] E. Y. Wu and J. Suñé, "Power-law voltage acceleration: A key element for ultrathin gate oxide reliability," *Microelectron. Reliab.*, vol. 45, no. 12, pp. 1809–1834, December 2005.
- [158] E. Y. Wu, A. Vayshenker, E. Nowak, J. Suñé, R. P. Vollertsen, W. Lai, and D. Harmon, "Experimental evidence of T_{BD} power-law for voltage dependence of oxide

- breakdown in ultrathin gate oxides,” *IEEE Trans. Electron. Devices*, vol. 49, no. 12, pp. 2242 – 2251, December 2002.
- [159] E. Y. Wu, J. Aitken, E. Nowak, A. Vayshenker, P. Varekamp, G. Hueckel, J. McKenna, D. Harmon, L. K. Han, C. Montrose, and R. Dufresne, “Voltage-dependent voltage-acceleration of oxide breakdown for ultra-thin oxides,” *in: Proc. IEEE IEDM Tech. Dig.*, pp. 541–544, December 2000.
- [160] A. K. Basu, *An Introduction to Stochastic Process*, 1st ed. Alpha Science International, 2003.
- [161] J. Besag, P. Green, D. Higdon, and K. Mengersen, “Bayesian computation and stochastic-systems,” *Statistical Science*, vol. 10, no. 1, pp. 3–41, February 1995.
- [162] J. P. Huelsenbeck, B. Larget, and D. Swofford, “A compound poisson process for relaxing the molecular clock,” *Genetics*, vol. 154, no. 4, pp. 1879–1892, April 2000.
- [163] M. Kijima and M. Ohnishi, “Stochastic orders and their applications in financial optimization,” *Mathematical methods of operations research*, vol. 50, no. 2, pp. 351–372, October 1999.
- [164] J. Buongiorno, “Generalization of faustmann’s formula for stochastic forest growth and prices with markov decision process models,” *Forest Sci.*, vol. 47, no. 4, pp. 466–474, November 2001.
- [165] A. T. Cemgil and B. Kappen, “Monte carlo methods for tempo tracking and rhythm quantization,” *Journal of artificial intelligence research*, vol. 18, pp. 45 – 81, January 2003.

- [166] Y. T. Qi, J. W. Paisley, and L. Carin, "Music analysis using hidden markov mixture models," *IEEE transactions on signal processing*, vol. 55, no. 11, pp. 5209–5224, November 2007.
- [167] J. R. Norris, *Markov Chains*, ser. Cambridge Series in Statistical and Probabilistic Mathematics. Cambridge University Press, 1997.
- [168] P. G. Doyle and J. L. Snell, "Random walks and electric networks," *Arxiv preprint math.*, January 2000.
- [169] B. Bollobás, *Modern Graph Theory*, 2nd ed., S. Alexer, F. W. Gehring, and K. A. Ribet, Eds. United States of America: Springer-Verlag New York, Inc., 1998.
- [170] B. E. Weir, P. Silverman, K. S. K. D. Monroe, M. Alam, G. Alers, T. W. Sorsch, G. L. Timp, F. Baumann, C. T. Liu, Y. Ma, and D. Hwang, "Ultra-thin gate dielectrics: They break down, but do they fail?" *in: Proc. IEEE IEDM Tech. Dig.*, pp. 73–76, December 97.
- [171] J. G. Proakis and D. G. Manolakis, *Digital Signal Processing: Principles, Algorithms, and Applications*, 4th ed. Prentice Hall, 2006.
- [172] J. Maserjian and N. Zamani, "Observation of positively charged state generation near the Si/SiO₂ interface during Fowler-Nordheim tunneling," *J. Vac. Sci. Technol.*, vol. 20, pp. 743–746, 1982.
- [173] T. Nguyen, P. Olivo, and B. Riccò, "A new failure mode of very thin ($< 50 \text{ \AA}$) thermal SiO₂ films," *in: Proc. Int. Reliab. Phys. Symp. (IRSP)*, pp. 66–71, April 1987.

- [174] K. Naruke, S. Taguchi, and M. Wada, "Stress-induced leakage current limiting to scale down EEPROM tunnel oxide thickness," *in: Proc. IEEE IEDM Tech. Dig.*, pp. 424–427, December 1988.
- [175] A. I. Chou, K. Lai, K. Kumar, P. Chowdhury, and J. C. Lee, "Modeling of stress-induced leakage current in ultrathin oxides with the trap-assisted tunneling mechanism," *Appl. Phys. Lett.*, vol. 70, no. 25, pp. 3407–3409, March 1997.
- [176] S. I. Takagi, N. Yasuda, and A. Toriumi, "Experimental evidence of inelastic tunneling in stress-induced leakage current," *IEEE Trans. Electron. Devices*, vol. 46, no. 2, pp. 335–341, February 1999.
- [177] I. J. D. Blauwe, "Stress induced leakage current in thin dielectrics and its impact on flash memory reliability," Ph.D. Thesis, Katholieke University Leuven, May 1998.
- [178] E. Rosenbaum and L. F. Register, "Mechanism of stress-induced leakage current in MOS capacitors," *IEEE Trans. Electron. Devices*, vol. 44, no. 2, pp. 317–323, February 1997.
- [179] P. Olivo, T. N. Nguyen, and B. Riccò, "High-field-induced degradation in ultra-thin SiO₂ films," *IEEE Trans. Electron. Devices*, vol. 35, no. 12, pp. 2259–2267, Dec. 1988.
- [180] G. J. Hemink, K. Shimizu, S. Aritome, and R. Shiota, "Trapped hole enhanced stress induced leakage currents in NAND EEPROM tunnel oxides," *in: IEEE Int. Reliab. Phys. Symp.(IRSP)*, pp. 117–121, April 1996.

- [181] C. Cheng, C. Hu, and R. W. Brodersen, "Quantum yield of electron impact ionization in silicon," *J. Appl. Phys.*, vol. 57, no. 2, pp. 302–309, January 1985.
- [182] R. Mozzami and C. Hu, "Stress-induced current in thin silicon dioxide films," *in: Proc. IEEE IEDM Tech. Dig.*, pp. 139–142, December 1992.
- [183] N. Yasuda, N. Patel, and A. Toriumi, "A two-step tunneling model for the stress induced leakage currents in thin silicon dioxide films," *Solid State Dev. Mater.*, pp. 847–850, 1993.
- [184] D. J. DiMaria and E. Cartier, "Mechanism for stress-induced leakage currents in thin silicon dioxide films," *J. Appl. Phys.*, vol. 78, no. 6, pp. 3883–3894, September 1995.
- [185] D. J. Dumin and J. R. Maddux, "Correlation of stress-induced leakage current in thin oxides with trap generation inside the oxides," *IEEE Trans. Electron. Devices*, vol. 40, no. 5, pp. 986–993, May 1993.
- [186] R. Rofan and C. Hu, "Stress-induced oxide leakage," *IEEE Electron. Device Lett.*, vol. 12, no. 11, pp. 632–634, November 1991.
- [187] R. Moazzami and C. Hu, "Stress-induced current in thin silicon dioxide films," *in: Proc. IEEE IEDM Tech. Dig.*, pp. 139–142, December 1992.
- [188] M. R. Herrmann and A. Schenk, "Field and high-temperature dependence of the long term charge loss in erasable programmable read only memories: Measurements and modeling," *J. Appl. Phys.*, vol. 77, no. 9, pp. 4522–4540, May 1995.

- [189] M. Kimura and H. Koyama, “Stress-induced low-level leakage mechanism in ultrathin silicon dioxide films caused by neutral oxide trap generation,” *in: IEEE Int. Reliab. Phys. Symp. (IRSP)*, pp. 167–172, April 1994.
- [190] B. Riccò, G. Gozzi, and M. Lanzoni, “Modeling and simulation of stress-induced leakage current in ultrathin SiO₂ films,” *IEEE Trans. Electron. Devices*, vol. 45, no. 7, pp. 1554–1560, July 1998.
- [191] T. Endoh, T. Chiba, H. Sakuraba, M. Lenski, and F. Masuoka, “A quantitative analysis of stress-induced leakage currents and extraction of trap properties in 6.8 nm ultrathin silicon dioxide films,” *IEICE Trans. Electron*, vol. 86, no. 4, pp. 2095–2099, May 1999.
- [192] T. Endoh, K. Hirose, and K. Shiraishi, “Physical origin of stress-induced leakage currents in ultra-thin silicon dioxide films,” *IEICE Trans. Electron*, vol. E90, no. 5, pp. 955–961, May 2007.
- [193] P. A. Lee and T. V. Ramakrishnan, “Disordered electronic systems,” *Reviews of Modern Physics*, vol. 57, no. 2, pp. 287–337, April 1985.
- [194] K. C. Chang, “Quantum theory of percolation,” Ph.D. Thesis, The Faculty of the Graduate School of Arts and Sciences, Brandeis University, Department of Physics, December 1986.
- [195] T. Odagaki and K. C. Chang, “Real-space renormalization-group analysis of quantum percolation,” *Phys. Rev. B*, vol. 30, no. 3, pp. 1612–1614, August 1984.

- [196] B. Kramer, T. Ohtsuki, and S. Kettemann, “Random network models and quantum phase transitions in two dimensions,” *Phys. Report-Review Section of Phys. Lett.*, vol. 417, no. 5–6, pp. 211–342, October 2005.
- [197] M. Vojta, “Quantum phase transitions,” *Reports on Progress in Physics*, vol. 66, no. 12, pp. 2069–2110, 2003.
- [198] S. Sachdev, *Quantum Phase Transitions*. Cambridge University Press, 2001.
- [199] D. R. Wolters and Z. V. Duijnhoven, “Tunnelling in thin SiO₂,” *Philosophical Trans. Royal Soc. London Series A -Mathematical Physical And Engineering Sciences*, vol. 354, no. 1717, pp. 2327 – 2350, October 1996.
- [200] M. Lenzlinger and E. H. Snow, “Fowler-Nordheim tunneling into thermally grown SiO₂,” *J. Appl. Phys.*, vol. 40, no. 1, pp. 278–283, January 1969.
- [201] B. Hamilton, J. Jacobs, D. A. Hill, R. F. Pettifer, D. Teehan, and L. T. Canham, “Size-controlled percolation pathways for electrical conduction in porous silicon,” *Nature*, vol. 393, no. 6684, pp. 443–445, June 1998.
- [202] D. Ali and H. Ahmed, “Coulomb-blockade in a silicon tunnel junction device,” *Appl. Phys. Lett.*, vol. 64, no. 16, pp. 2119 –2120, April 1994.
- [203] “Insulator-metal transition in coulomb blockade nanostructures,” *Appl. Phys. Lett.*, vol. 79, no. 5, pp. 689–691, July 2001.
- [204] S. Redner, “Percolation and conduction in a random resistor-diode network,” *J. Phys. A: Math. Gen.*, vol. 14, no. 9, pp. L349–L354, September 1981.

- [205] S. Redner and A. C. Brown, “Percolation properties of a three-dimensional random resistor-diode network,” *J. Phys. A: Math. Gen.*, vol. 14, no. 8, pp. L285–L290, August 1981.

Glossary

A-SBD Analogue Soft Breakdown. 23

AHI Anode Hole Injection. 11

AHR Anode Hydrogen Release. 11

BD Breakdown. 5

CCS Constant Current Stress. 17

CFD Cumulative Failure Density. 51

CMOS Complementary Metal Oxide Semiconductor. 5

CPDG Constant Probability of Defect Generation. 50

CVS Constant Voltage Stress. 17

D-SBD Digital Soft Breakdown. 23

ESR Electron Spin Resonance. 15

F-N Fowler-Nordheim. 24

FET Field Effect Transistor. 1

FFT Fast Fourier Transform. 106

H-K Hoshen-Kopelman. 48

HBD Hard Breakdown. 23

IC Integrated Circuit. 1

ITRS International Technology Roadmap for Semiconductors. 4

KCL Kirchoff's Current Law. 42

MB Micro-Breakdown. 23

MOS Metal Oxide Semiconductor. 10

MOSFET Metal Oxide Semiconductor Field Effect Transistor. 1

NL-HBD Non-Linear HBD. 23

PSD Power Spectral Density. 106

QPC Quantum Point Contact. 28

RVS Ramped Voltage Stress. 17

SBD Soft Breakdown. 22

SHEI Substrate Hot Electron Injection. 16

SIA Semiconductor Industry Association. 3

SILC Stress Induced Leakage Current. 6

SOI Silicon On Insulator. 4

TAT Trap-Assisted Tunneling. 118

TDDB Time Dependent Dielectric Breakdown. 17

ULSI Ultra-Large Scale Integrated Circuit. 115

VRH Variable Range Hopping. 26

WKB Wentzel-Kramers-Brillouin . 123

Index

A

AHI, *see* Anode Hole Injection Model
AHR, *see* Anode Hydrogen-Release Model
analogue SBD, 23
Anode Hole Injection Model, 13
Anode Hydrogen-Release Model, 11
area-scaling, 20

B

breakdown statistics, 18
 log-normal, 18
 Weibull, 18
Burg algorithm, 106

C

carrier-separation, 25
charge-assisted tunneling, 116
CMOS scaling, 1
 ITRS, 4
 Moore's Law, 2

critical phenomena, 36
cumulative failure density, 19

D

diffusion, 32
digital SBD, 23

E

$1/E$ model, 13, 15
 E model, 15
 E' center, 15
electron spin resonance, 15
ESR
 electron spin resonance, 15
extreme-value distribution, 19

F

Fowler-Nordheim tunneling, 13

H

hard breakdown, 22
 high HBD, 23

low HBD, 23
 non-linear HBD, 23
 high-HBD, 23
 hydrogen release model, *see* Anode Hydrogen-
 Release Model

I

International Technology Roadmap for Semi-
 conductors, 4
 ITRS, *see* International Technology Roadmap
 for Semiconductors

L

log-normal, 18
 low-HBD, 23

M

Markov chain, 91
 absorption probability, 95
 hitting probability, 96
 micro-breakdown(MB), 23
 Moore's Law, 2

N

noise, 24, 107
 non-linear HBD, 23

O

oxide breakdown, 9
 1/ E model, 13, 15
 characterization, 17
 E model, 15
 polarity-dependence, 16
 statistics, 18
 thermochemical model, 15

P

percolation, 31
 bond percolation, 34
 conductance, 38
 history, 31
 quantum percolation, 118
 site percolation, 34
 periodogram, 106
 phase transition, 36
 metal-insulator transition, 118
 Poisson model, 20
 polya-walk, 32
 post-breakdown current, 24
 Power Spectral Density, 106
 power-law, 83

PSD, *see* Power Spectral Density

Q

quantum percolation, 118

tunneling, 118

quantum-point contact model, 28

R

reliability projection, 18

area scaling, 20

field extrapolation, 20

statistical scaling, 18

temperature scaling, 21

voltage scaling, 20

S

SHEI, 16

substrate hot electron injection, 16

SILC, 116

soft breakdown, 22

analogue SBD, 23

digital SBD, 23

micro-breakdown, 23

models, 26

percolation, 27

quantum-point contact, 28

tunneling, 26

variable range hopping, 26

stress-induced leakage current, 116

substrate hot electron injection, 16

T

temperature acceleration, 21

thermochemical model, 15

trap-assisted tunneling, 116

elastic tunneling, 116

inelastic tunneling, 116

tunneling, 26

Fowler-Nordheim tunneling, 26, 122

quantum percolation, 118

TAT (trap-assisted tunneling), 116

trap-assisted tunneling, 116

V

variable range hopping, 26

W

weakest-link, 19

Weibit, 19

Weibull, 18, 19